DEVELOPMENT OF A 3D MICROSTRUCTURE SENSITIVE CRYSTAL PLASTICITY MODEL FOR ALUMINUM

By

ALANKAR ALANKAR

A dissertation submitted in partial fulfillment of
the requirements for the degree of

DOCTOR OF PHILOSOPHY

WASHINGTON STATE UNIVERSITY
School of Mechanical and Materials Engineering

MAY 2010

To the Faculty of Washington State University:

The members of the Committee appointed to examine the dissertation of ALANKAR ALANKAR find it satisfactory and recommend that it be accepted.

_____

David P. Field, Ph.D., Chair

_____

Hussein M. Zbib, Ph.D.

_____

Jow-Lian Ding, Ph.D.

_____

Balasingam Muhunthan, Ph.D.

ACKNOWLEDGEMENT

I would like to express my heartfelt gratitude to my thesis advisor Dr. David P. Field for his guidance, mental and financial support during the course of my research work. Dr. Field has been instrumental in putting me to the ground work needed for my doctoral research. His superb direction has resulted into my professional development as a researcher. I am especially thankful to him for giving me the great opportunity for working on my dream research – dislocation density based crystal plasticity and computational materials science.

I am grateful to Dr. Hussein M. Zbib, Jow-Lian Ding and Dr. Balasingam Muhunthan for serving on my committee and their fruitful feedback in my research work. I extend my special thanks to Dr. Zbib for all knowledgeable discussions about crystal plasticity frameworks. I am thankful to him for providing with the 3D- dislocation dynamics computer program for studying the dislocation interactions. I also acknowledge the guidance of Dr. Ioannis N. Mastorakos for helping me start the project and understand dislocation dynamics simulations.

I acknowledge the partial financial support by DARPA and Alcoa Inc. to this research programme. I would like to thank the Graduate Professional Students Association at WSU, and Gordon Research Conference Committee for providing travel grants. The timely help by the MME staff members Jan Danforth, Bob Ames (past), Gayle Landeen, Michael Shook, Giac Pham, and Michelle White is appreciated.

Finally, I am thankful for the invaluable support from my family and friends, especially my parents and my brother. This thesis is dedicated to my parents who poured into me ethics, insight to aim high and determination to reach the milestones.

DEVELOPMENT OF A 3D MICROSTRUCTURE SENSITIVE CRYSTAL PLASTICITY MODEL FOR ALUMINUM

Abstract

by Alankar Alankar, Ph.D.
Washington State University
May 2010

Chair: David P. Field

A dislocation density based crystal plasticity finite element model (CPFEM) has been developed in which different dislocation densities evolve on all octahedral slip systems in aluminum. Based upon the kinematics of crystal deformation and dislocation interaction laws, dislocation generation and annihilation are modeled. Dislocation densities evolve in form of closed loops and are tracked as state variables in the model, leading to spatially inhomogeneous dislocation densities that show patterning in the dislocation structures. A generalized Taylor equation is used as the hardening law in which hardening coefficients are based on the reactions between dislocations on co-planar and non-planar slip systems. The hardening coefficients for reactions involving latent slip systems are determined using 3D discrete dislocation dynamics. The model is validated using distinct hardening behavior of {100} and {111} single crystals of aluminum. The phenomenon of overshooting in aluminum is predicted using the model. Effect of collinear interactions of dislocations is shown to enhance the overshooting behavior.

Evolution of crystallographic texture during plane strain deformation of polycrystalline aluminum is predicted. The crystallographic texture shows characteristic texture components observed in the “rolling texture” in the experiments reported in the

literature. Description of dislocation densities is presented in form of pole figures along with evolution of crystallographic texture which shows increasing heterogeneity in microstructure with increasing deformation.

Simulations of plane strain deformation on bicrystals are performed which predict rotations of crystallites during deformation and orientation spread at the final stage of deformation reasonably well as compared with the experimental observation. Similar studies are done for more complex grain topology in 2D columnar multicrystals. Overall, the model predicts heterogeneous evolution of accumulated plastic strain which is found to be consistent with the accumulated dislocation density, shear strain, dislocation density evolution rate and the Taylor factor in the corresponding grains.

TABLE OF CONTENTS

Page

LIST OF TABLES

LIST OF FIGURES

This thesis is dedicated to my wonderful parents, Rajendra Prasad and Bala Tomar, who have raised me to be the person I am today. You have been with me every step to this day through good times and bad. Thank you for all the sacrifices and pain that you went through, and for unconditional love, guidance, and endless support that you have always given me, helping me to succeed and instilling in me the confidence that I am capable of doing anything I put my mind to.

CHAPTER ONE

INTRODUCTION

G. I. Taylor's Bakerian Lecture at the Royal Society in 1923 formally started the systematic and formal study of finite deformation of cubic single crystals. This work of Taylor and Elam [1] primarily concentrated on the changing orientation of the crystal lattice. Using X-ray analysis and geometrical measurements, the specific directions of deformation in the single crystal were established. Taylor and Elam [1] established the milestone for starting the theories on crystallographic slip, lattice deformation and continuum plasticity. The crystal lattice remains invariant after crystallographic slip, as compared to elastic distortion which changes both the angles and the spacing of a crystal lattice. The effect comes due to the plasticity carriers (Taylor [2]) called dislocations.

The theory of plasticity due to dislocation motion also addresses the discrepancy between the theoretically determined intrinsic strength and the actually observed strength. Theoretical strength of a perfect crystal is two to four orders of magnitude greater than the observed strength. As assumed in theory, the shear does not occur because of the slip on the whole slip plane but only on a section of it which is associated with the movement of the dislocations. Apart from accounting for the plastic deformation in crystalline materials, the dislocations are associated with the work hardening behavior by means of their multiplication activity due to mutual interactions that hinders the motion of gliding dislocations. In 1953, Cottrell [3] mentioned that the strength of Cu and alike materials can be increased 20 times by the effect of work hardening. Basinski and Basinski [4], in talking about work hardening, quotes Cottrell [3] saying "It was the first problem to be

attempted by the dislocation theory of slip and may well prove to be the last to be solved". The crystal plasticity formulations have successfully addressed the problems like crystallographic texture using classical hardening models e.g. power laws defining crystallographic slip. However, as the research deepens, effects of hardening due to long and short range interactions and the effect of interfaces remain as two of the many other grueling issues. Even after 30 years once mentioned by Basinski and Basinski [4] Cottrell's statement still stands valid and a lot of research is being done to establish more realistic work hardening formulations. The experimental studies are always fundamental in terms of the underlying physics. However, the experiments are mostly destructive in nature and can not be used for repeating a test on the same specimen for consistency of experimental conditions. The experiments are dependent on a number of parameters e.g. purity, composition, environmental conditions, temperature and methodological perfection etc. Therefore the models which are fundamentally based on the physics of microstructure evolution need to be adapted.

1.1 Statistically stored and geometrically stored dislocations

Materials can be differentiated based on plastically homogeneous and non-homogeneous deformation. During plastic deformation dislocations multiply due to two possible reasons. First, dislocations are necessary to contain the geometry in the deformed state and second they are stored due to trapping one another. The rate of dislocation storage depends on the mean free path which a dislocation travels between two consecutive obstacles. Stress is generated by two mechanisms namely, cutting of forest dislocations and interaction of elastic fields of dislocations.

1.1.1 Statistically stored dislocations (SSDs)

SSDs are generated due to behavior of the material i.e. it is affected by crystal structure, shear modulus, stacking fault energy, etc. During homogeneous deformation (i.e. in uniaxial tensile test), material is stretched in one direction, and dislocations are stored only due to trapping by other dislocations. They are called statistically stored dislocations (SSDs).

1.1.2 Geometrically necessary dislocations (GNDs)

Geometrically necessary dislocations are generated due to non-homogeneous deformation in the material or due to a strain gradient generated on application of stress in non-homogeneous materials [5]. In two phase alloys the extent of deformation in one phase is not the same as in the other phase. In processes like bending, indentation and torsion tests, deformation is not uniform within the specimen. Zaiser and Aifantis [6] have defined the GND density as the minimum density of discrete lattice dislocations that is required to accommodate a given mesoscopic strain gradient. This strain gradient depends on the extent of deformation or distance from the axis of deformation. This distance is called the length scale of the measurement. As the distance from the deformation axis increases the extent of deformation increases [5, 7, 8]. Thus a geometrical non-equilibrium condition occurs which requires that some dislocations be stored to contain this new geometry of the specimen. These dislocations, which are necessary for compatibility of deformation, are called geometrically necessary dislocations (GNDs) [5, 7-9]. The state of dislocations associated with geometry is defined by a second order tensor called Nye's tensor, after

Nye [10]. GNDs account for crystalline anisotropy as described by Nye's tensor. Strengthening is also caused by local interaction of SSDs with GNDs [9]. Dislocation interaction mechanisms like jog formation cause macroscopic isotropic hardening. Due to trapping of dislocations long range back stress is generated which causes kinematic hardening. Fleck et al. [9] have given one case study which shows that lower plastic strains create Orowan loops, GNDs, more kinematic hardening and stronger long range back stresses. Whereas higher plastic strains cause prismatic dislocation loops, no long range back stresses and no kinematic hardening. In case of particle larger than a certain size, dislocation density evolves statistically and no GNDs will be created. At levels of plastic strain below a few percent, kinematic hardening is caused by the generation of long range elastic stresses generated by strain gradients. However, due to the reaction of GNDs and SSDs, the density of GNDs does not change. Thus the total dislocation density, given as a sum of the two types of dislocations, is a lower bound of the total dislocation density [5, 7, 11]. Arsenlis and Parks [12] showed that due to the crystallographic consideration, the actual number of dislocations produced was generally greater than the number of GNDs by a factor of r' which these researchers called the Nye factor. The Nye factor has been defined along the same lines as Nye's tensor. Nye's factor describes the crystalline anisotropy in the macroscopic measure of GND density. Dislocations tend to align themselves along boundary structures that further result in stress shielding which is associated with GNDs.

A dislocation line present in a volume of crystal can have both statistical and geometrical characteristics [12]. Because GND density is the minimum density which accounts for a certain strain gradient, the density calculated based on geometric

constraints will be the lower limit of the dislocation density. The remaining dislocations will contribute to the statistically stored dislocation density. Using a back scattered X-ray technique, the lattice rotation of a plastically bent crystal can be measured [13, 14]. The lower limit of excess dislocations (alias GNDs) can be estimated using electron backscatter diffraction (EBSD) or orientation imaging microscopy[15] by determination of lattice incompatibility [16]. Recently, similar measurements have been performed by using X-ray micro-diffraction techniques by Field et al. [17] and the observations are compared against the one s observed using EBSD.

1.2 Multiscale modeling

GNDs cannot be distinguished physically from SSDs at the macroscopic level. Only the effects of strain gradient plasticity are observed at mesoscopic or microscopic levels [6, 18-21]. Therefore while discussing GNDs in crystalline solids, it is needed to define the length scale in plastic deformation. The smallest displacement unit of plastic displacements is the Burgers vector. Therefore the plastic strain field will be discontinuous on a microscopic scale which can be as small as the average spacing between two dislocation lines ($\frac{1}{\sqrt{\rho^T}}$, where ρ^T is the total dislocation density). The response of deformation increases with decreasing scale. Fleck et al. [7] have suggested that yield strength depends both on strain and strain gradient where strain will define the scale of deformation. In case of torsion the smaller the wire, the larger the strain gradient generated. In thin wires of 12 to 170 μm diameter, torsional hardening increases as the diameter of the wire specimen decreases [7]. Hardening of a beam increases as the

thickness of thin beams, ranging from 12.5 to 50 μm, decreases [22]. Conventional crystal plasticity theories, however, do not take into account these effects making them fundamentally incapable of predicting scale dependent behavior. The substructures formed by dislocations in FCC materials observed directly, point towards the complex interactions of dislocations at different length scales. These interactions of dislocations drive for the development of simulations such as those performed by Zbib et al. [23] and Kubin [24] using the dynamics of dislocations divided into many smaller segments. The mesoscopic simulations based on dislocation dynamics are calibrated and are bridged with even an lower scale of modeling called atomistic simulations e.g. [25].

1.3 Microstructure evolution in polycrystalline materials

The initial concentration on the crystal plasticity simulations was to include the modeling of work hardening and mechanical properties in terms of flow stress at different temperatures and strain rates. In the past 3 decades, the crystal plasticity models have come forward to predict not only the mechanical properties but, crystallographic texture and overall microstructure evolution during deformation of polycrystalline materials and dislocation densities as well.

Involvement of dislocation densities in crystal plasticity finite element method (CPFEM) models enables studies on the grain interactions and the neighborhood effect on the hardening of grains. For more complex microstructure evolution phenomena, such as static recovery and recrystallization, it is important to have information on local stored energy in a structure. In CPFEM models which are based on dislocation density evolution, the stored energy information is addressed by the spatial distribution of dislocations i.e.

dislocation structures. Problems such as recrystallization can not be simply addressed by dislocation density based stored energy alone but must include effects of particles, particle matrix interface, grain boundaries, and micro-slip bands as well. It is well documented by Becker and Panchandeeswaran [26] and others that grain interactions can have a first order effect on local texture evolution. It is obvious that the local texture evolution affects the local dislocation density evolution since both are dependent upon which slip systems are active for a given deformation gradient. Therefore it is worthwhile to study the evolution of dislocation density considering the effect of texture evolution. The objectives of the current research work are to:

1. Develop a dislocation density based 3D crystal plasticity model which can predict orientation dependence of stress-strain behavior of single crystal aluminum.
2. Predict rotations of crystallites of bicrystals and multicrystals during plane strain compression and compare the results with those reported in the literature.
3. Predict the crystallographic texture evolution during planning strain compression of a polycrystal
4. Study of microstructure evolution during plane strain compression of a large grain columnar polycrystal.

1.4 Thesis outline

This research work focuses on the finite strain deformation of pure aluminum. The thesis is divided into 7 chapters. Chapter 2 gives an overview of literature available in this area

of research. The theories of dislocation density evolution and crystal plasticity modeling framework used in the past are reviewed in Chapter 2. Chapter 3 presents a dislocation density based model which has been adopted for development of a 3D CPFEM model in this work. A time integration scheme for implementing the model in the commercially available FEM package ABAQUS^{TM}/Standard is also presented in Chapter 3. The study done on the interaction of dislocations using the dislocation dynamics is presented in Chapter 4. Chapter 5 presents the study on the anisotropic behavior of aluminum single crystals. The simulation results showing stress-strain response of aluminum single crystals and their orientation evolution during finite deformation are discussed in this chapter. Chapter 5 also presents 4 case studies namely: dislocation density and orientation evolution in two bicrystals. For one of the bicrystals only orientation of the crystallites is tracked during plane strain compression. A study on the orientation split during plane strain compression is done using the other bircrystal. Simulation results showing dislocation densities, evolution of Taylor factor and orientations of constituent crystallites of a 10 grain multi-crystal are described in case study 3. The predictions of orientation evolution of selected crystallites are compared against other simulation studies and the experimental observations. Case study 4 discusses the predictions of heterogeneous microstructure evolution of an 18 grain polycrystal against the experimental observations. The conclusion of the research work and the future work are presented in Chapter 6 and Chapter 7 respectively.

References

[1] Taylor GI, Elam CF. Proceedings of The Royal Society London 1923;A102:643.

[2] Taylor GI. Proceedings of Royal Society London 1934;145:362.

[3] Cottrell AH. Dislocations and Plastic Flow in Crystals: Clarendon Press, Oxford, 1953.

[4] Basinski SJ, Basinski ZS. Plastic Deformation and Work Hardening. In: Nabarro FRN, editor. Dislocations in Solids, vol. 4. North-Holland, Amsterdam, 1979.

[5] Ashby MF. Philosophical Magazine 1970;21:399.

[6] Zaiser M, Aifantis EC. Scripta Materialia 2003;48:133.

[7] Fleck NA, Muller GM, Ashby MF, Hutchinson JW. Acta Materialia 1994;42:475.

[8] Gao H, Huang Y. Scripta Materialia 2003;48:113.

[9] Fleck NA, Ashby MF, Hutchinson JW. Scripta Materialia 2003;42:178.

[10] Nye JF. Acta Metallurgica 1953;1:153.

[11] Ashby MF. The deformation of plastically non-homogeneous alloy: Elsevier Pub. Co., 1971.

[12] Arsenlis A, Parks DM. Acta Materialia 1999;47:1597.

[13] Cahn RW. Journal of the Institute of Metals 1949;76:121.

[14] Wartan JA. Acta Crystallographica 1966;20:49.

[15] Dingley DJ, Field DP. Materials Science and Technology 1996;12:1.

[16] Field DP, Trivedi PB, Wright SI, Kumar M. Ultramicroscopy 2005;103:33.

[17] Field DP, Magid KR, Mastorakos IN, Florando JN, Lassila DH, Jr JWM. Philosophical Magazine 2010;In press.

[18] Huang Y, Gao H, Nix WD, Hutchison JW. Journal of Mechanics and Physics of Solids 2000;48:99.

[19] Jiang H, Huang Y, Zhuang Z, Hwang KC. Journal of Mechanics and Physics of Solids 2001;49:979.

[20] Huang KC, Jiang H, Huang Y, H HG, Hu N. Journal of Mechanics and Physics of Solids 2002;50:81.

[21] Guo Y, Huang Y, Gao H, Zhuang Z, Hwang KC. International Journal of Solids and Structures 2001;38:7447.

[22] Stolken JS, Evans AG. Acta Materialia 1998;46:5109.

[23] Zbib H, Rhee M, Hirth J. International Journal of Mechanical Sciences 1998;40:113.

[24] Kubin L, Canova G, Condat M, Devincre B, Pontikis V, Bréchet Y. Diffusion and Defect Data—Solid State Data, Part B (Solid State Phenomena) 1992;23-24:455.

[25] Arsenlis A, Cai W, Tang M, Rhee M, Oppelstrup T, Hommes G, Pierce TG, Bulatov VV. Modelling and Simulation in Materials Science and Engineering 2007;15:553.

[26] Becker R, Panchanadeeswaran S. Acta metallurgica et materialia 1995;43:2701.

CHAPTER TWO

LITERATURE REVIEW

Single crystal models form the basis of polycrystalline models and are used for studies of plastic anisotropy and texture evolution in metal deformation e.g. rolling, extrusion etc. [1]. In a polycrystalline material, each crystallite deforms according to its individual orientation and the local thermomechanical conditions imposed on it (e.g. deformation gradient, strain rate, temperature, tractions etc) in the polycrystalline aggregate. For correct prediction of overall microstructure evolution, grain boundary structure, interaction of constituent grains, and plastic strain heterogeneity should be considered [2-5]. Micromechanical models used for microstructure evolution studies of polycrystalline aggregates are employed as stand alone computer programs e.g. ALAMEL (cf. Van Houtte et al. [6], [7]) or are developed as user interface subroutines in commercial finite element packages, e.g. [8]. In this chapter the development of crystal plasticity models and application for microstructure evolution over the past many decades has been reviewed briefly.

2.1 Crystal plasticity formulations

The systematic study of crystallographic slip started in 1923 by Taylor and Elam [9, 10], who truly initiated the development of phenomenological single crystal continuum plasticity [cf. Taylor [11]]. The evolution of hardening laws afterwards enabled the development of more sophisticated crystal plasticity formulations staring from the 1960s until now. These models are shown to predict the stress-strain response for a given

loading history, orientation dependent hardening, evolution of lattice orientation during uniaxial plastic deformation and evolution of crystallographic texture during deformation of polycrystals etc.

The continuum crystal kinematics framework adopted in all the crystal plasticity formulations comes due to the pioneering work by Hill [12] and Mandel [13]. These authors proposed the time independent continuum frameworks for crystallographic slip in single crystals at low temperatures. Plastic flow of crystalline solids at low temperature has been studied in a time independent continuum framework by many other researchers, for example, by Bishop and Hill [14], Hutchinson [15], Havner and Shalaby [16] and Asaro and Rice [17], Hill and Rice [18], Hill and Havner [19], and Peirce et al. [20]. A detailed review of the aforesaid approaches is presented by Asaro [21]. In these formulations the dislocation motion, giving rise to overall plastic deformation, is described in terms of continuous crystallographic slips. In these models, a generalized Schmid's law is used and any slip system is considered to be active if the corresponding shear stress on that system reaches a critical value (cf. Hill [12]). The critical shear stress evolution $\dot{\tau}_{cr}^{\alpha}$ on a slip system α is given as a function of the shear rate $\dot{\gamma}^{\beta}$ on the self system or latent system β (=1, 12 for FCC crystals). This formulation of hardening is given by:

$$\dot{\tau}_{cr}^{\alpha} = \sum_{\beta=1}^{N} h_{\alpha\beta}\dot{\gamma}^{\beta} \tag{2.1}$$

where $h_{\alpha\beta}$ are the hardening moduli which take into account the effect of all the latent slip systems on each individual slip system. N is the total number of slip systems. It is shown later in this chapter that this critical shear stress is actually the slip resistance due

to the latent system and has been used in a majority of crystal plasticity models. However, a varying form of the constitutive equation for the shear strain is found in the literature. (cf. e.g. Asaro et al. [22] and Harder et al. [23]).

In the framework of time independent plasticity, the hardening laws based upon the simplified assumptions do not predict a unique set of active slip systems (cf. Hill [12], Hill and Rice [18]). To avoid this indeterminacy Havner and Shalaby [16] propose a theory of additional maximum work and Asaro [24] proposes a classic time-dependent formulation. However these approaches with simple hardening evolution laws have not been able to address issues such as stage I to stage II transition and the orientation dependence of stress-strain response of single crystals. Wu et al. [25] show that a usually considered criterion that the self hardening terms are smaller than the latent hardening terms, is not sufficient to describe the experimental findings showing single glide and overshoot. The authors later proposed a set of constitutive equations and hardening laws which are shown to predict a distinct set of active slip systems, orientation dependence of stress-strain response of single crystals, and latent hardening in stage II deformation using a time independent framework. (cf. Bassani and Wu [26]). Bassani and Wu [26] propose a phenomenological law of latent hardening in multi-slip conditions in FCC crystals which was developed in the wake of several macroscopic hardening phenomena observed in the experiments [25]. This hardening law shows a high initial hardening on a previously latent slip system and the hardening matrix can be chosen in such a way that for a time independent formulation it gives a unique set of active slip systems.

Apart from being classified as time independent and time dependent models, currently available crystal plasticity models using finite element methods (CPFEM) can

be distinguished into two major types. In the first type, slip resistances are used as internal state variables (e.g. Beaudoin et al. [1], Kalidindi et al. [8], Asaro and Rice [17], Anand and Kothari [27], Nemat-Nasser and Okinaka [28, 29], Kumar and Dawson [30], Delannay et al. [31]). In these models generally, the slip resistance due to forest (latent) system is given by Eq (2.1) and the plasticity flow rate is determined using a power law or exponential law or a combination of both forms, coupling the shear strain with the shear stress and the slip resistance. Eq (2.2) shows a typical form of this equation.

$$\dot{\gamma}^{\alpha} = \dot{\gamma}_0 \left(\frac{\tau^{\alpha}}{S^{\alpha}} \right)^{1/m} \tag{2.2}$$

where $\dot{\gamma}^{\alpha}$ is the shear rate on slip system α due to a resolved shear stress of τ^{α} against the slip resistance S^{α} caused by forest dislocations on that slip system. m is the strain rate sensitivity and $\dot{\gamma}_0$ is a reference shear rate, details of which can be read in the review by Kocks and Mecking [32]. The exponential form of the flow rule is as shown in Eq (2.3).

$$\dot{\gamma}^{\alpha} = \dot{\gamma}_0 . exp \left(1 - \left(\frac{\tau^{\alpha}}{S^{\alpha}} \right)^{p} \right)^{q} \tag{2.3}$$

where p and q are the exponential factors which define the distribution of the obstacles (e.g. forest dislocations, solute particles) on the dislocation glide plane [32]. Other than the forms given in Eq (2.2) and Eq (2.3), some researchers use a multiplicative combination of the power law and the exponential law. Zhang et al. [33] use a flow equation identical to Eq (2.2) coupled with hardening laws proposed by Bassani and Wu [26] to simulate necking during a uniaxial tensile test of single crystal Cu. Gerken and Dawson [34] use a similar flow equation and also use gradients of slip on each slip system to include the non-local effect in the constitutive equations.

A large fraction of CPFEM models use slip resistances as internal state variables and such models are able to predict the stress-strain response well. However, dislocation densities are the microstructural variables that govern the evolution of properties and would enable a more physical understanding compared to slip resistance. Nevertheless, slip resistance based models also have been used to predict local deformation and problems like surface roughening with reasonable agreement to experimental observations (e.g. predictions of local grain orientations by Zhao et al. [35]). Also the CPFEM models that do not use dislocation densities as internal state variables are not fully capable of predicting properties of the material beyond the limits of available experimental data.

In the other type of models, dislocation density/densities are used as internal state variables (e.g. Cuitino and Ortiz [36], Tabourot et al. [37], Estrin et al. [38], Ohashi [39], Roters et al. [40], Busso et al. [41], Evers et al. [42], Bortoloni and Cermelli [43], Cheong et al. [44], Ma et al. [4], Brinckmann et al. [45], Rezvanian et al. [46], Zhao et al. [35]). In the phenomenological (or the empirical) equations such as those shown in Eq (2.2) and Eq (2.3), "material constants" are only fitting parameters and do not depend on the microstructural state of the material. Since the introduction of dislocations as "plasticity carriers" by Taylor in 1934 [47] there have been many advances in the understanding of physics of dislocations which has enabled the modeling of dislocation density based crystal plasticity. In these models the evolution of dislocation densities is incorporated explicitly in the framework of flow rules and slip resistance. The current status of the dislocation density based models is due to the contributions on dislocation theories of work hardening by Seeger [48], Nabarro, Basinski and Holt [49], Cottrell and

Stokes [50], Kulhmann-Wilsford [51, 52], Kocks [53] and Mecking and Kocks [54], Estrin and Mecking [55], Kocks, Argon, and Asbhy [56], Gottstein and Argon [57] and Nabarro [58]. A pioneering review of the strain hardening in FCC metals can be found in the work of Kocks and Mecking [32].

While all the dislocation density based models are based on the scale of slip systems, they can be classified in different categories based on the way dislocation density is incorporated in the framework. Cuitino and Ortiz [36] use only one (edge and screw combined) dislocation density on each slip system. Some other models such as the one by Cheong et al. [44] and Zhao et al. [35] determine the dislocation density using phenomenological equations which in turn are related to shear strain rate on each slip system. Tabourot et al. [37] and Delaire et al. [59] use a power law such as that found in Eq (2.2) and use a dislocation density based formulation for slip resistance. In their model, dislocation density evolution is given as an additive form of rate of multiplication and annihilation which are further related to the mean free path of dislocation glide and the shear rate on the corresponding slip system. While Tabourot et al. [37] show the evolution of the three stages of hardening during uniaxial tensile deformation of a pure Cu single crystal in single glide orientation, Delaire et al. [59] predict the distribution of deformation field, dislocation density and activity of slip systems in different crystallites of a single layer Cu multicrystal. Kubin et al. [60] propose a similar framework which is well informed by 3D dislocation dynamics simulations [61]. However, in contrast to the lone dependence of the mean free path of gliding dislocations on the density of forest dislocations, they suggest it to be dependent on (i) stored dislocation segment length, (ii) probability of interactions, and (iii) ratio of density of dislocations forming junctions and

the total dislocation density. Groh et al. [62] also using a multiscale approach propose a model for deformation of single crystal aluminum. In their approach molecular dynamics and dislocation dynamics are coupled with crystal plasticity in the hierarchy of increasing scale to provide with the material constants such as dislocation mobility and hardening coefficients. Brinckmann et al. [45] model the SSDs based on the mean free path of dislocations and the plastic strain and GNDs based on the gradients of plastic strain. An example of flow rule as a combination of a power law and an exponential law can be found in the work by Rezvanian et al. [46] who classify dislocation densities into statistical, GND, and the grain boundary dislocations.

In the current decade, many researchers have started developing constitutive laws based on dislocation densities alone. Some of these models define flow rules based on the Orowan equation (cf. Ohashi [63]) and hardening rules based on dislocation densities in which dislocation density evolution is given by an additive form of accumulation and annihilation. Ma et al. [4] and Roters et al. [40] use dislocation densities of mobile, forest and dislocations parallel to slip plane and use an Orowan type of equation to define the shear rate on each slip system. Arsenlis and Parks [64] proposed a model in which dislocation densities evolve in form of loops consisting of right handed and left handed edge and screw dislocations. In this model the flow rule is given by an Orowan type of equation. The authors report a modified version of the model to including strain gradient plasticity (cf. Arsenlis et al. [65]). This model is based on fundamental dislocation mechanics (e.g. continuity of dislocation line and conservation of Burgers vector). The model is shown to be capable of predicting orientation dependence of tensile stress-strain behavior of single crystal aluminum. The dislocation density evolution framework of

Arsenlis and Parks [64] has been adopted in a recently published work by Alankar et al. [66] to predict the overall crystallographic texture of polycrystalline aluminum during plane strain compression.

Strength is directly related to the dislocation density state or dislocation substructures in the material. To predict evolution of substructures, dislocation density based models incorporating length scale plasticity, are useful (cf. Ma et al. [67, 68]). These models have been able to capture the orientation dependence of single crystal stress-strain behavior and can be validated against strategic observations by electron backscatter diffraction (EBSD), details of which will be given in the latter sections of this chapter. CPFEM models based on slip resistance evolution can not be readily validated by directly observing slip resistance evolution.

2.2 Single crystal deformation and work hardening

After Diehl [69], typically, the deformation of a single crystal is differentiated into three stages. Stage I depends only on the initial orientation of the single crystal and is called the easy glide stage. The regime where dislocations start multiplying rapidly and hardening rate is steepest is termed as the stage-II and depends upon the orientation through the dependence of shear modulus *G*. Stage-III is the slower rate regime of hardening and is very sensitive to changes in the temperature and the rate of deformation [32]. The resolved shear stress or Schmid stress are the driving force for shear on the slip systems [12, 17]. The evolution of shear stress and hence accuracy of predictions in different stages of work hardening is governed by hardening laws for different slip

systems which remains the least explored part of the continuum description of crystal plasticity.

Experimental investigation of work hardening is not very straightforward. Only an indirect measurement of the evolution of hardening is found in the literature. This is due to the limitations of simultaneous measurement of small increments of shear strain with measurement of shear stress with infinitesimal increments of deformation on different slip systems. Assuming single slip and assuming dependence of hardening on deformation history, experiments have been reported for indirect latent hardening measurements. [cf. Edwards and Washburn [70], Kocks [71], Ramaswami et al. [72], Jackson and Basinski [73], Franciosi et al. [74]]. In these experiments successive stress measurements are done on primary (single glide, first test) and secondary slip systems (second test). The amount of latent hardening is determined based upon the back extrapolation of yield stress in the second test; though this back extrapolation does not include any detail of the initial hardening. Also, the subsequent hardening determined by the secondary slip may not be a good estimate of latent hardening during ‘primary’ slip. In a tensile test, the overshooting [75, 76] of the tensile axis across the symmetry line between the primary and the conjugate slip systems is a measure of the anisotropy between the two slip systems [72] and is an indirect measure of the latent hardening. Consistent with the observations of the aforesaid experiments, simplified hardening laws have been proposed. Havner and Shalaby [16] proposed a latent hardening law for finite distortions of metal crystals which was able to predict the single slip mode in FCC crystals in tension having the tensile axis beyond the crystallographic symmetry axis. Later, the authors [77] showed that the law was also able to predict the anisotropic

hardening in FCC metal crystals. However, at infinitesimal small strains the model followed isotropic hardening on all active slip systems as proposed by Taylor [11]. Kocks [71] points out that the hardness on the second system is typically 1-1.6 times the hardness on the primarily active system and is independent of the strain history. Weng [78] also identifies a high initial hardening in the secondary test of the latent hardening experiment. The hardening anisotropy measured from the overshoot experiments is based on the assumption of single glide. However the experiments elucidate that substantial amount of secondary glide starts before the overshoot [79], and the evolution of lattice orientation is not consistent with the assumption of single glide (cf. Mitchell and Thornton [80] and Joshi and Green [76]). Kuhlmann-Wilsdorf [81] points out that work hardening, if related to the increment shear stress for a given increment of shear stress and the overall flow stress alone, will not be a true representative of the work hardening. Nevertheless, an increment of shear strain is fundamentally related to the glide of dislocations. Bassani and Wu [26] develop an analytical form of hardening law for general multislip condition. The hardening for each slip system is a function of the magnitude of the slip on that system (e.g. self hardening formulation by Pierce et al. [20] and Asaro [21]) and the latent hardening is given as multiples of slip on the latent system. Bassani and Wu [26], for showing a stage I to stage II transformation, use a diagonal hardening matrix (no latent hardening) which makes sure that a previously latent system hardens only when it is active. An interesting feature of the hardening law developed by Bassani and Wu [26] is that the hardening moduli evolves during the deformation and therefore can capture the strain path along with the final state.

The difference in self-hardening and latent hardening has been identified by many researchers (cf. Franciosi and Zaoui [82]). Therefore interactions of latent slip systems are of special interest. Various researchers have concluded that overall hardening in a single crystal is accounted to the different strength of interactions between dislocations on different slip systems. For example, the reader is referred to Saada [83], Zarka [84], and Franciosi et al. [74]. Similarly, total accumulated slip due to different slip interactions on each glide system has been related to the slip resistance by Zarka [84] which enabled the modeling of salient features of stage I and stage II hardening. The high rate of hardening in stage II is a consequence of dislocation interactions (or secondary slip). With the activation of new slip systems the hardening rate on each system increases depending upon the type of dislocation locks formed with the latent systems. The newly active systems harden much faster since it faces a larger number of forest dislocations. A more detailed review of different dislocation interactions and the numerical determination of the hardening coefficients are given in the next section.

2.3 Discrete dislocation dynamics

As reviewed earlier, in crystal plasticity simulations, hardening on distinct slip systems plays a key role in the microstructure evolution during deformation processes. In the models which use dislocation densities as state variables, hardening is a function of dislocation densities on the slip systems. Even based on dislocation densities, the continuum models such as reviewed in section 2.1 are limited to the evolution of stress and dislocation densities on an average basis (up to the slip system scale). To understand the underlying physics (e.g. short range interactions of dislocations: junctions and multi-

junctions) at the micro scale, atomistic models [85] and discrete dislocation dynamics (DDD) simulations [86-90] have proven to be of great importance.

In DDD simulations, dislocations are considered to be embedded into an isotropic elastic medium [86, 88]. More details of different frameworks used for DDD simulations can be found in the work of e.g. Kubin et al. [88], Ghoniem and Sun [91], Schwarz [92], Bulatov and Kubin [93], Zbib and Rubia [94], Ghoniem et al. [95, 96], Cai et al. [97], Martinez et al. [85].

A brief overview of how 3D DDD simulations have been employed for determination of strength coefficients for different slip systems is given herein. The shear stress on a slip system α is related to the forest dislocation density ρ by a classical Taylor equation given by:

$$\tau^{\alpha} = \alpha\mu b\sqrt{\rho} \tag{2.4}$$

where μ is the shear modulus and b is the magnitude of the Burgers vector. A sophisticated form of Eq (2.4) is suggested by Franciosi and Zaoui [82] in which the hardening is dependent on the type of interacting slip systems. Eq (2.5) shows a generalized form of Eq (2.4) in which ρ^{β} is the forest dislocation density and $h^{\alpha\beta}$ is the hardening matrix details of which will be given shortly.

$$\tau^{\alpha} = \mu b\sqrt{h^{\alpha\beta}\rho^{\beta}} \tag{2.5}$$

Franciosi et al. [74] suggest that based on the symmetry of FCC crystals and the types of interactions, the overall slip resistance evolution is governed by six hardening coefficients. Four of these account for the latent hardening caused by the reactions known as Hirth junction, glissile junction, Lomer junction and collinear interaction. A Hirth junction is formed by two orthogonal burgers vectors which produce a <100> type

junction. Lomer junction and Glissile junction both form a ½<110> type junction. In the former the junction is sessile and it is glissile in the latter type. Apart from the aforementioned non-coplanar interactions, strength also evolves due to (i) parallel burgers vectors on parallel slip planes and (ii) non-parallel burgers vectors on parallel slip planes [82, 98, 99] which make the remaining two coefficients of the hardening matrix $h^{\alpha\beta}$. However those interactions are weaker than the latent interactions. Although the gliding dislocations on a slip plane do not pierce the other parallel dislocations, they do increase the resistance to slip on parallel planes [100]. It is well documented in the literature [83] that these short range interactions mostly govern the flow stress during plastic deformation. In earlier studies, Saada [83] and Schoeck and Freyman [101] did specific calculations of junctions one by one and then averaged to determine the overall strength of the forest dislocation density.

Recent research on dislocation dynamics simulations for studying the dislocation reactions can be found in the work of e.g. Kubin et al. [90], Zbib et al. [87], Shin et al. [102], Devincre et al. [103, 104] and Schwarz [105], Madec et al. [106-111] and Wickham et al. [112, 113], Bulatov et al. [114], Arsenlis et al. [89], and Martinez et al. [115]. Other possible interactions such as repulsive and crossed state reactions are also found in the literature [106, 107, 109] but are not discussed due to irrelevance to the topic of research under consideration.

It is noteworthy that the 3DDD of Kubin et al. [88] and Zbib et al. [86] are different in the way dislocation densities are used in their frameworks. The former uses straight segments of pure edge, pure screw, $\frac{\pi}{3}$, and $\frac{2\pi}{3}$ dislocations [106, 116] which form mixed types of dislocations and the latter uses curved dislocations. In the latter,

arbitrary curved dislocations are decomposed into piecewise arrays of dislocations. Dislocations dynamics simulations have been used extensively for dislocation-dislocation interactions, dislocation-interface interactions, for finding materials parameters for larger scale continuum models i.e. CPFEM, and for direct coupling with the finite element simulations successfully. For example, Akasheh et al. [117] use discrete dislocation dynamics (DDD) developed by Zbib et al. [86, 87] to find material parameters for a multiscale crystal plasticity model which is coupled with DDD. Liu et al. [118] couple the 3DDD with FE simulations such that the macroscopic boundary conditions are handled by the FE simulations and the dislocation slip activities are determined by DD. However, large number of time steps and therefore large simulation times restrict the use of DD simulations for the application into studies on dislocation density patterning, and the problems involving larger densities of dislocations. A detailed review of problems associated with large DD simulations can be read in Zbib and Rubia [94].

2.4 Microstructure evolution

The mechanical behavior of a material in response to the applied deformation conditions of a material is not fully understood. Micromechanical simulations are used to explore the effects of microstructure on the evolution of mechanical properties. These simulations give the freedom for investigation of material behavior at different scales with in the mesoscopic limits. For example, the mechanical behavior has been studied at the microstructure scale by Becker and Panchanadeeswaran [3], Diard et al. [119], Van Houtte et al. [7], Zhao et al [35], Bieler et al. [120]) and at the specimen scale by Dawson et al. [121], Delannay et al. [122]; Zamiri et al. [123]). Modern experimental techniques

have made the predictions of CPFEM models to be compared against the experimental observations. These observations will aid in further enhancing the constitutive laws. Applied deformation can be easily mapped using microscopy techniques. Bhattacharya et al. [124], Héripré et al. [125] and St-Pierre et al. [126] map the realistic EBSD data on finite element mesh to compare the strain field against the ones observed in experiments. In these simulations CPFEM models are shown to qualitatively predict the local strain field heterogeneity with good agreement. Experimentally observed strain fields were studied by comparing CPFEM simulations against experimental results of free surface strain maps inside individual grains by Delaire et al. [59] and Raabe et al. [127]. Raabe et al. [128] define a macromechanical and micromechanical Taylor factor to distinguish the effect of friction coefficient to compare the von Mises strain profiles with the ones determined from experimentally determined displacement fields. In-situ studies of plastic deformation on the surface (cf. Schroeter and McDowell [129], Musienko et al. [130]) and in the bulk (cf. 3D X-ray characterization: Poulsen et al. [131]) have been done to explore overall microstructure evolution. Hetem and Zikry [132] map SEM/EBSD data onto the FEM mesh using Voronoi tessellations and to predict localized deformation bands which are consistent with the slip system activity and accumulation of mobile and immobile dislocation density.

Microstructure evolution models which are used for studying crystallographic texture, plastic anisotropy and grain-to-grain interactions must incorporate local plastic strain heterogeneity [133]. The influence of grain boundary and the cooperative deformation of adjacent grains is shown by Van Houtte et al. [6] assuming inhomogeneous shear in the grains parallel to the grain boundary. Kanjarla et al. [133]

report that plastic heterogeneity at the triple junctions causes stress singularities leading to the creation of splitting and creation of new grain boundaries with in the grain showing the singularity. CPFEM models such as presented in this work and fast Fourier transforms (FFT) (cf. Lebensohn et al. [134]) have been used for comparing against prediction of experimental observations of evolution of crystallographic orientation. In CPFEM simulation studies, typically it is assumed that the grain boundaries are planar interfaces between two neighboring grains. (cf. Van Houtte et al. [6, 135], Lee et al. [136], Engler et al. [137], Al-Fadhalah et al. [138], Mahesh [139]). Kalidindi et al. [140] compared CPFEM simulation predictions against the plane strain experiments carried out on a high purity aluminum polycrystal with columnar grains initially oriented close to <100>. Erieau and Rey [141] use a dislocation density based CPFEM model to do a similar study on the plane strain compression of IF steel. In both studies the predictions of overall texture and individual grains orientation from CPFEM models were compared against the experimental results. The models are shown to be able to predict the overall crystallographic texture but fail to predict local orientation patterns in certain grains. Similarly, Mika and Dawson [142] and Zhao et al. [35] report the simulation predictions of local grain orientations against the experiments only in a statistical sense. Plane strain deformation of aluminum bicrystals with different orientations of tilt boundary was studied by Zaefferer et al [143]. The study by Zaefferer et al. [143] shows that orientations of individual grains play a rather important role in the microstructure evolution as compared to the misorientations between the neighboring grains.

If dislocation slip activity is considered in a statistical manner, the grain interaction effects may not be captured fully due to the lack of discrete slip activity in the

neighboring grain which is captured by employment of length scale. The non-local effects (i.e. transportation of dislocation slip effect across the grain boundaries) have been addressed by a number of researchers. (cf. Ashmawi and Zikry [144], Ma et al. [145], Acharya et al. [146]).

The CPFEM models are usually able to predict the strain fields and orientations inside the grains reasonably well on an average basis but fail to represent the experimental observations at each point of the simulated microstructure. The predictions of FE simulations depend on the scale of the mesh with respect to the microstructure.

References

[1] Beaudoin AJ, Dawson PR, Mathur KK, Kocks UF, Korzekwa DA. Computer Methods in Applied Mechanics and Engineering 1994;117:49.

[2] Liu YS, Delannay L, Van Houtte P. Acta Materialia 2002;50:1849.

[3] Becker R, Panchanadeeswaran S. Acta metallurgica et materialia 1995;43:2701.

[4] Ma A, Roters F, Raabe D. International Journal of Solids and Structures 2006;43:7287.

[5] Evers LP, Brekelmans WAM, Geers MGD. International Journal of Solids and Structures 2004;41:5209.

[6] Van Houtte P, Li S, Seefeldt M, Delannay L. International Journal of Plasticity 2005;21:589.

[7] Van Houtte P, Kanjarla AK, Van Bael A, Seefeldt M, Delannay L. European Journal of Mechanics - A/Solids 2006;25:634.

[8] Kalidindi SR, Bronkhorst CA, Anand L. Journal of Mechanics and Physics of Solids 1992;40:537.

[9] Taylor GI, Elam CF. Proceedings of The Royal Society London 1923;A102:643.

[10] Taylor GI, Elam CF. Proceedings of The Royal Society London 1925;A108:28.

[11] Taylor GI. Journal of Institute of Metals 1938;62:307.

[12] Hill R. Journal of Mechanics and Physics of Solids 1966;14:95.

[13] Mandel J. International Journal of Solids and Structures 1965;1:273.

[14] Bishop JF, Hill R. Philosophical Magazine 1951;42:414.

[15] Hutchinson JW. Proceedings of The Royal Society London 1970;A319:247.

[16] Havner KS, Shalaby AH. Proceedings of The Royal Society of London, Series A: Mathematical and Physical Sciences 1977;358:47.

[17] Asaro RJ, Rice JR. J. Mech. Phys. Solids 1977;25:309.

[18] Hill R, Rice JR. Journal of Mechanics and Physics of Solids 1972;20:401.

[19] Hill R, Havner KS. Journal of Mechanics and Physics of Solids 1982;30:5.

[20] Peirce D, Asaro RJ, Needleman A. Acta Metallurgica 1982;30:1087.

[21] Asaro RJ. Journal of Applied Physics 1983b;50:921.

[22] Asaro RJ, Hegemier GA, Maewal A. Constitutive behavior of crystalline materials. New Orleans, LA, USA: Published by The Minerals, Metals & Materials Society (TMS), 1991. p.3.

[23] Harder J. International Journal of Plasticity 1999;15:605.

[24] Asaro RJ. Advanced Applied Mechanics 1983a;23:1.

[25] Wu T-Y, Bassani JL, Laird C. Proceedings of Royal Society-Mathematical and Physical Sciences 1991;435:1.

[26] Bassani JL, Wu T-Y. Proceedings of Royal Society: Mathematical and Physical Sciences 1991;435:21.

[27] Anand L, Kothari M. Journal of Mechanics and Physics of Solids 1996;44:525.

[28] Nemat-Nasser S, Okinaka T. Mechanics of Materials 1996;24:43.

[29] Nemat-Nasser S, Ni L, Okinaka T. Mechanics of Materials 1998;30:325.

[30] Kumar A, Dawson PR. Computer Methods in Applied Mechanics and Engineering 1998;153:259.

[31] Delannay L, Jacques PJ, Kalidindi SR. International Journal of Plasticity 2006;22:1879.

[32] Kocks UF, Mecking H. Progress in Materials Science 2003;48:171.

[33] Zhanga F, Bowera AF, Mishrab RK, Boylec KP. International Journal of Plasticity 2009;25:49.

[34] Gerken JM, Dawson PR. J. Mech. Phys. Solids 2008;56:1651.

[35] Zhao Z, Ramesh M, Raabe D, Cuitiño AM, Radovitzky R. International Journal of Plasticity 2008;24:2278.

[36] Cuitino AM, Ortiz M. Modelling and Simulation in Materials Science and Engineering 1992;1:225.

[37] Tabourot L, Fivel M, Rauch E. Materials Science and Engineering A 1997;A234-23:639.

[38] Estrin Y, Sluys B, Brechet Y, Molinari A. Dislocation based gradient plasticity model. In: Bertram A, Sidoroff F, editors. Euromech Mecamat 97: 2nd European mechanics of materials conference on mechanics of materials with intrinsic length scale:

Physics, experiments, modelling and application, vol. 8. Magdeburg, Germany: EDP Sciences, 1998. p.135.

[39] Ohashi T. Philosophical Magazine Letters 1997;75:51.

[40] Roters F, Raabe D, Gottstein G. Acta Materialia 2000;48:4181.

[41] Busso EP, Meissonnier FT, O'Dowd NP. J. Mech. Phys. Solids 2000;48:2333.

[42] Evers LP, Parks DM, Brekelmans WAM, Geers MGD. Journal of Mechanics and Physics of Solids 2002;50:2403.

[43] Bortoloni L, Cermelli P. Journal of Elasticity 2004;76:113.

[44] Cheong KS, Busso EP, Arsenlis A. International Journal of Plasticity 2005;21:1797.

[45] Brinckmann S, Siegmund T, Huang Y. International Journal of Plasticity 2006;22:1784.

[46] Rezvanian O, Zikry MA, Rajendran AM. Materials Science and Engineering A 2008;494:80.

[47] Taylor GI. Proceedings of Royal Society London 1934;145:362.

[48] Seeger A, Schoeck G. Acta Metallurgica 1953;1:519.

[49] Nabarro F, Basinski ZS, Holt DB. Advanced Physics 1964;13:193.

[50] Cottrell AH, Stokes RJ. Proceedings of Royal Physical Soceity 1955;A233:17.

[51] Kulhmann-Wilsford D. Transactions of Metallurgical Society A.I.M.E. 1962;218:962.

[52] Kulhmann-Wilsford D. Metallurgical Transactions 1985;16A:2091.

[53] Kocks UF. Journal of Engineering Materials and Technology 1976;98:76.

[54] Mecking H, Kocks UF. Acta Metallurgica 1981;29:1865.

[55] Estrin Y, Mecking H. Acta Metallurgica 1984;32:57.

[56] Kocks UF, Argon AS, Ashby MF. Progress in Materials Science 1975;19:1.

[57] Gottstein G, Argon AS. Acta Metallurgica 1987;35:1261.

[58] Nabarro FRN. Work hardening of face-centered cubic single crystals. vol. 3. Montreal, Que, Can: Pergamon Press (International Series on the Strength and Fracture of Materials and Structures), 1986. p.1667.

[59] Delaire F, Raphanel JL, Rey C. Acta Materialia 2000;48:1075.

[60] Kubin L, Devincre B, Hoc T. Materials Science and Engineering A 2008;483-484:19.

[61] Kubin LP, Canova G. Scripta metallurgica et materialia 1992;27:957.

[62] Groh S, Marin EB, Horstemeyer MF, Zbib HM. International Journal of Plasticity 2009;25:1456–1473.

[63] Ohashi T. Philosophical Magazine A: Physics of Condensed Matter, Structure, Defects and Mechanical Properties 1994;70:793.

[64] Arsenlis A, Parks DM. J. Mech. Phys. Solids 2002;50:1979.

[65] Arsenlis A, Parks DM, Becker R, Bulatov VV. J. Mech. Phys. Solids 2004;52:1213.

[66] Alankar A, Mastorakos IN, Field DP. Acta Materialia 2009;57:5936.

[67] Ma A, Roters F, Raabe D. Acta Materialia 2006;54:2169.

[68] Ma A, Roters F, Raabe D. International Journal of Solids and Structures 2006;43:7287.

[69] Diehl J. Zeitschrift fuer Metallkunde/Materials Research and Advanced Techniques 1956;47:331.

[70] Edwards EH, Washburn W. Transactions of Metallurgical Society A.I.M.E. C 1954;200:1239.

[71] Kocks UF. Transactions of Metallurgical Society A.I.M.E. 1964;230:1160.

[72] Ramaswami B, Kocks UF, Chalmers B. Transactions of Metallurgical Society A.I.M.E. 1965;233:927.

[73] Jackson PL, Basinski ZS. Canadian Journal of Physics 1967;45:707.

[74] Franciosi P, Berveiller M, Zaoui A. Acta Metallurgica 1980;28:273.

[75] Bell JF, E JREGJR. Philosophical Magazine 1967;15:469.

[76] Joshi NR, Green Jr RE. Journal of Materials Science 1980;15:729.

[77] Havner KS, Shalaby AH. Journal of Applied Mechanics, Transactions ASME 1978;45:500.

[78] Weng GJ. Acta Mechanica 1981;41:217.

[79] Basinski SJ, Basinski ZS. 2nd International Conference on Strength of Metals and Alloys. Metal Park, Ohio: ASM, 1970. p.189.

[80] Mitchell TE, Thornton PR. Philosophical Magazine 1964;10:315.

[81] Kuhlmann-Wilsdorf D. Materials Science and Engineering A 1989;113:1.

[82] Franciosi P, Zaoui A. Acta Metallurgica 1982;30:1627.

[83] Saada G. Acta Metallurgica 1960;8:841.

[84] Zarka J. Constitutive equations in plasticity. In: Argon AS, editor. MIT Press, 1975. p.359.

[85] Martinez E, Marian J, Arsenlis A, Victoria M, Perlado JM. J. Mech. Phys. Solids 2008;56:869.

[86] Zbib H, Rhee M, Hirth J. International Journal of Mechanical Sciences 1998;40:113.

[87] Zbib H, Rubia TDdl, Rhee M, Hirth J. Journal of Nuclear Materials 2000;276:154.

[88] Kubin L, Canova G, Condat M, Devincre B, Pontikis V, Bréchet Y. Diffusion and Defect Data—Solid State Data, Part B (Solid State Phenomena) 1992;23-24:455.

[89] Arsenlis A, Cai W, Tang M, Rhee M, Oppelstrup T, Hommes G, Pierce TG, Bulatov VV. Modelling and Simulation in Materials Science and Engineering 2007;15:553.

[90] Kubin LP, Madec R, Devincre B. Dislocation intersections and reactions in FCC and BCC crystals. vol. 779. San Francisco, CA, United states: Materials Research Society, 2003. p.25.

[91] Ghoniem N, L. LS. Physical Review B 1999;60:128.

[92] Schwarz KW. Journal of Applied Physics 1999;85:108.

[93] Bulatov VV, Kubin LP. Current Opinion in Solid State and Materials Science 1998;3:558.

[94] Zbib HM, Rubia TDdl. International Journal of Plasticity 2002;18:1133.

[95] Ghoniem N, Tong S, Sun L. Physical Review B 2000;61:913.

[96] Ghoniem N, Huang J, Wang Z. Philosophical Magazine Letters 2002;82:55.

[97] Cai W, Arsenlis A, Weinberger CR, Bulatov VV. J. Mech. Phys. Solids 2006;54:561.

[98] Kocks UF. Polyslip in single crystals of face-centered cubic metals. vol. Ph.D.: Harvard University, 1959.

[99] Lomer WM. Philosophical Magazine 1951;42:1327–1331.

[100] Argon AS. A statistical theory for easy glide II. Cambridge, MA: MIT Press, 1969.

[101] Schoeck G, Frydman R. Physica Stata Solidi B 1972;53:661.

[102] Shin CS, Fivel MC, Rodney D, Phillips R, Shenoy VB, Dupuy L. Formation and strength of dislocation junctions in FCC metals: A study by dislocation dynamics and atomistic simulations. vol. 11. Delft, Netherlands: EDP Sciences, 2001. p.Pr519.

[103] Devincre B, Hoc T, Kubin LP. Materials Science and Engineering A 2005;400-401:182.

[104] Devincre B, Kubin L, Hoc T. Scripta Materialia 2006;54:741.

[105] Schwarz KW. Modelling and Simulation in Materials Science and Engineering 2003;11:609.

[106] Madec R, Devincre B, Kubin LP. In: Kubin LP, Selinger R, Bassani JL, Cho K, editors. Materials Research Society, vol. 653, 2000. p.z1.

[107] Madec R, Devincre B, Kubin L, Hoc T, Rodney D. Science 2003;301:1879.

[108] Madec R, Devincre B, Kubin LP. Physical Review Letters 2002;89:255508/1.

[109] Madec R, Devincre B, Kubin LP. Computational Materials Science 2002;23:219.

[110] Madec R, Kubin LP. Scripta Materialia 2008;58:767.

[111] Madec R DBaKL. Physical Review Letters 2002;89:255508.

[112] Wickham LK, Schwarz KW, Stolken JS. Dislocation forest interactions: simulation and prediction. vol. 578. Boston, MA, USA: Materials Research Society, 2000. p.125.

[113] Wickham LK, Schwarz KW, Stolken JS. Physical Review Letters 1999;83:4574.

[114] Bulatov VV, Hsiung LL, Tang M, Arsenlis A, Bartelt MC, Cai W, Florando JN, Hiratani M, Rhee M, Hommes G, Pierce TG, De La Rubia TD. Nature 2006;440:1174.

[115] Martinez E, Marian J, Arsenlis A, Victoria M, Perlado JM. Philosophical Magazine 2008;88:809.

[116] Madec R. vol. Ph.D.: University of Orsay, 2001.

[117] Akasheh F, Zbib HM, Ohashi T. Philosophical Magazine 2007;87:1307.

[118] Liu ZL, Liu XM, Zhuang Z, You XC. International Journal of Plasticity 2009;25:1436.

[119] Diard O, Leclercq S, Rousselier G, Cailletaud G. International Journal of Plasticity 2005;21:691.

[120] Bielera TR, Eisenlohra P, Rotersa F, Kumarb D, Masonc DE, Crimpb MA, Raabe D. International Journal of Plasticity 2009;25:1655.

[121] Dawson PR, MacEwen SR, Wu P-D. International Materials Reviews 2003;48:86.

[122] Delannay L, Béringhier M, Chastel Y, Mater. REL, Sci. Forum. Simulation of cup-drawing based on crystal plasticity applied to reduced grain samplings. In: Kestens PVHaL, editor. 14th International Conference on Textures of Materials (ICOTOM 14), vol. 495-497. Leuven, Belgium: Trans Tec Publications Inc., 2005. p.1639.

[123] Zamiri A, Pourboghrat F, Barlat F. International Journal of Plasticity 2007;23:1126.

[124] Bhattacharyya A, El-Danaf E, Kalidindi SR, Doherty RD. International Journal of Plasticity 2001;17:861.

[125] Héripré E, Dexet M, Crépin J, Gélébart L, Roos A, Bornert M, Caldemaison D. International Journal of Plasticity 2007;23:1512.

[126] St-Pierre L, Héripré E, Dexet M, Crépin J, Bertolino G, Bilger N. International Journal of Plasticity 2008;24:1516.

[127] Raabe D, Zhao Z, Park SJ, Roters F. Acta Materialia 2002;50:421.

[128] Raabe D, Sachtleber M, Zhao Z, Roters F, Zaefferer S. Acta Materialia 2001;49:3433.

[129] Schroeter BM, McDowell DL. International Journal of Plasticity 2003;19:1355.

[130] Musienko A, Tatschl A, Schmidegg K, Kolednik O, Pippan R, Cailletaud G. Acta Materialia 2007;55:4121.

[131] Poulsen HF, Margulies L, Schmidt S, Winther G. Acta Materialia 2003;51:3821.

[132] Hatem TM, Zikry MA. Philosophical Magazine 2009;89.

[133] Kanjarla AK, Houtte PV, Delannay L. International Journal of Plasticity 2009:In Press.

[134] Lebensohn RA, Brenner R, Castelneau O, Rollett AD. Acta Materialia 2008;56:3914.

[135] Van Houtte P, Peeters B. Effect of deformation-induced intragranular microstructure on plastic anisotropy and deformation textures. vol. 408-412. Seoul, Korea, Republic of: Trans Tech Publications Ltd, 2002. p.985.

[136] Lee BJ, Ahzi S, Parks DM. Journal of Engineering Materials and Technology 2002;124:27.

[137] Engler O, Crumbach M, Li S. Acta Materialia 2005;53:2241.

[138] Al-Fadhalah K, Tome CN, Beaudoin AJ, Robertson IM, Hirth JP, Misra A. Philosophical Magazine 2005;85:1419.

[139] Mahesh S. International Journal of Plasticity 2009;25:752.

[140] Kalidindi SR, Bhattacharya A, Doherty RD. Proceedings of Royal Physical Soceity London 2004;A460:1935.

[141] Erieau P, Rey C. International Journal of Plasticity 2004;20:1763.

[142] Mika DP, Dawson PR. Acta Materialia 1999;47:1355.

[143] Zaefferer S, Kuo JC, Zhao Z, Winning M, Raabe D. Acta Materialia 2003;51:4719.

[144] Ashmawi WM, Zikry MA. Mechanics of Materials 2003;35:537.

[145] Ma A, Roters F, Raabe D. Acta Materialia 2006;54:2181.

[146] Acharya A, Beaudoin AJ, Miller RE. Mathematics and Mechanics of Solids 2008;13:292.

CHAPTER THREE

CRYSTAL PLASTICITY MODEL

The formulation for evolution of dislocation density presented in this section is based on the work of Arsenlis and Parks [1]. Dislocation evolution equations are coupled with the crystal kinematics. Overall crystal plasticity framework is implemented in the user subroutine interface UMAT in ABAQUS^{TM}/Standard using a fully-implicit time integration procedure which is discussed later in this chapter.

3.1 Crystal kinematics

The crystal kinematics briefly reviewed here is based on the work of Asaro and Rice [2]. The deformed configuration of the material with respect to the undeformed material or reference configuration is given by $\mathbf{F} = \frac{\partial \mathbf{x}}{\partial \mathbf{X}}$, which can be further decomposed multiplicatively into elastic ($\mathbf{F^e}$) and plastic ($\mathbf{F^p}$) factors; i.e.

$$\mathbf{F} = \mathbf{F^e F^p} \tag{3.1}$$

where, $\mathbf{F^p}$ maps the neighborhood of the original configuration to an intermediate configuration and describes the effects of plastic deformation on an unrotated and undeformed lattice, and $\mathbf{F^e}$ maps the intermediate neighborhoods to the neighborhood in the deformed configuration. $\mathbf{F^p}$ evolves as follows:

$$\dot{\mathbf{F}}^{\mathbf{p}} = \mathbf{L^p F^p} \tag{3.2}$$

where $\mathbf{L^p}$ is the plastic flow rate.

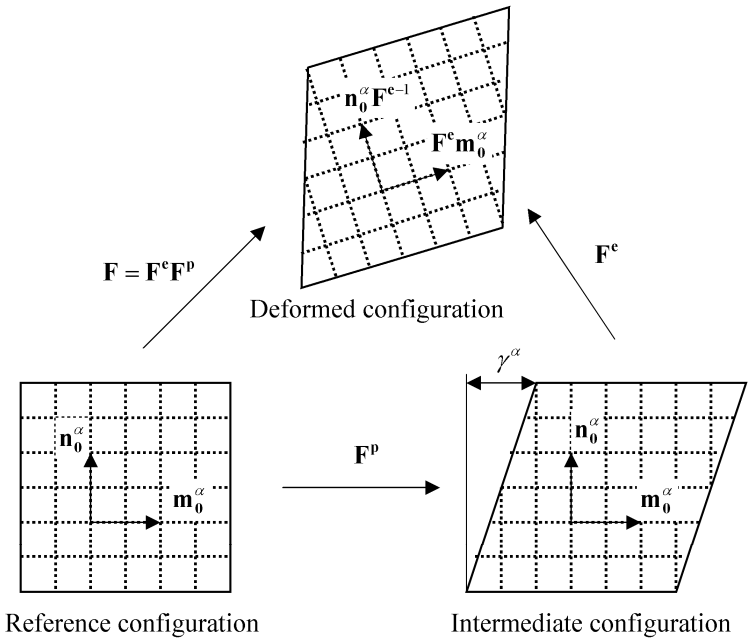

Figure 3.1 Kinematics of slip system activity showing deformation by slip and distortion of the crystal lattice (after Meissonnier et al.[3])

Fig. 3.1 shows a schematic of the deformation by slip and distortion of the crystal lattice. $\mathbf{L}$ is the velocity gradient which gives the slip rate in the current configuration. $\mathbf{L}$ is given by:

$$\mathbf{L} = \frac{\partial \dot{\mathbf{x}}}{\partial \mathbf{x}} = \dot{\mathbf{F}}\mathbf{F}^{-1} = \dot{\mathbf{F}}^{\mathbf{e}}\mathbf{F}^{\mathbf{e}-1} + \mathbf{F}^{\mathbf{e}}\dot{\mathbf{F}}^{\mathbf{p}}\mathbf{F}^{\mathbf{p}}\mathbf{F}^{\mathbf{e}-1} \tag{3.3}$$

where $\mathbf{L}^{\mathbf{e}}$ and $\mathbf{L}^{\mathbf{p}}$ are the elastic and plastic parts respectively of the velocity gradient $\mathbf{L}$. $\mathbf{L}^{\mathbf{p}}$ can be written as:

$$\mathbf{L}^{\mathbf{p}} = \sum_{\alpha=1}^{N} \dot{\gamma}^\alpha \mathbf{m}_0^\alpha \otimes \mathbf{n}_0^\alpha \tag{3.4}$$

where $\mathbf{m}_0^\alpha$ and $\mathbf{n}_0^\alpha$ are the unit vectors in the slip direction and in the slip plane normal direction for slip system α in the reference configuration. N is the number of slip

systems. The motion of dislocations and their interactions related to the plastic shear rate is given by Eq. (3.4).

Evolution of $\mathbf{m}^{\alpha}$ and $\mathbf{n}^{\alpha}$ can be determined by the equations:

$$\begin{aligned} \mathbf{m}^{\alpha} &= \mathbf{F}^{\mathbf{e}}.\mathbf{m}_0^{\alpha} \\ \mathbf{n}^{\alpha} &= \mathbf{n}_0^{\alpha}.\mathbf{F}^{\mathbf{e}-1} \end{aligned} \tag{3.5}$$

$\mathbf{m}^{\alpha}$ and $\mathbf{n}^{\alpha}$ are considered to be orthogonal so that the plastic deformation of the crystal is isochoric. $\mathbf{F}^{\mathbf{e}}$ is determined from the equation:

$$\dot{\mathbf{F}}^{\mathbf{e}} = \left(\mathbf{L} - \mathbf{L}^{\mathbf{p}}\right).\mathbf{F}^{\mathbf{e}} \tag{3.6}$$

or it can be calculated from Eq. (3.1), where **F** is known and $\mathbf{F}^{\mathbf{p}}$ is obtained from the equation:

$$\dot{\mathbf{F}}^{\mathbf{p}} = \left(\sum_{\alpha=1}^{\mathrm{N}} \dot{\gamma}^{\alpha} \mathbf{m}_0^{\alpha} \otimes \mathbf{n}_0^{\alpha}\right).\mathbf{F}^{\mathbf{p}} \tag{3.7}$$

The elastic Green-Lagrange strain corresponding to the intermediate configuration is given by:

$$\mathbf{E}^{\mathbf{e}} = \frac{1}{2}\left(\mathbf{F}^{\mathbf{e}\mathbf{T}}\mathbf{F}^{\mathbf{e}} - \mathbf{I}_2\right) \tag{3.8}$$

where $\mathbf{I}_2$ is a second order identity tensor.

The Piola-Kirchhoff stress tensor $\mathbf{T}^{*}$ is related to the Cauchy stress, σ through:

$$\sigma = \det\left(\mathbf{F}^{\mathbf{e}}\right)^{-1} \mathbf{F}^{\mathbf{e}}\mathbf{T}^{*}\mathbf{F}^{\mathbf{e}\mathrm{T}} \tag{3.9}$$

The Piola-Kirchhoff stress is related to the strain by:

$$\mathbf{T}^{*} = \mathfrak{I}\left[\mathbf{E}^{\mathbf{e}}\right] \tag{3.10}$$

where $\mathfrak{I}$ is the 4$^{\text{th}}$ order stiffness tensor consisting of material elastic moduli.

3.2 Dislocation density framework

Total dislocation density in a plastically deformed material is given by $\rho^T = \rho^G + \rho^S$; where ρ^S is the density of statistically stored dislocations and ρ^G is the density of geometrically necessary dislocations. Further dislocation densities can be sub-classified as right-handed edge, left-handed edge, right-handed screw, and left-handed screw dislocations given by respectively ρ^α_{e+}, ρ^α_{e-}, ρ^α_{s+}, and ρ^α_{s-}. where '*e*' and '*s*' denote the edge and screw dislocation density respectively, and '+' and '-' signs represent the right-handed and left-handed dislocation densities in each type. The plastic shear strain rate is given by:

$$\dot{\gamma}^\alpha = \left(\rho^\alpha_{\mathbf{e}+} \overline{\mathbf{v}}^\alpha_{\mathbf{e}+} + \rho^\alpha_{\mathbf{e}-} \overline{\mathbf{v}}^\alpha_{\mathbf{e}-} + \rho^\alpha_{\mathbf{s}+} \overline{\mathbf{v}}^\alpha_{\mathbf{s}+} + \rho^\alpha_{\mathbf{s}-} \overline{\mathbf{v}}^\alpha_{\mathbf{s}-} \right) \left| \mathbf{b}^\alpha \right| \tag{3.11}$$

where $\overline{v}^\alpha_{xp}$ is the average velocity for dislocation density of type 'x' and polarity 'p' on slip system α. **b** is the Burgers vector. Dislocation flux is given by $\rho^\alpha_{xp} \overline{v}^\alpha_{xp}$ such that the positive sense of dislocation density increases the dislocation flux and hence the plastic shear rate.

Considering the three process; generation, annihilation (dynamic recovery) and accumulation/loss associated with the flux divergence, the evolution of dislocation density is given by:

$$\dot{\rho}^\alpha = \dot{\rho}^\alpha_{gen} + \dot{\rho}^\alpha_{ann} + \dot{\rho}^\alpha_{flux} \tag{3.12}$$

Generation and annihilation terms are statistical in nature and do not affect the geometric character of the dislocation density within the volume element. The geometric character of dislocations is affected by the flux divergence term $\dot{\rho}^\alpha_{flux}$. Fig. 3.2 schematically shows expansion of a dislocation loop lying on the plane of paper when a

shear stress in the '+' X direction is applied. $\vec{t}$ represents the line sense of a dislocation segment. The generation terms for each density type are given by:

$$\dot{\rho}^{\alpha}_{e+(gen)} = \dot{\rho}^{\alpha}_{e-(gen)} = \frac{\rho^{\alpha}_{s+}\left|\overline{v}^{\alpha}_{s+}\right|}{\overline{l}^{\alpha}_{s+}} + \frac{\rho^{\alpha}_{s-}\left|\overline{v}^{\alpha}_{s-}\right|}{\overline{l}^{\alpha}_{s-}}$$
$$\dot{\rho}^{\alpha}_{s+(gen)} = \dot{\rho}^{\alpha}_{s-(gen)} = \frac{\rho^{\alpha}_{e+}\left|\overline{v}^{\alpha}_{e+}\right|}{\overline{l}^{\alpha}_{e+}} + \frac{\rho^{\alpha}_{e-}\left|\overline{v}^{\alpha}_{e-}\right|}{\overline{l}^{\alpha}_{e-}} \tag{3.13}$$

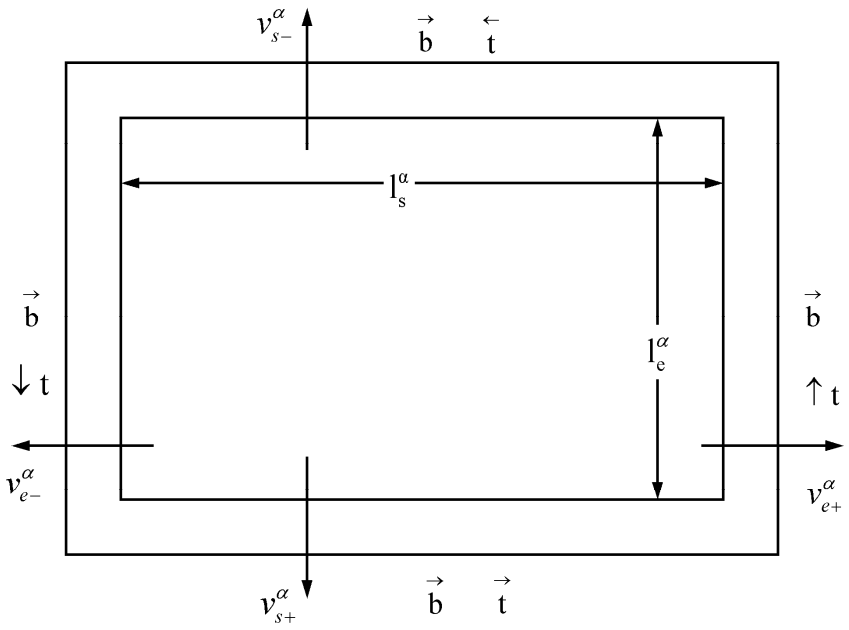

Figure 3.2 Schematic of an expanding dislocation loop idealized as a composition of discrete edge and screw line segments forming a closed loop (after Arsenlis and Parks [1]).

where $\overline{l}^{\alpha}_{xp}$ is the average dislocation segment length; subscripts and superscripts have the same sense as for average dislocation velocity. Evolution of dislocation density and

activity of dislocation sources is mainly affected by the evolution of dislocation segment lengths which are given by:

$$\begin{aligned} \overline{l}_{e+}^{\alpha} &= \overline{l}_{e-}^{\alpha} = 1 \Big/ \sqrt{\sum_{\beta=1}^{N} \left(H_{ee}^{\alpha\beta} \rho_e^{\beta} + H_{es}^{\alpha\beta} \rho_s^{\beta} \right)} \\ \overline{l}_{s+}^{\alpha} &= \overline{l}_{s-}^{\alpha} = 1 \Big/ \sqrt{\sum_{\beta=1}^{N} \left(H_{se}^{\alpha\beta} \rho_e^{\beta} + H_{ss}^{\alpha\beta} \rho_s^{\beta} \right)} \end{aligned} \tag{3.14}$$

where $H_{xy}^{\alpha\beta}$ are dislocation strength interaction matrices as described in [1]. $H_{xy}^{\alpha\beta}$ represents interaction of a dislocation of type '*x*' on slip system α with a dislocation of type '*y*' on slip system β (forest).

The dislocation density annihilation equations are given by:

$$\begin{aligned} \dot{\rho}_{e+(ann)}^{\alpha} &= \dot{\rho}_{e-(ann)}^{\alpha} = -\rho_{e+}^{\alpha} \rho_{e-}^{\alpha} R_e \left(\left| \overline{v}_{e+}^{\alpha} \right| + \left| \overline{v}_{e-}^{\alpha} \right| \right) \\ \dot{\rho}_{s+(ann)}^{\alpha} &= \dot{\rho}_{s-(ann)}^{\alpha} = -\rho_{s+}^{\alpha} \rho_{s-}^{\alpha} R_s \left(\left| \overline{v}_{s+}^{\alpha} \right| + \left| \overline{v}_{s-}^{\alpha} \right| \right) \end{aligned} \tag{3.15}$$

where R_e and R_s are the critical capture radii for the edge and screw dislocations. The critical capture radii decide the minimum distance to which two parallel Burgers vector dislocations can come before they annihilate each other. In a macroscopic view, the saturation values of the edge and screw dislocations densities are decided by these critical capture radii [1]. A similar argument is given by Kubin et al.[4] about the critical radii of the stress field of screw dislocations referring to their annihilation activity.

The slip system indices are used as described by Schmid and Boas [5] (see also English version by Schmid [6]). A, B, C and D represent 4 slip planes namely $\left(1\,\overline{1}\,\overline{1}\right)$, $\left(111\right)$, $\left(1\,\overline{1}1\right)$, and $\left(\overline{1}\,\overline{1}1\right)$ respectively. 1, 2, 3, 4, 5, and 6 representing the six directions of Burgers vectors in the FCC crystal given by $\left[011\right]$, $\left[01\,\overline{1}\right]$, $\left[101\right]$, $\left[10\,\overline{1}\right]$, $\left[110\right]$, and

$\left[1\,\bar{1}0\right]$. A [100] stereographic projection is presented in Fig. 3.3 which shows 24 standard triangles with few slip systems. Table A.1 in Appendix A shows the slip directions ($\mathbf{m}_0^\alpha$) and slip plane normal ($\mathbf{n}_0^\alpha$) in the reference frame for FCC crystals.

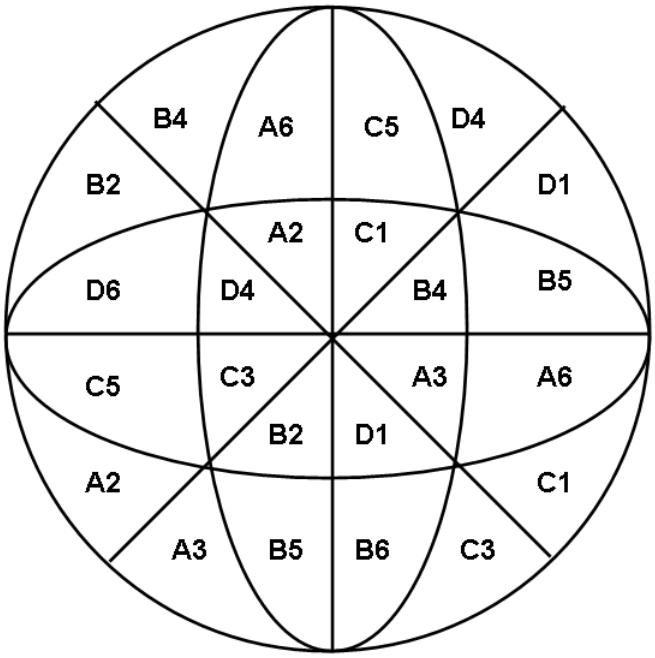

Figure 3.3 Stereographic project from [100] showing slip systems on 24 standard triangles (after Wu et al. [7]). Note that all slip systems are not visible in this projection. Slip system notation is after Schmid and Boas [6].

3.3 Evolution of slip resistance

Dislocation resistance is modeled primarily by forest dislocation density interactions but glide dislocations and dislocations in parallel gliding planes are also taken into account. Gliding dislocations increase the slip resistance to slip on parallel slip planes [8]. In the

present work dislocation slip resistance is represented in a Taylor type equation of hardening given by:

$$S_{de}^{\alpha} = \mu b \sqrt{\sum_{\beta=1}^{N} \left(G_{ee}^{\alpha\beta} \rho_e^{\beta} + G_{es}^{\alpha\beta} \rho_s^{\beta} \right)}$$
$$S_{ds}^{\alpha} = \mu b \sqrt{\sum_{\beta=1}^{N} \left(G_{se}^{\alpha\beta} \rho_e^{\beta} + G_{ss}^{\alpha\beta} \rho_s^{\beta} \right)} \tag{3.16}$$

where S_{de}^{α} is the slip resistance on edge mobile dislocations on slip system α due to forest dislocations of type edge and screw on slip system β. S_{ds}^{α} is the slip resistance on screw mobile dislocations on slip system α due to forest dislocations of type edge and screw on slip system β. Finally, ρ_e^{β} is the total edge dislocation density on slip system β and ρ_s^{β} is the total screw dislocation density on slip system β [1] given by:

$$\rho_e^{\beta} = \rho_{e^+}^{\beta} + \rho_{e^-}^{\beta}$$
$$\rho_s^{\beta} = \rho_{s^+}^{\beta} + \rho_{s^-}^{\beta} \tag{3.17}$$

$G_{xy}^{\alpha\beta}$ are dislocation strength interaction matrices as described in [1]. $G_{xy}^{\alpha\beta}$ represents interaction of a dislocation of type '*x*' on slip system α with a dislocation of type '*y*' on slip system β.

Dislocation strength interaction matrices consist of 6 independent coefficients namely G_0, G_1, G_2, G_3, G_4, G_5. G_0 represents in-plane interaction of dislocations with the same Burgers vectors and G_1 represents interaction of dislocations with different Burgers vectors and on the same gliding plane. Coefficients $G_2 - G_5$ represent out of plane interactions and are related to four different types of junctions/locks which glide dislocations make with forest dislocations. These are called Hirth junction, collinear lock, glissile junction, and Lomer junction respectively. A detailed study on hardening and

interaction of slip systems has been done by Franciosi and Zaoui [9, 10]. Though it is suggested [9] that the hardening matrix should depend on the stress state (dislocation density), we do not consider evolution of the matrix during deformation. Constitutive behavior equations for the velocity of dislocations have been used as given in reference [1] and will be introduced later while we discuss time integration procedure in section 3.5.

3.4 Crystallographic texture update algorithm

In this section, three different methods of texture update algorithm are reviewed.

(i) The first two methods are based on an update of the orientation matrix for each grain based on the change in orientation which is determined using polar decomposition of the elastic part of the deformation gradient ($\mathbf{F^e}$).

$$\mathbf{R}' = \mathbf{F^e R} \tag{3.18}$$

$$\mathbf{R}' = \mathbf{R^* R} \tag{3.19}$$

with $\mathbf{R}$ being the initial (Lagrangian) orientation matrix for each grain and $\mathbf{R^*}$ the orthogonal rotation tensor obtained using polar decomposition of $\mathbf{F^e}$ i.e.

$$\mathbf{F^e} = \mathbf{R^* U} \tag{3.20}$$

$\mathbf{U}$ is the displacement tensor in the intermediate configuration. For small elastic strains (e.g. metals) both Eq (3.18) and Eq (3.19) produce the same results. In case of large elastic strains the second equation is more accurate [11].

(ii) In the third method, $\mathbf{R}$ in the previous configuration is used to calculate $\mathbf{R}$ in the next time step.

$$\dot{\mathbf{R}} = \mathbf{W}^{*}\mathbf{R} \tag{3.21}$$

where $\mathbf{W}^{*}$ is the elastic part of the spin tensor and is given by $\mathbf{W}^{*} = \mathbf{W} - \mathbf{W}^{\mathbf{p}}$. $\mathbf{W}$ is the anti-symmetric part of the velocity gradient tensor and is given by:

$$\mathbf{W} = \frac{1}{2}\left(\mathbf{L} - \mathbf{L}^{\mathbf{T}}\right) \tag{3.22}$$

$\mathbf{W}^{\mathbf{p}}$ is the plastic part of the spin tensor and is given by

$$\mathbf{W}^{\mathbf{p}} = \sum_{\alpha} \dot{\gamma}^{\alpha} \Omega^{\alpha} \tag{3.23}$$

where Ω^{α} is the anti-symmetric part of the Schmid matrix in the current configuration given by:

$$\Omega^{\alpha} = \frac{1}{2}\left(\mathbf{m}^{\alpha} \otimes \mathbf{n}^{\alpha} - \mathbf{n}^{\alpha} \otimes \mathbf{m}^{\alpha}\right) \tag{3.24}$$

$\mathbf{m}^{\alpha}$ and $\mathbf{n}^{\alpha}$ are slip direction vectors and slip plane normal vectors respectively in the current configuration. The orientation change is then given by:

$$\Delta\mathbf{R} = \left(\mathbf{W}\Delta t - \sum_{\alpha} \dot{\gamma}^{\alpha} \Omega^{\alpha} \Delta t\right)\mathbf{R} \tag{3.25}$$

The results presented in the current work are obtained using the first scheme. The orthogonal rotation matrix $\mathbf{R}'$ obtained here is also called the orientation matrix and is used to determine Euler angles for each grain. Orientation matrix is represented in the passive convention by the direction cosine matrix of the Euler angles (Bunge's notation) φ_1, Φ, and φ_2. See section A.2 in Appendix A.

3.5 Time integration procedure

The crystal plasticity framework described in the previous section is numerically integrated using a fully-implicit time integration procedure. The crystal kinematics framework and the dislocation density framework are implemented using a user interface subroutine UMAT in the commercially available FEM package ABAQUS^{TM}/Standard [12]. The variables passed as input to the UMAT are total deformation gradient at time *t* ($\mathbf{F}(t)$) and the Cauchy stress at time *t* ($\sigma(t)$). The UMAT is implemented with a fully-implicit Newton-Raphson scheme to give state-dependent variables namely dislocation densities, dislocation density evolution rates, and the plastic deformation gradient ($\mathbf{F}^{\mathrm{p}}(t)$) at time $\tau = t + \Delta t$. This chapter focuses on the equations which are set up for updating the stress and state variables in the new time increment.

The time integration procedure is inspired by the work of Kalidindi et al.[13] which the authors describe as a two-level scheme. In this approach, the stress is determined in the first level of the Newton-Raphson method while slip resistance, dislocation density and dislocation velocities are updated in the second level. t_n and t_{n+1} are current time at the beginning and end of a time increment given by $\Delta t = t_{n+1} - t_n$. For each iteration, state variables (dislocation densities and dislocation evolution rates), state dependent variables (slip resistance) S_{di}^{α}, the Cauchy stress (σ) and material Jacobian matrix $\frac{\partial \sigma}{\partial \varepsilon}$ are needed.

i varies from 1 to 2; 1 being for edge dislocations and 2 being for screw dislocations.

It is assumed that at time t_n, σ_n, $\mathbf{F}_n^{\mathrm{p}}$, and S_{di}^{α} are known.

Applying a fully-implicit time integration of Eq (3.2), $\mathbf{F}_{n+1}^{\mathrm{p}}$ is given by:

$$\mathbf{F}_{n+1}^{\mathrm{p}} = \left(\mathbf{1} + \Delta t \mathbf{L}^{\mathrm{p}}\right)\mathbf{F}_n^{\mathrm{p}} \tag{3.26}$$

Eq (3.26) can be re-written as given below by using Eq (3.4):

$$\mathbf{F}^{\mathrm{p}}_{n+1} = \left(1 + \sum_{\alpha=1}^{N} \Delta\gamma^{\alpha} \mathbf{P}^{\alpha}\right) \mathbf{F}^{\mathrm{p}}_{n} \tag{3.27}$$

Also,

$$\mathbf{F}^{\mathrm{p\text{-}1}}_{n+1} = \mathbf{F}^{\mathrm{p\text{-}1}}_{n} \left(1 - \sum_{\alpha=1}^{N} \Delta\gamma^{\alpha} \mathbf{P}^{\alpha}\right) \tag{3.28}$$

where $\mathbf{P}^{\alpha} = \mathbf{m}^{\alpha}_{0} \otimes \mathbf{n}^{\alpha}_{0}$ is the Schmid tensor.

Eq (3.11) shows that $\dot{\gamma}^{\alpha} = \dot{\gamma}^{\alpha}\left(\rho, v\right)$; where ρ is dislocation density and v is dislocation velocity which in turn depend upon the resolved shear stress (τ^{α}) and slip resistance (S^{α}_{di}) on each slip system. Also ignoring the small elastic strain in metallic materials, the resolved shear stress (τ^{α}) is given by:

$$\tau^{\alpha} \approx \mathbf{T}^{*} : \mathbf{P}^{\alpha} \tag{3.29}$$

Therefore $\dot{\gamma}^{\alpha}$ can be written as:

$$\dot{\gamma}^{\alpha} = \dot{\gamma}^{\alpha}\left(\mathbf{T}^{*}, S^{\alpha}_{di}\right) \tag{3.30}$$

The slip increment $\Delta\gamma^{\alpha}$ is defined in terms of the weighted average of the slip rate at t_n and t_{n+1}:

$$\Delta\gamma^{\alpha} = \left[(1\text{-}\omega).\dot{\gamma}_{\mathrm{t_n}} + \omega.\dot{\gamma}_{\mathrm{t_{n+1}}}\right]\Delta t \tag{3.31}$$

where ω is a weighting factor. $\omega = 0$ corresponds to the Euler forward (explicit) and $\omega \neq 0$ to the Euler backward (fully-implicit) integration. $\omega = 0.5$ is the trapezoidal rule.

Using Eq (3.1) and Eq (3.28), the following relation can be established [13]:

$$\mathbf{F}^{\mathrm{p\text{-}T}}_{n+1} \mathbf{F}^{\mathrm{T}}_{n+1} \mathbf{F}_{n+1} \mathbf{F}^{\mathrm{p\text{-}1}}_{n+1} = \mathbf{A} - \sum_{\alpha=1}^{\mathbf{n}_{\alpha}} \Delta\gamma^{\alpha} \mathbf{B}^{\alpha} \tag{3.32}$$

where

$$\mathbf{A} \equiv \mathbf{F}_n^{\text{p-T}} \mathbf{F}_{n+1}^{\text{T}} \mathbf{F}_{n+1} \mathbf{F}_n^{\text{p-1}} \text{ and } \mathbf{B}^\alpha \equiv \left(\mathbf{P}^{\alpha^{\text{T}}} \mathbf{A} + \mathbf{A} \mathbf{P}^\alpha \right) \tag{3.33}$$

Using Eq (3.32) and the Eq (3.33) $\mathbf{T}^*$ is obtained as:

$$\mathbf{T}^* \approx \mathbf{T}^{*\text{tr}} - \sum_{\alpha=1}^{\mathbf{n}_\alpha} \Delta\gamma^\alpha \mathbf{C}^\alpha \tag{3.34}$$

where

$$\mathbf{C}^\alpha \equiv \mathfrak{I}\left[(1/2) \mathbf{B}^\alpha \right] \tag{3.35}$$

$$\mathbf{T}^{*\text{tr}} \equiv \frac{1}{2} \mathfrak{I}(\mathbf{A} - \mathbf{1}) \tag{3.36}$$

First, Eq (3.34), which is a set of non-linear equations in $\mathbf{T}^*$ and $\Delta\gamma^\alpha$, is solved using a Newton-Raphson type root-finding scheme given by the following equation. From now on the symbol '(τ)' will be used for time t_{n+1} and the n^{th} iteration of the Newton-Raphson will be represented by an '*n*' in the subscript.

$$\mathbf{T}_{n+1}^* (\tau) = \mathbf{T}_n^* (\tau) - \kappa_n^{-1} \left[\mathbf{G}_n \right] \tag{3.37}$$

$$\mathbf{G}_n \equiv \mathbf{T}_n^* (\tau) - \mathbf{T}^{*\text{tr}} + \sum_{\alpha=1}^{\mathbf{n}_\alpha} \Delta\gamma^\alpha \left(\mathbf{T}_n^* (\tau), \left(S_{di}^\alpha \right)_k (\tau) \right) \mathbf{C}^\alpha \tag{3.38}$$

κ_n is the tangent matrix for Newton-Raphson scheme given by:

$$\kappa_n \equiv \mathbf{I} + \sum_{\alpha=1}^{\mathbf{n}_\alpha} \mathbf{C}^\alpha \otimes \frac{\partial \Delta\gamma^\alpha \left(\mathbf{T}_n^* (\tau), \left(S_i^\alpha \right)_k (\tau) \right)}{\partial \mathbf{T}_n^* (\tau)} \tag{3.39}$$

and $$\gamma^\alpha \left(\mathbf{T}_n^* (\tau), \left(S_{di}^\alpha \right)_k (\tau) \right) \equiv \gamma^\alpha \left(\left(\rho_j^\alpha \right)_k (\tau), \left(v_j^\alpha \right)_k (\tau) \right) \tag{3.40}$$

where *j* varies from 1 to 4 and denotes the 4 types of dislocation densities as described in Eq. (3.11). $\left(S_{di}^\alpha \right)_k$ is the *k*th update in S_{di}^α after *n+1* iterations of the N-R method.

Similarly $\left(\rho_j^\alpha\right)_k$ and $\left(v_j^\alpha\right)_k$ represent the *k*th update in the dislocation densities and dislocation velocities after $n+1$ iterations of the N-R method. From Eq. (3.40) it is evident that:

$$\frac{\partial \Delta\gamma^\alpha\left(\mathbf{T}_n^*(\tau),\left(S_{di}^\alpha(\tau)\right)_k\right)}{\partial \mathbf{T}_n^*(\tau)} = \frac{\partial \Delta\gamma^\alpha\left(\left(\rho_i^\alpha\right)_k(\tau),\left(v_j^\alpha\right)_k(\tau)\right)}{\partial \mathbf{T}_n^*(\tau)} \tag{3.41}$$

N-R scheme is applied for a very small increment, and $\left(\rho_j^\alpha\right)_k(\tau)$ is assumed to be constant for determination of $\frac{\partial \Delta\gamma^\alpha\left(\left(\rho_j^\alpha\right)_k(\tau),\left(v_j^\alpha\right)_k(\tau)\right)}{\partial \mathbf{T}_n^*(\tau)}$, viz

$$\frac{\partial \Delta\gamma^\alpha\left(\left(\rho_j^\alpha\right)_k(\tau),\left(v_j^\alpha\right)_k(\tau)\right)}{\partial \mathbf{T}_n^*(\tau)} = \left(\rho_j^\alpha\right)_k \frac{\partial \Delta\gamma^\alpha\left(\left(v_j^\alpha\right)_k\right)}{\partial \mathbf{T}_n^*(\tau)} \tag{3.42}$$

Dislocation densities are simply updated using:

$$\left(\rho_{xp}^\alpha\right)_{k+1} = \left(\rho_{xp}^\alpha\right)_k + \Delta t^{'}\left(\dot{\rho}_{xp}^\alpha\right)_k \tag{3.43}$$

where $\Delta t^{'}$ is the sub-increment in the N-R scheme.

Slip resistances are integrated using:

$$\left(S_{de}^\alpha\right)_{k+1} = \mu b\sqrt{\sum_\beta\left\{G_{ee}^{\alpha\beta}\left(\rho_e^\beta\right)_{k+1} + G_{es}^{\alpha\beta}\left(\rho_s^\beta\right)_{k+1}\right\}} \tag{3.44}$$

$$\left(S_{ds}^\alpha\right)_{k+1} = \mu b\sqrt{\sum_\beta\left\{G_{se}^{\alpha\beta}\left(\rho_e^\beta\right)_{k+1} + G_{ss}^{\alpha\beta}\left(\rho_s^\beta\right)_{k+1}\right\}} \tag{3.45}$$

τ_{n+1}^α can be updated using Eq (3.29). Now that we have τ_{n+1}^α, $\left(S_{de}^\alpha\right)_{k+1}$, and $\left(S_{ds}^\alpha\right)_{k+1}$, dislocation velocities can be updated using:

$$\left(\overline{v}_e^\alpha\right)_{k+1} = v_0\exp\left\{-\frac{F_0}{kT}\left(1-\left(\frac{\left|\tau_{n+1}^\alpha\right|}{\left(S_{de}^\alpha\right)_{k+1}}\right)^p\right)^q\right\} \tag{3.46}$$

and

$$\left(\bar{v}_s^{\alpha}\right)_{k+1} = v_0 \exp\left\{-\frac{F_0}{kT}\left(1-\left(\frac{\left|\tau_{n+1}^{\alpha}\right|}{\left(S_{ds}^{\alpha}\right)_{k+1}}\right)^{p}\right)^{q}\right\} \tag{3.47}$$

where, T is absolute temperature, k is Boltzmann's constant, F_0 is the total free energy required to overcome the slip resistance, and p, q, and v_0 are exponential and pre-exponential constants.

The procedure for determination of $\frac{\partial \mathbf{T}}{\partial \mathbf{E}}$ is described in the next section which is needed for determination of the material Jacobian matrix $\frac{\partial \sigma}{\partial \varepsilon}$ [3]. $\mathbf{T}$ is the second Piola-Kirchhoff stress tensor pushed forward to the intermediate configuration. $\mathbf{E}$ is the total Green-Lagrange strain tensor defined by $\mathbf{E} = \frac{\mathbf{1}}{\mathbf{2}}\left(\mathbf{F}^{\mathrm{T}}\mathbf{F} - \mathbf{I}\right)$.

3.5.1 Determination of the tangent matrix $\frac{\partial \mathbf{T}}{\partial \mathbf{E}}$

The determination of $\frac{\partial \mathbf{T}}{\partial \mathbf{E}}$ is obtained following the work of Meissonnier et al. [3]. A two-level update method is used coupled with Newton-Raphson algorithm as suggested by Kalidindi et al [13]. Since a two-level update algorithm is used in which slip resistance is not determined in a single update along with stress $\mathbf{T}$, it is exclude from the procedure employed for determination for $\frac{\partial \mathbf{T}}{\partial \mathbf{E}}$. Hence all the derivatives used for slip resistance S_{di}^{α} are excluded in this procedure and the remainder of the algorithm is the

same as given by Meissonnier et al. [3]. All the mathematical operations used here have their usual meaning and are listed in Table A.3 in Appendix A.

$$\frac{\partial \mathbf{T}}{\partial \mathbf{E}} = \left(\det \mathbf{F}^{\mathrm{p}}\right)\left(\mathbf{F}^{\mathrm{p}} \underline{\otimes} \mathbf{F}^{\mathrm{p}}\right)^{-1} : \left(\frac{\partial \mathbf{T}^{*}}{\partial \mathbf{E}} + \left[\mathbf{T}^{*} \otimes \mathbf{F}^{\mathrm{p}^{-\mathrm{T}}} - \left(\det \mathbf{F}^{\mathrm{p}}\right)^{-1}\left[1 \underline{\otimes}\left(\mathbf{T}\mathbf{F}^{\mathrm{p}\mathrm{T}}\right)^{\mathrm{T}} + \left(\mathbf{F}^{\mathrm{p}}\mathbf{T}\right)\bar{\otimes}1\right]\right] : \frac{\partial \mathbf{F}^{\mathrm{p}}}{\partial \mathbf{E}}\right)$$

(3.48)

where $\frac{\partial \mathbf{F}^{\mathrm{p}}}{\partial \mathbf{E}}$ is given by:

$$\frac{\partial \mathbf{F}^{\mathrm{p}}}{\partial \mathbf{E}} = \sum_{\alpha=1}^{\mathbf{n}_{\alpha}} \left(\mathbf{P}_{\alpha}\mathbf{F}_{\mathbf{n}}^{\mathrm{p}}\right) \otimes \frac{\partial \Delta\gamma^{\alpha}}{\partial \mathbf{E}} \tag{3.49}$$

and $\frac{\partial \mathbf{T}^{*}}{\partial \mathbf{E}}$ is determined using a linear system of equations given by:

$$\Re : \frac{\partial \mathbf{T}^{*}}{\partial \mathbf{E}} = \frac{\partial \mathbf{T}^{\mathrm{tr}}}{\partial \mathbf{E}} - \sum_{\alpha=1}^{\mathbf{n}_{\alpha}} \Delta\gamma^{\alpha} \frac{\partial \mathbf{C}^{\alpha}}{\partial \mathbf{E}} \tag{3.50}$$

where $\Re$ is given by:

$$\Re \equiv 1 \underline{\otimes} 1 + \sum_{\alpha=1}^{N} \left(\mathbf{C}^{\alpha} \otimes \frac{\partial \Delta\gamma^{\alpha}}{\partial \mathbf{E}}\right) \tag{3.51}$$

where $\frac{\partial \mathbf{T}^{\mathrm{tr}}}{\partial \mathbf{E}}$ is given by:

$$\frac{\partial \mathbf{T}^{\mathrm{tr}}}{\partial \mathbf{E}} = \Im : \left(\mathbf{F}^{\mathrm{p}\text{-}1} \underline{\otimes} \mathbf{F}^{\mathrm{p}\text{-}1}\right) \tag{3.52}$$

and $\frac{\partial \mathbf{C}^{\alpha}}{\partial \mathbf{E}}$ is given by:

$$\frac{\partial \mathbf{C}^{\alpha}}{\partial \mathbf{E}} = \Im : \left[\mathbf{F}^{\mathrm{p}\text{-}\mathrm{T}} \underline{\otimes}\left(\mathbf{F}^{\mathrm{p}\text{-}1}\mathbf{P}^{\alpha}\right)^{\mathrm{T}} + \left(\mathbf{F}^{\mathrm{p}\text{-}1}\mathbf{P}^{\alpha}\right)^{\mathrm{T}} \underline{\otimes} \mathbf{F}^{\mathrm{p}\text{-}\mathrm{T}}\right] \tag{3.53}$$

References

[1] Arsenlis A, Parks DM. J. Mech. Phys. Solids 2002;50:1979.

[2] Asaro RJ, Rice JR. J. Mech. Phys. Solids 1977;25:309.

[3] Meissonnier FT, Busso EP, O'Dowd NP. International Journal of Plasticity 2001;17:601.

[4] Kubin L, Canova G, Condat M, Devincre B, Pontikis V, Bréchet Y. Diffusion and Defect Data—Solid State Data, Part B (Solid State Phenomena) 1992;23-24:455.

[5] Schmid E, Boas W. Kristallplastizität, mit besonderer Berüchsichtigung der Metalle. Berlin: Springer, 1935.

[6] Schmid E. Kristallplastizität, mit besonderer Berüchsichtigung der Metalle. English

Plasticity of crystals, with special reference to metals, by E. Schmid and W. Boas; [translated from the German by F.A. Hughes & Co.]. London: Chapman & Hall, 1968.

[7] Wu T-Y, Bassani JL, Laird C. Proceedings of Royal Society-Mathematical and Physical Sciences 1991;435:1.

[8] Argon AS. A statistical theory for easy glide II. Cambridge, MA: MIT Press, 1969.

[9] Franciosi P, Zaoui A. Acta Metallurgica 1982;30:1627.

[10] Franciosi P. FCC single crystals hardening anisotropy and stacking fault energy. vol. 1. Montreal, Que, Can: Pergamon Press (International Series on the Strength and Fracture of Materials and Structures), 1986. p.281.

[11] Ling X, Horstemeyer MF, Potirniche GP. International Journal for Numerical Methods in Engineering 2005;63:548.

[12] ABAQUS Reference Manual Versions 6.5. Providence, RI: ABAQUS Inc., 2005.

[13] Kalidindi SR, Bronkhorst CA, Anand L. Journal of Mechanics and Physics of Solids 1992;40:537.

CHAPTER FOUR

DETERMINATION OF AVERAGE DISLOCATION INTERACTION STRENGTHS USING DISLOCATION DYNAMICS

As discussed in Chapter two, hardening laws play a key role in predicting the plastic anisotropic behavior of single crystals, which in turn sets up the building block for prediction of the overall crystallographic texture evolution and microstructure evolution (including dislocation patterning). In this chapter determination of hardening coefficients used in the current CPFEM model using an application of 3D discrete dislocation dynamics is discussed. The determination of these hardening parameters using a 3DDD model such as shown herein can be of great importance for obtaining an appropriate initial estimate in finding a reasonable set of hardening coefficients. This chapter focuses only on the latent hardening coefficients.

4.1 Simulation details

In the simulation cells, dislocations are populated in such a way that on the application of stress only one type of junction is formed. The result is a specific junction of dislocations on mobile and forest systems. The strength of these junctions is determined using the critical resolved shear stress on the mobile slip system and the forest dislocation density which is given by a Taylor equation.

$$\tau_c^{\alpha} = \mu b \sqrt{\sum_{\beta} a^{\alpha\beta} \rho^{\beta}} \tag{4.1}$$

Here, τ_c^α is the critical resolved shear stress (RSS) on the mobile slip system α, ρ^β is the dislocation density on the forest slip system β. μ is the shear modulus and *b* is the magnitude of the Burgers vector.

In the CPFEM model presented here the slip resistance is given by Eqs. (3.16). For readability, these equations are again presented here.

$$S_{de}^\alpha = \mu b \sqrt{\sum_\beta \left(G_{ee}^{\alpha\beta} \rho_e^\beta + G_{es}^{\alpha\beta} \rho_s^\beta \right)}$$
$$S_{ds}^\alpha = \mu b \sqrt{\sum_\beta \left(G_{se}^{\alpha\beta} \rho_e^\beta + G_{ss}^{\alpha\beta} \rho_s^\beta \right)} \quad (4.2)$$

where symbols are as described in Chapter Three, Eq (3.16). As used in the above equations, the forest dislocation densities are divided into edge and screw type dislocations and different hardening coefficients are envisioned for the edge (mobile)-edge (forest), edge(mobile)-screw(forest), screw(mobile)-edge(forest), and screw(mobile)-screw(forest) dislocations. However, for simplicity we consider average strength of dislocation interactions and therefore use identical hardening coefficients as described in Eq. (4.1). Rather than giving edge and screw dislocations different treatments, we determine the hardening coefficients which would be applicable to an overall ensemble of mixed types of dislocations.

Material constants (e.g. elastic stiffness, stacking fault energy etc.) for pure aluminum are used. The shear modulus is 26.1 GPa and the magnitude of the Burgers vector is 2.86E-10 m. $a^{\alpha\beta}$ is the latent hardening coefficient of interest. In each simulation, the mobile system is given by ½[0 1 1](1 1 -1) and the forest slip system varies according to the junction of interest. The forest and mobile slip systems used for the simulations are shown in Table 4.1. Each simulation cell is a cubic cell of size

$(35000b)^3$ (~ 10 μm $)^3$. All the simulations were done at a constant strain rate of 20 s^{-1} up to a total strain of ~ 1E-03. Cross-slip is disabled for all simulations to avoid reactions by cross-slip.

Table 4.1 Forest and mobile slip systems for different junctions. After Devincre et al. [1]

Junction/Lock Type	Mobile system	Forest system
Hirth	½[0 1 1](1 1 -1)	½[0 1 -1](1 1 1)
		½[0 1 -1](-1 1 1)
Glissile	½[0 1 1](1 1 -1)	½[-1 0 1](1 -1 1)
		½[-1 1 0](1 1 1)
Lomer-Cottrell	½[0 1 1](1 1 -1)	½[-1 0 1](1 1 1)
		½[1 1 0](-1 1 1)
Collinear	½[1 0 -1](1 -1 1)	½[1 0 -1](1 1 1)

The forest dislocation density (ρ_f) is 1 x 10^{12} m^{-2} and the mobile dislocation density (ρ_m) is $\frac{\rho_f}{5}$. All dislocations on forest and mobile slip systems are sets of randomly selected edge and screw type dislocations. On forest slip systems, all screw dislocations are aligned in the X direction of the simulation cell and the edge dislocations are in the Y direction. Fig. 4.1 shows a typical initial configuration of dislocations in the simulation cell (for the Lomer junction in the picture). Resolved shear stress on the forest slip system is zero, therefore forest dislocation density does not evolve. Also, the interactions between dislocations on the same slip systems are disabled. In an effort to

account for junction formation only, we disable attractive or repulsive interactions of dislocations (including dipoles) on the same slip systems. To further minimize the change to the forest dislocation density during the slip process, periodic boundary conditions are employed so that the dislocations remain straight due to line tension.

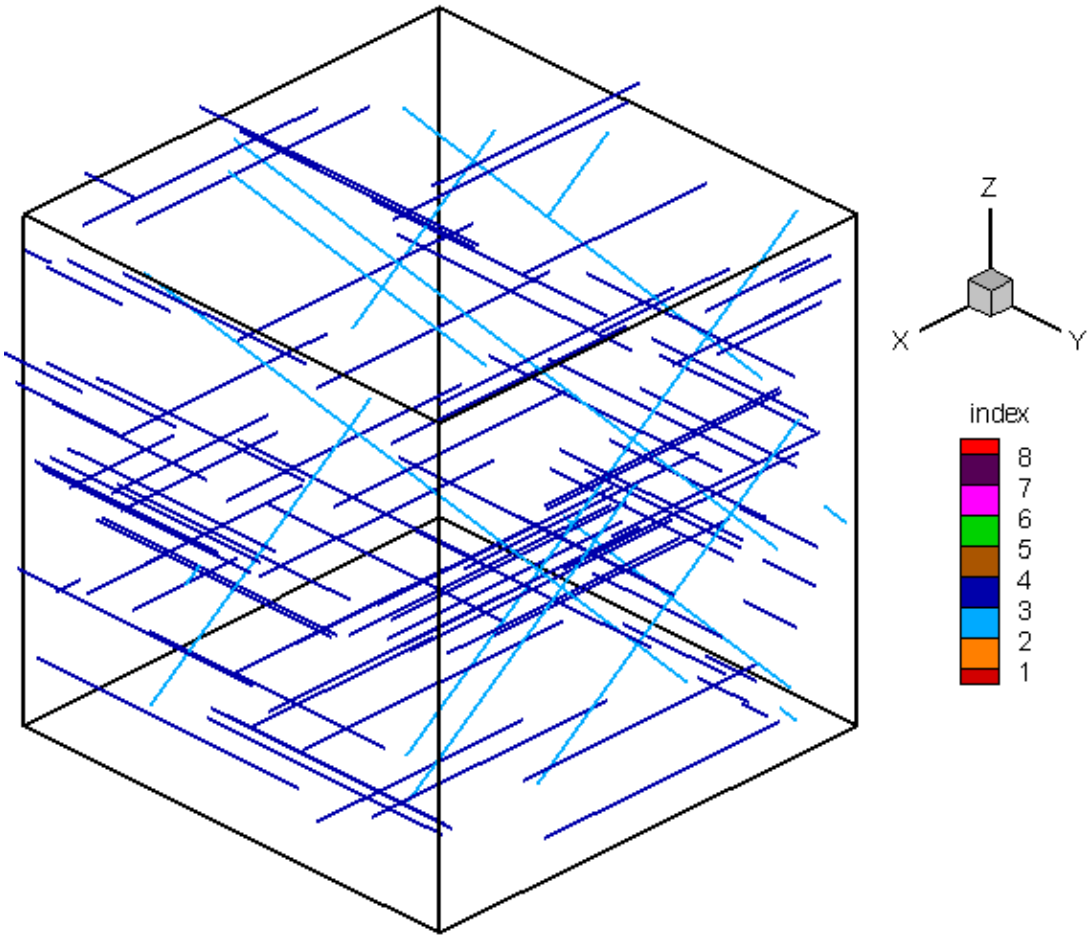

Figure 4.1 Initial configurations of the dislocations in the simulation cell. Dark colored lines represent the forest dislocations and the light colored lines are the mobile dislocations. Dark lines along the X direction are screw dislocations and along the Y direction are the edge dislocations.

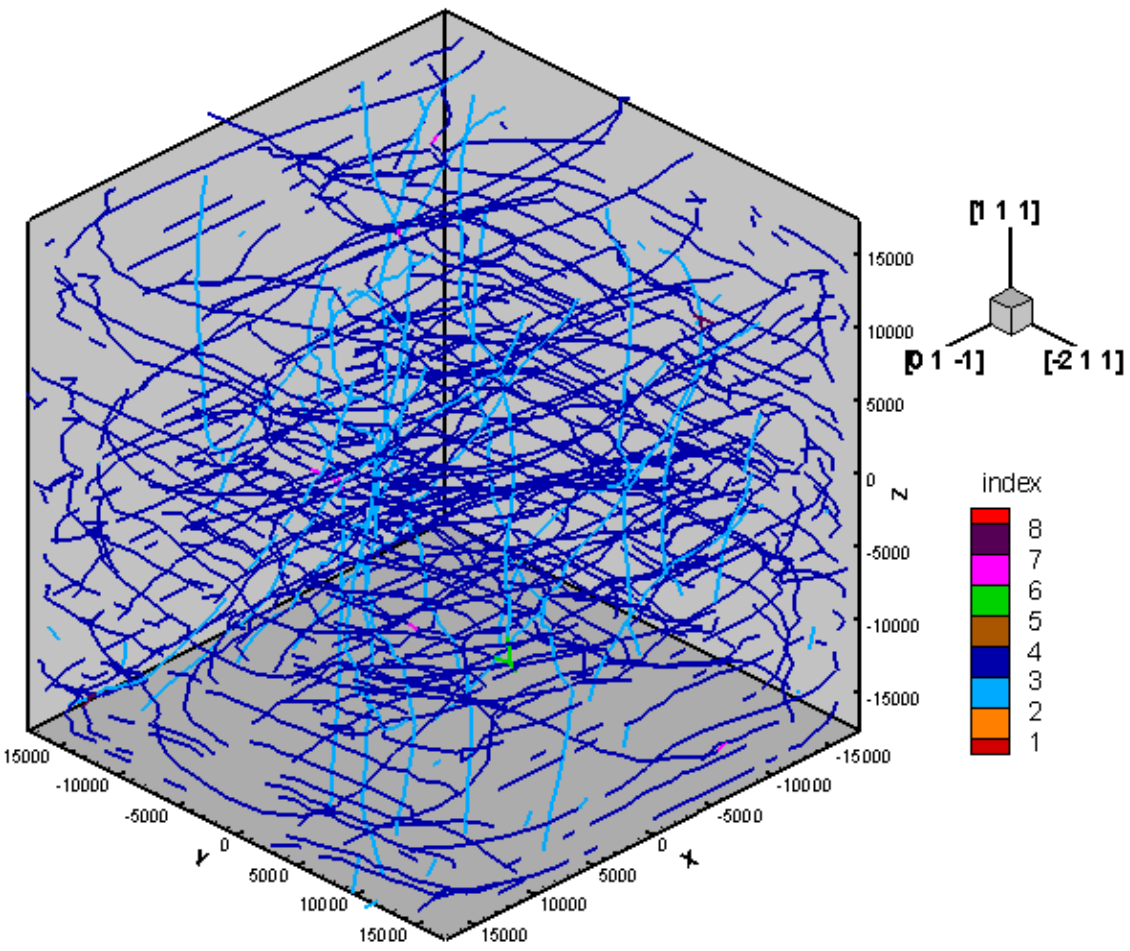

(a)

Figure 4.2 Final configuration of the simulation cells. (a) Hirth junction, (b) glissile junction, (c) Lomer junction, (d) collinear interaction. Junctions are represented by the green color. Repulsive and crossed states are represented by the pink purple colors respectively.

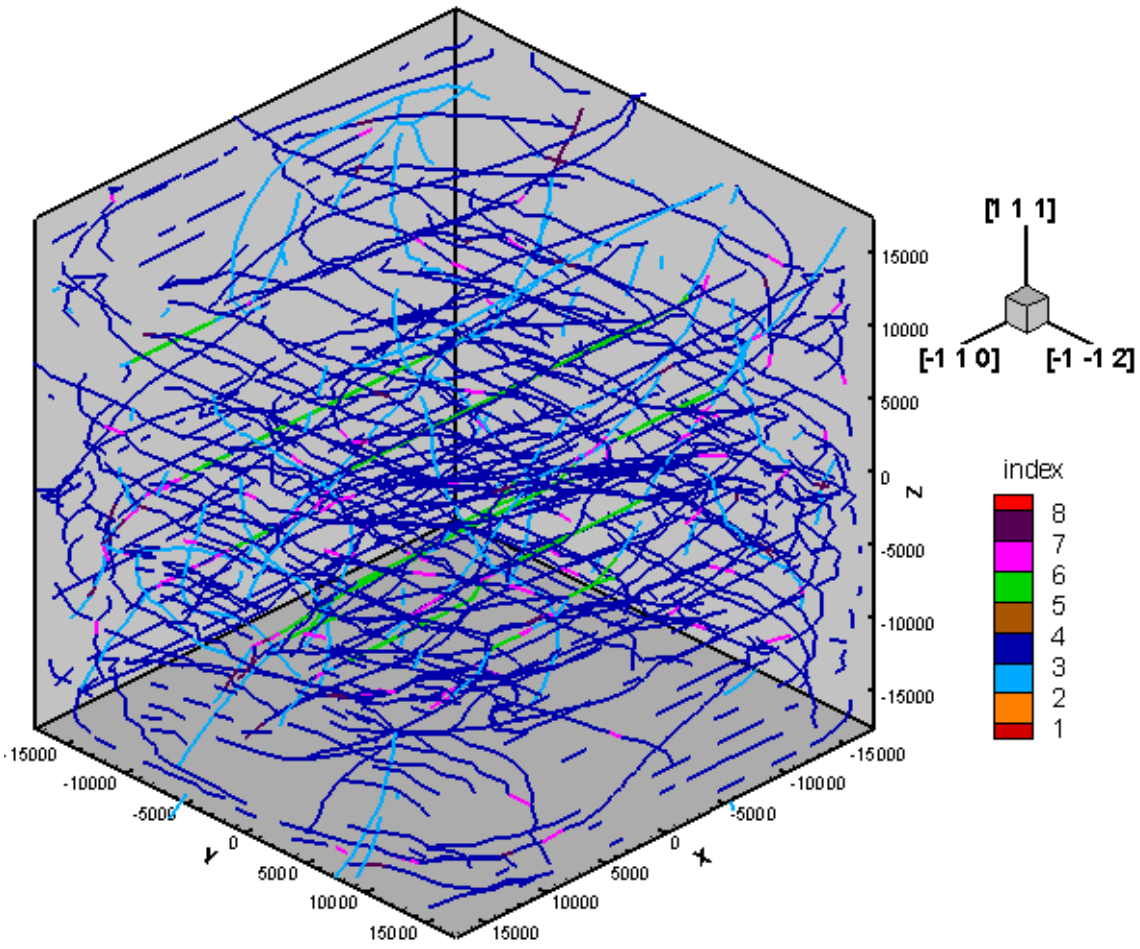
[1 1 1]
[-1 1 0]
[-1 -1 2]
index
8
7
6
5
4
3
2
1
15000
10000
5000
0
-5000
-10000
-15000
Z
Y
X

(b)

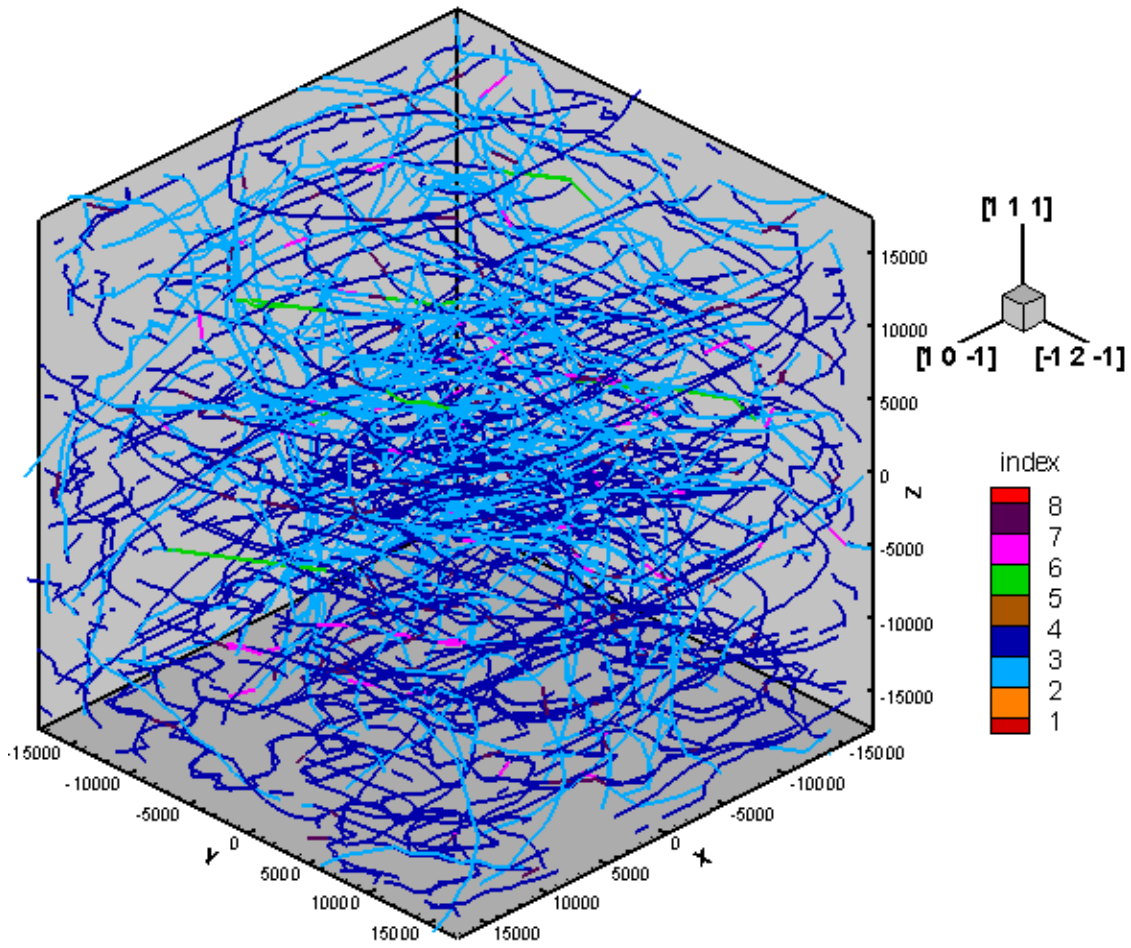
[1 1 1]
[1 0 -1]
[-1 2 -1]
index
8
7
6
5
4
3
2
1
15000
10000
5000
0
-5000
-10000
-15000
Z
Y
X

(c)

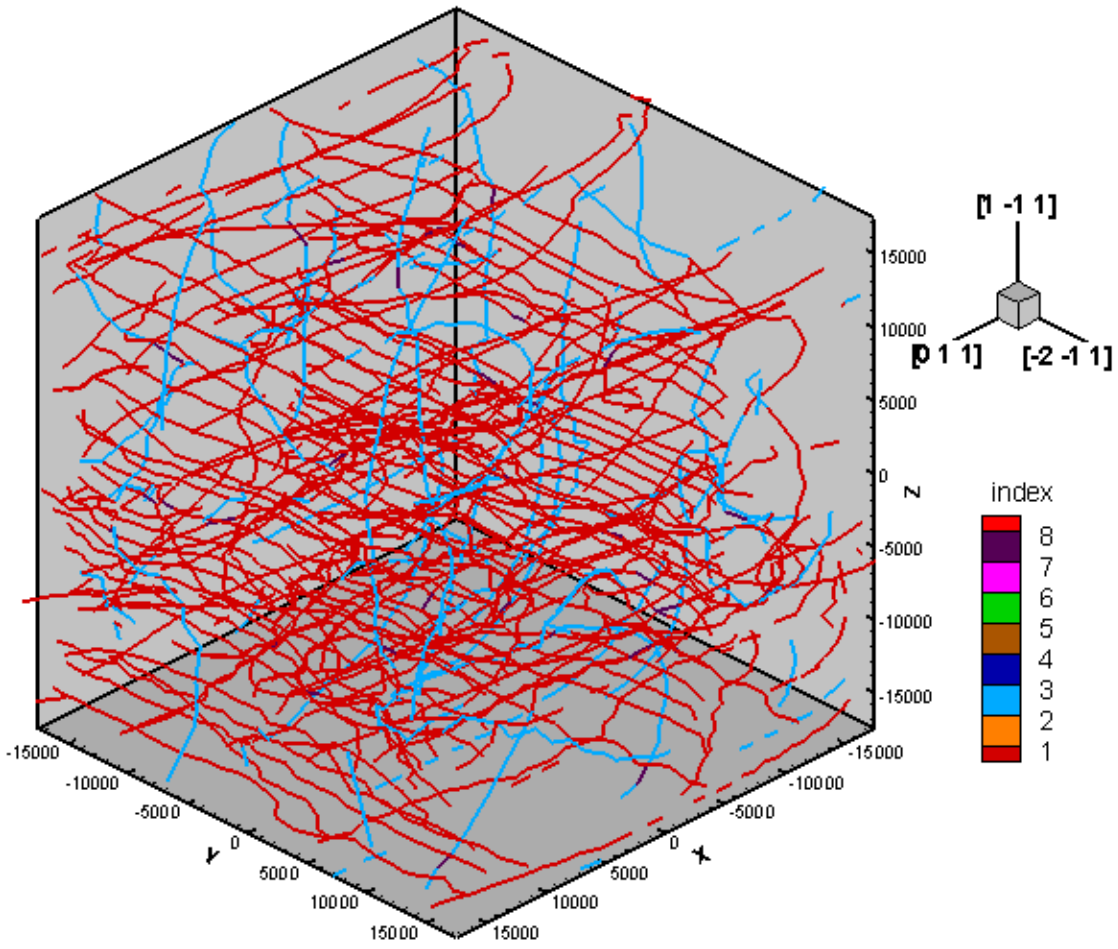

(d)

4.2 Results and discussion

Fig. 4.2 shows the final configuration for the simulation cells for glissile junction, Hirth junction and Lomer junction. In Fig 4.2, the legend identifies different planes and reactions. Number 1 to 4 represent planes $(1\bar{1}1)$, $(\bar{1}11)$, $(\bar{1}\bar{1}1)$, (111) respectively, and number 5, 6, 7, 8 represent the occurrence of a jog, junction, repulsive state, and a crossed state respectively. Junctions are potentially formed along the direction defined by the line of intersection of two non coplanar dislocation slip planes. Two same line-sense

and same Burgers vectors dislocations repel each other. Two same line-sense but opposite Burgers vector dislocations interact attractively. Attractive dislocations on the latent planes interact to form stable junctions [2]. A typical junction is shown in Fig. 4.3. The picture shows a Hirth junction which is formed between a dislocation line with Burgers vector $\mathbf{[}0\bar{1}\bar{1}\mathbf{]}$ on plane $\mathbf{(}\bar{1}\bar{1}1\mathbf{)}$ i.e. plane 3 (mobile dislocation) and a dislocation line with Burgers vector $\mathbf{[}01\bar{1}\mathbf{]}$ on plane $\mathbf{(}111\mathbf{)}$ i.e. plane 4 (forest dislocation).

Another attractive reaction which could form a junction but does not, is called a crossed state. In the crossed state the dislocations are pinned at their point of intersection but do not zip further due to higher line tension of dislocation lines than the local force required for zipping [3]. Fig. 4.4 shows the final state of dislocations showing the formation of locks. The first 3 junctions can be seen physically in the pictures and are represented by dark black lines which are encircled for clarity. The fourth interaction forms a collinear lock which can not be seen physically because it is created by pinning of dislocations which annihilate at the line of intersection of two cross-slip planes. The lock, so formed, is a result of a zero Burgers vector junction and can not be seen physically. However, the dislocation segments having one part on the forest slip system and the other on the mobile slip system can be seen [Fig 4.4(d)]. A 3D view of the formation of the collinear lock can be seen in Fig. 4.5 (a), (b), and (c) in serial with increasing time. One dislocation on plane $\mathbf{(}1\bar{1}1\mathbf{)}$ with Burgers vector $\mathbf{[}10\bar{1}\mathbf{]}$ and the other on plane $\mathbf{(}111\mathbf{)}$ with the same Burgers vector i.e. $\mathbf{[}10\bar{1}\mathbf{]}$ interact to cause a collinear annihilation. Since the reaction product is a Burgers vector of “zero” length, it is the minimum energy configuration of the reacting dislocations and therefore makes it harder to destabilize the pinning. Note that no quantitative analysis is done on repulsive states

and crossed states in this work. Pictures shown in Fig. 4.4 are the view of 1 μm thin sections cut in the forest plane from the simulation cell. In Fig 4.4, junctions are in the [110] direction for glissile junctions and Lomer junctions. Hirth junction are in the [100] direction. Mobile segments which are shown in gray color are, in general bigger in the Hirth, glissile, and Lomer junction simulations as compared to the collinear interaction simulations. This is attributed to the collinear annihilation in the latter which causes the mobile segments to break into smaller segments. Forest segments break into smaller segments as well, but to a lesser extent. These segments need higher stress for remobilization than before the reaction. This can be visualized in Fig. 4.6 which shows the evolution of RSS as a function of plastic strain. RSS curves for the three junctions are rather smoother as compared to those for the collinear reactions. Frequent jumps in the RSS in the plot for the collinear reaction are attributed to the elastic relaxation after each collinear annihilation.

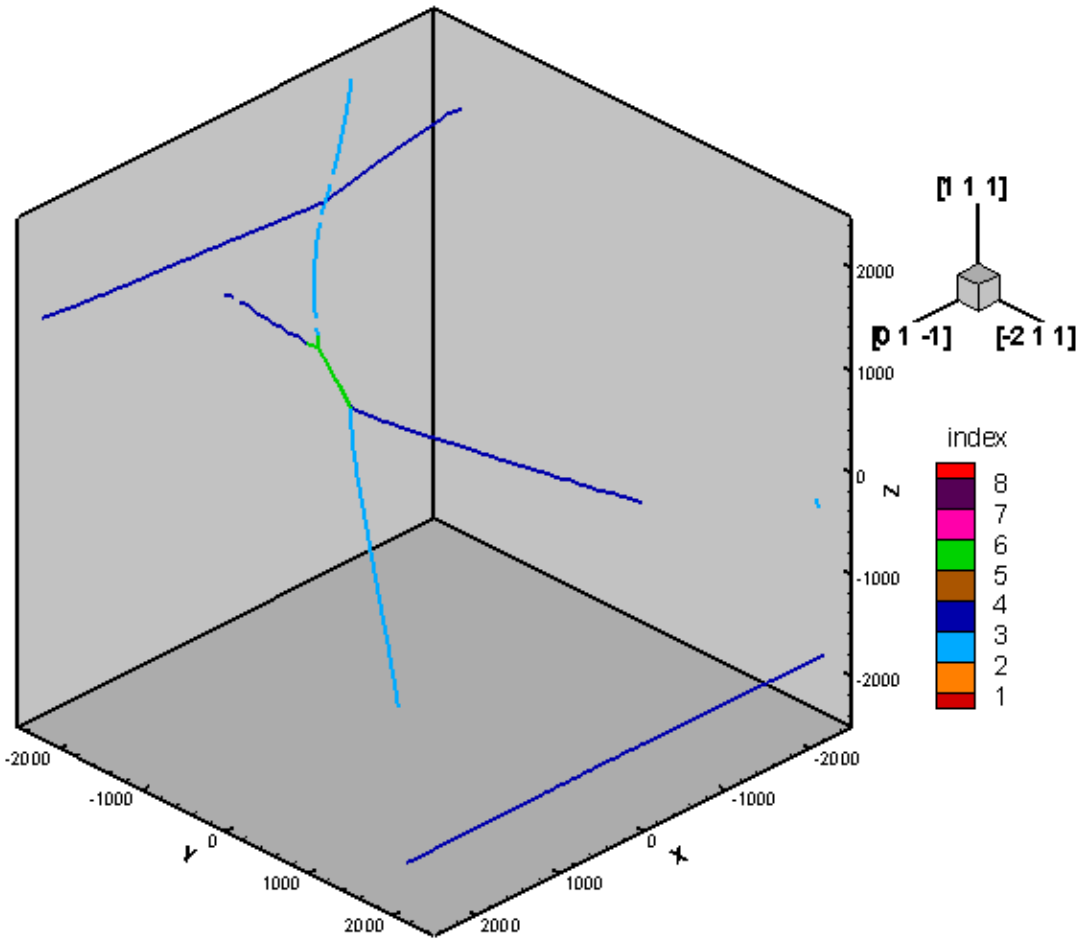

Figure 4.3 A smaller simulation cell showing a typical junction. The green color line shows a junction of Hirth type.

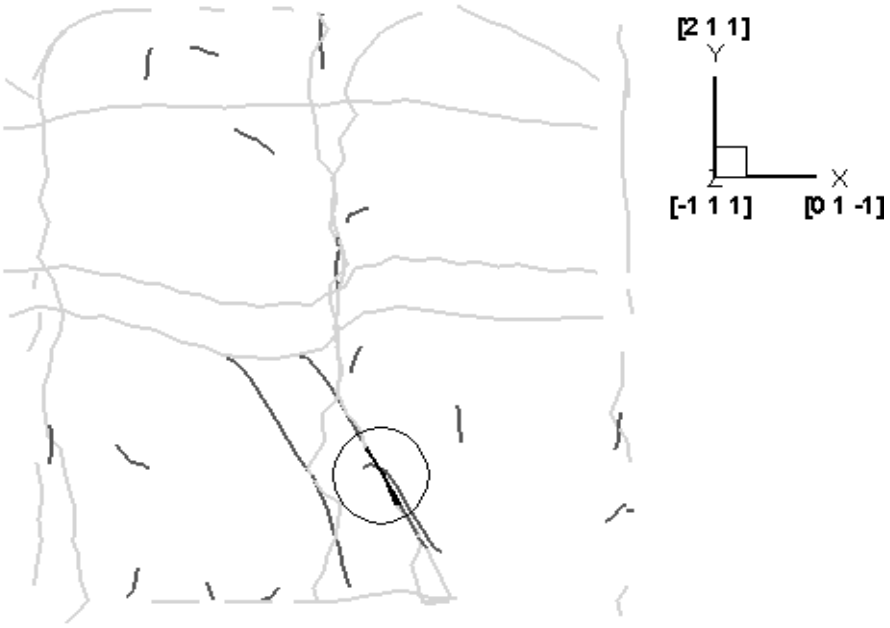

(a)

Figure 4.4 Views of DD simulations, showing formation of (a) Hirth junctions, (b) Glissile junctions, (c) Lomer junctions, and (d) Collinear interactions. Light gray (horizontal) lines are forest screw dislocations while the forest edge dislocations are perpendicular to the plane of the paper. Dark gray lines are mobile dislocations. Black, encircled lines are junctions.

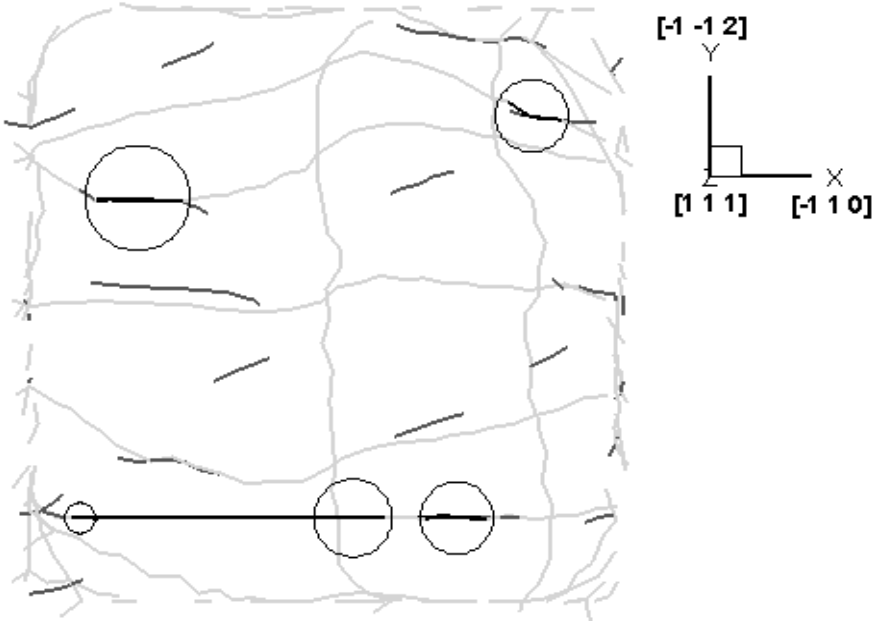

(b)

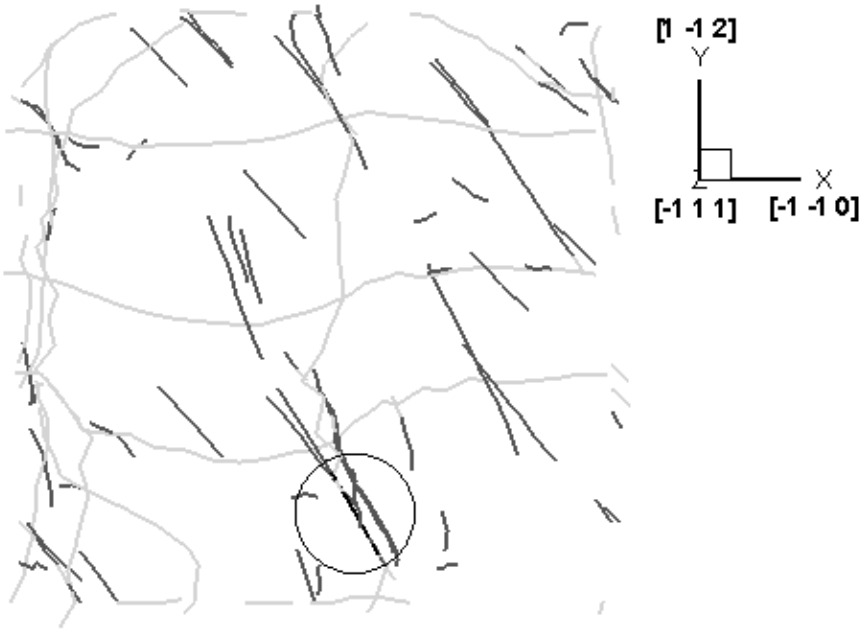

(c)

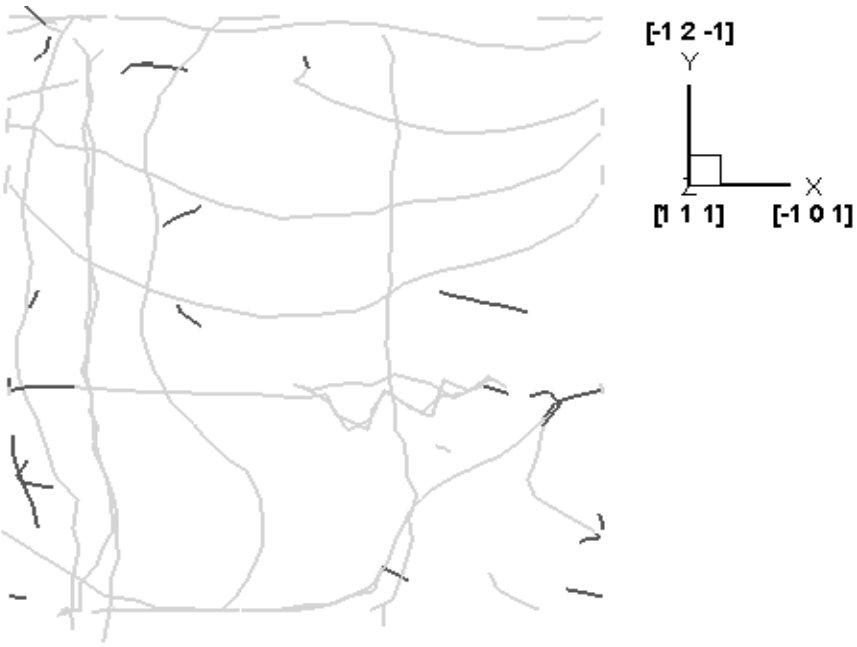

(d)

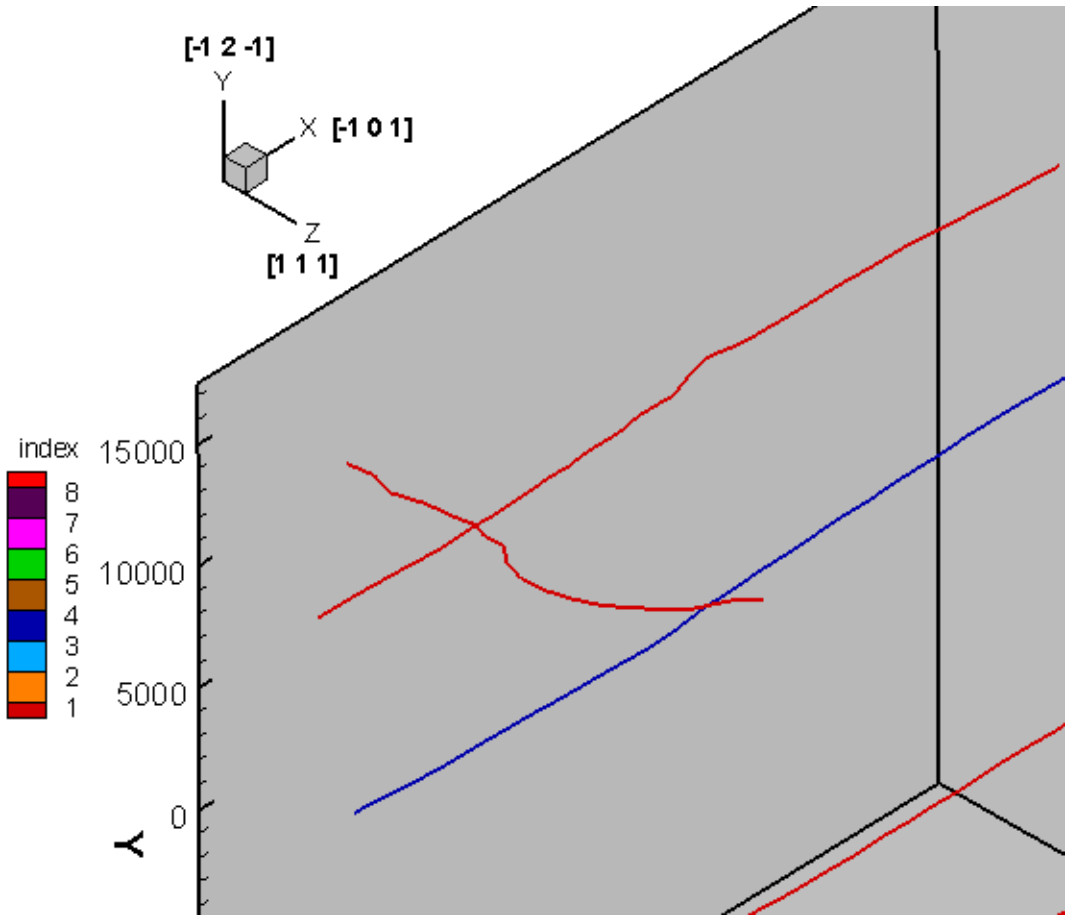

(a)

Figure 4.5 Formation of a collinear lock. (a), (b) and (c) are in serial with increasing time.

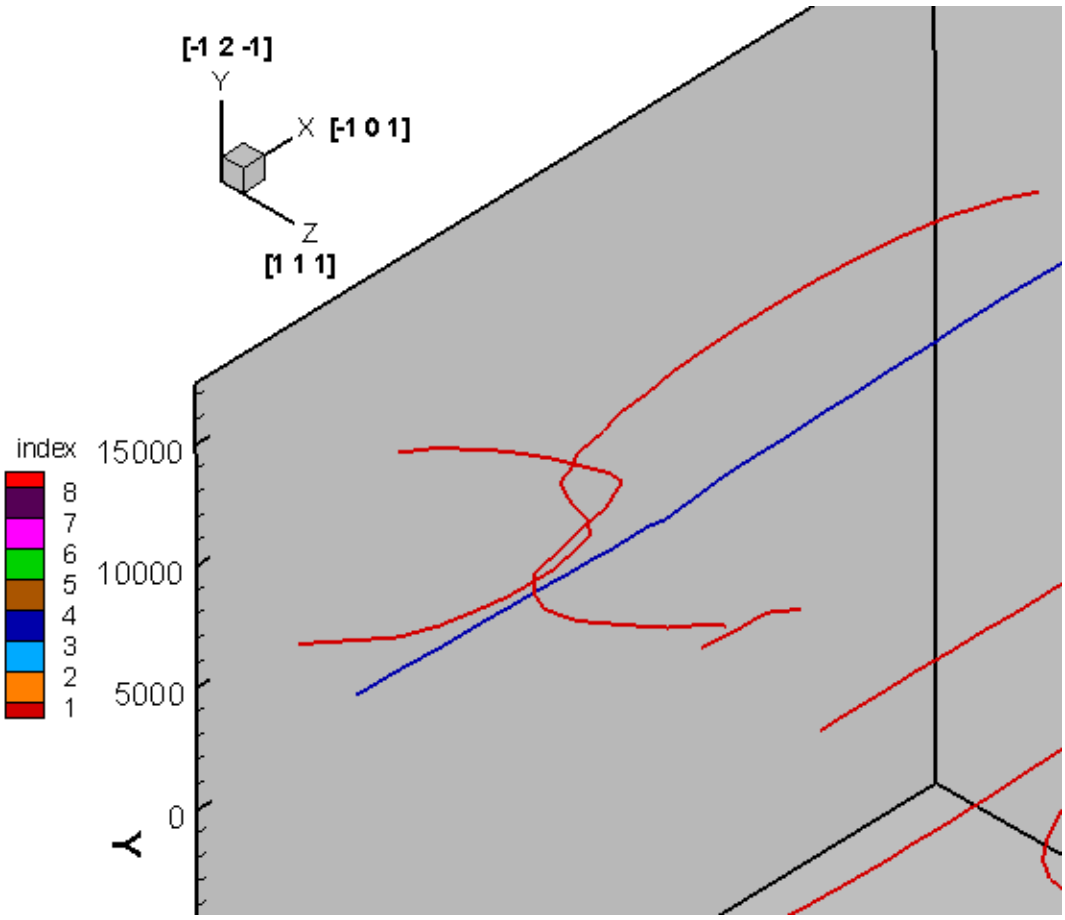

(b)

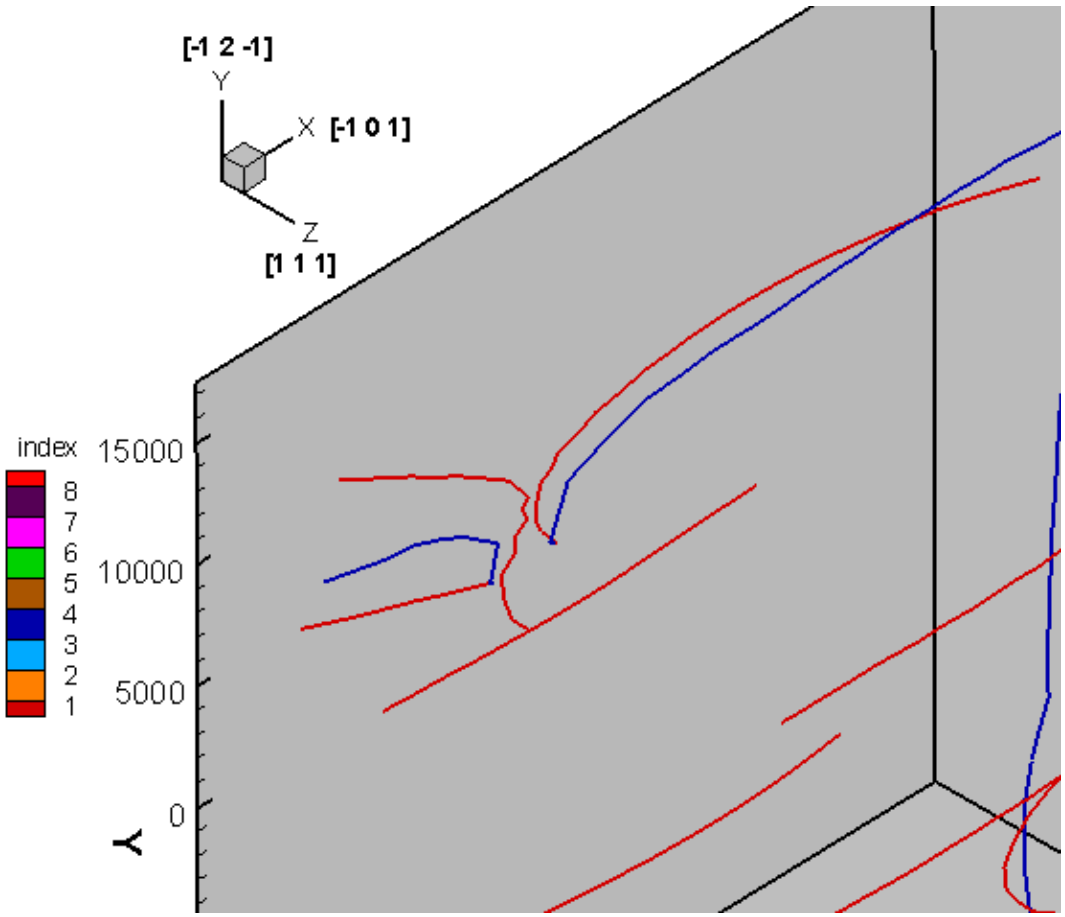

(c)

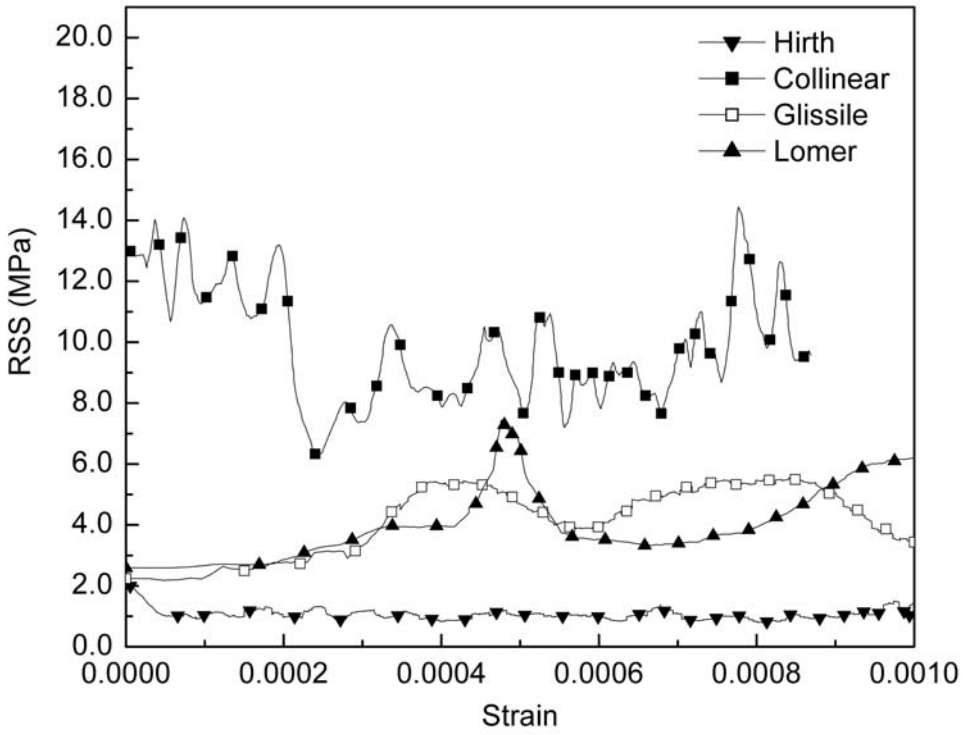

Figure 4.6 Evolution of resolved shear stress with respect to plastic strain for Hirth junctions, glissile junctions, Lomer junctions, and collinear interaction.

Junction formation on a segment is a highly stimulating event for further junction formation on the same segment. Once a junction is formed, the mobile and forest segments are zipped to a small fraction of their length. This causes the unzipped length of the segments to curve around the ends of the zipped (junctions) lengths and makes the segments more probabilistic for forming a junction (more junction length). An example of strength evolution with increasing number of junctions and how the junction forming segments cause more lengths to form a junction is shown in Fig. 4.7. Note that in these plots the total strains are not necessarily ~ 0.001.

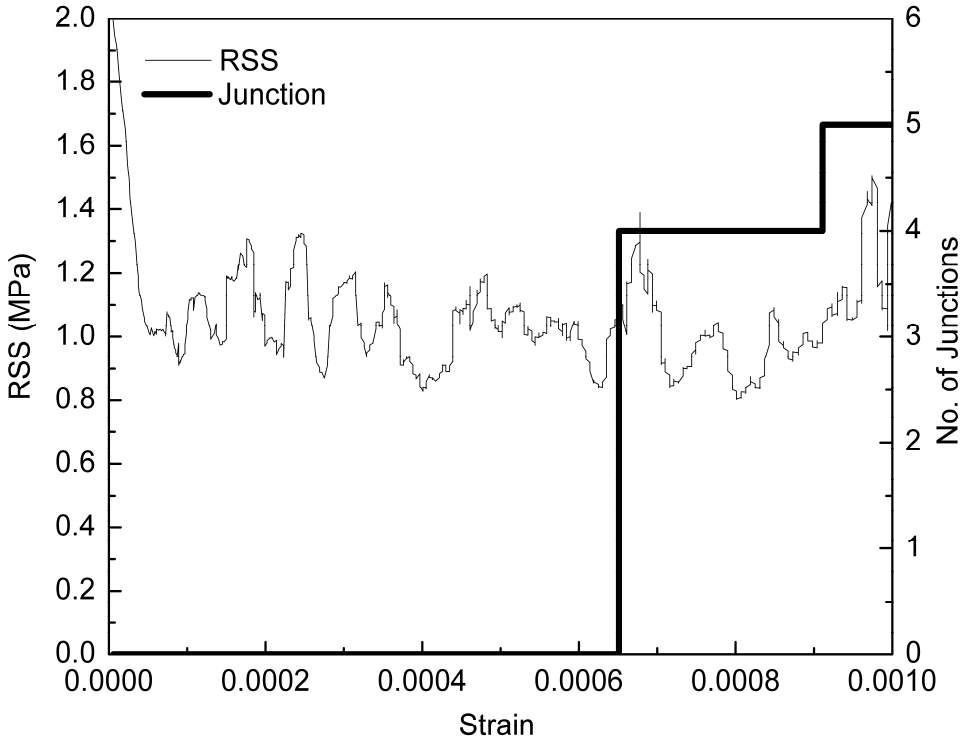

(a)

Figure 4.7 Number of junctions formed for (a) Hirth (b) glissile, (c) Lomer junctions, plotted with RSS. The thick black line in each picture represents the number of junctions. In (c) the thinner dark line shows the number of jogs.

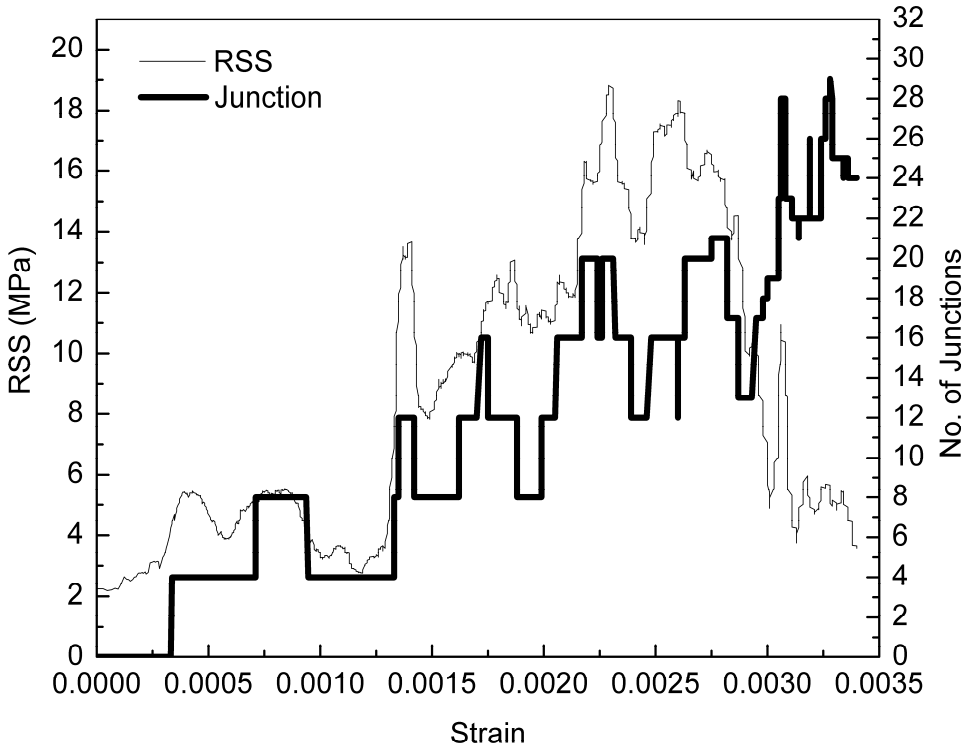
RSS
Junction
RSS (MPa)
No. of Junctions
Strain
0
2
4
6
8
10
12
14
16
18
20
22
24
26
28
30
32
0.0000
0.0005
0.0010
0.0015
0.0020
0.0025
0.0030
0.0035

(b)

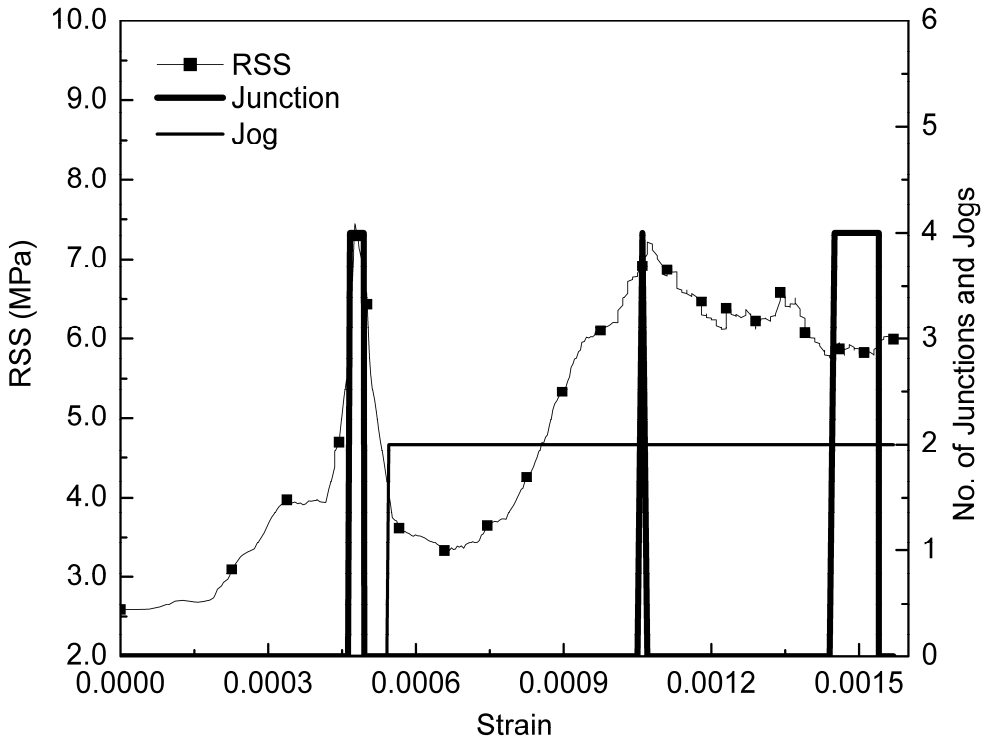

(c)

For a more reasonable comparison of junction strength, not only stress values, but the number of junctions formed at different strain levels should be studied. We compare the number of junctions as functions of strains and correlate the stress evolution with corresponding junctions. Glissile junctions are formed most easily followed by Hirth and Lomer junctions. Glissile junctions are formed at a high frequency as a function of strain but the critical resolved shear stress at which they are formed is not higher than that for the Lomer junctions. Lomer junctions are similar to glissile junctions except the fact that they are sessile, therefore they cause high stress evolution once formed. Fig. 4.7(c) shows the number of jogs which were observed in the simulation for Lomer junctions. It is evident that junction formation has a much stronger effect on the strength evolution as compared with jog formation. This could be justified with the argument that in jog

formation, much smaller fractions of the interacting segments come together as compared to a junction formation. Also, in junction formation the angles between the interacting segments are smaller (< 8^o in the present simulation studies) as compared to those in jog formations. The smaller angle of interaction causes zipping of the segments, which is evidently a much stronger reaction than a jog. The coefficients of hardening are determined using Eq (4.1). For determination of the critical RSS in each reaction, the RSS value at which the first reaction occurs is used. Forest dislocation density is used for the corresponding RSS value. Table 2 shows the hardening coefficients determined using these simulations.

Table 4.2 Hardening coefficients for different junctions

Junction/Lock Type	Interaction coefficient		
	Current work* Avg (Min, Max)	Devincre et al. [1]	Madec et al. [4]
Hirth	0.0312 (0.0154, 0.0615)	0.0454+/-0.003	0.051+/-0.012
Glissile	0.2128 (0.1631, 0.2504)	0.137+/-0.014	0.075+/-0.014
Lomer	0.2225 (0.1443, 0.2895)	0.122+/-0.012	0.084+/-0.012
Collinear	0.9968 (0.9347, 1.0489)	0.625+/-0.044	1.265+/-0.125

*Values are calculated using 4 simulations for each reaction

The hardening values obtained are of the same order as reported in the literature [4] and are justified according to the reasoning given earlier and in the literature e.g. [1, 4]. However, in reference [1], the hardening coefficient for a glissile junction is reported

to be higher than that of a Lomer junction which contradicts the fact that the latter is a sessile junction.

The other hardening coefficients used in the CPFEM model are the average dislocation segment length coefficients described referring to Eq. (3.14) in Chapter Three. Determination of these coefficients even using a simplified relation similar to Eq. (4.1) will not be straight forward. The average segment length of a mobile dislocation is an average length pinned between two immobile points in that dislocation length [5]. This immobile point can be a junction with the forest dislocation (in the case of a pure crystal) or a solute atom or precipitate in a more complex case. The determination of all segments of mobile dislocations (length between junctions with forest dislocations) is not performed for this research and can be considered for future work using the above vision.

4.3 Summary

Strength of junctions in aluminum is studied using discrete dislocation dynamics of curved dislocations of mixed character. This simulation is based on aluminum which is elastically more isotropic than many other metals. As described by Devincre et al. [1], these hardening coefficients are dimensionless parameters therefore they should be the same for different materials having the same crystal structure. RSS plotted along with the number of junctions formed shows that with every new junction formed, RSS evolves further and with each unzipping of a junction, the stress decreases. Calculations of hardening coefficients shown here are in order with the ones presented in similar studies in the literature. Worth mentioning is the fact that some simulation dependent criteria (e.g.

critical angles of the reacting segments, and the minimum length between two reacting segments) play significant roles on the reactions.

References

[1] Devincre B, Kubin L, Hoc T. Scripta Materialia 2006;54:741.

[2] Zbib H, Rhee M, Hirth J. International Journal of Mechanical Sciences 1998;40:113.

[3] Madec R, Devincre B, Kubin LP. Computational Materials Science 2002;23:219.

[4] Madec R, Devincre B, Kubin L, Hoc T, Rodney D. Science 2003;301:1879.

[5] Zbib HM. Personal communication on: Proportionality coefficient between average mobile dislocation segment length and forest dislocation density. 2009.

CHAPTER FIVE

ANISOTROPY OF ALUMINUM SINGLE CRYSTALS, CRYSTALLOGRAPHIC TEXTURE AND MICROSTRUCTURE EVOLUTION IN POLYCRYSTALS

The dislocation density evolution framework described in Chapter 3 is integrated into the user subroutine interface UMAT in ABAQUS^{TM}/Standard using a fully-implicit time integration procedure. In this chapter, applications of the model are discussed in the order of increasing complexity of microstructure evolution. Predictions by the model for stress-strain evolution and orientation evolution for uniaxial tensile tests of single crystals are compared against the experimental results reported in the literature. Crystallographic texture and microstructure evolution is discussed referring to dislocation density, hardening and orientation evolution in polycrystals.

5.1 Anisotropy of single crystals

For calibration of the CPFEM model, experimental results for single crystal tensile stress-strain behavior for aluminum by Hosford et al. [1] were used. For single crystals, the FE formulations use a simplified geometry of 0.04 mm x 0.04 mm x 0.04 mm, consisting of 1 element. C3D8 type elements are used. This element is an 8 node, 8 integration points linear brick element in ABAQUS/Standard element library [2]. The rear face perpendicular to Z is restricted for displacement in Z and the front face perpendicular to Z is pulled in the Z direction. Strain is caused using a prescribed displacement. Material constants and fitting parameters used in the current model are shown in Table 5.1.

Table 5.1 Material parameters for single crystal aluminum

Elastic moduli	C_{11} =108 GPa
	C_{12} =61.3 GPa
	C_{44} =28.5 GPa
	μ =25.0 GPa
Burgers vector	$\|b\|$ =2.863 Å
Critical radii	R_e =10.0 nm, R_s =90.0 nm
v_o	1.0e-3 m.s^{-1}
p, q	0.10, 1.41 respectively

Table 5.2. Euler angles used for single crystals

Single crystal Identification	Single crystal	φ_1 (^{o})	Φ (^{o})	φ_2 (^{o})
A	[-1 2 3]	75.0	36.0	333.0
B	[-1 2 5]	47.0	24.0	333.0
C	[-4 2 1]	94.0	77.0	296.0
D	[-2 3 6]	70.0	31.0	326.0
E	[111]	0.0	54.7	45.0
F	[111]*	0.0	54.7356	45.0
G	[-110]	360.0	90.0	315.0
H	[100]	90.0	90.0	90.0

*With negligible misorientation from the tensile axis.

The Euler's angles used for simulations of all the single crystals in this work are shown in Table 5.2. The stress-strain evolution in aluminum single crystals <111> and <100> is presented in Fig. 5.1. The CPFEM model captures the stress evolution fairly closely along with the characteristic difference in hardening in <111> and <100> single crystals. The <111> single crystal shows a relatively faster rate of hardening as compared to the <100> , even though there are fewer slip systems active as compared to the latter. Slip systems A5, A3, D5, D1, C3, and C1 are active in tensile tests of <111> single crystals, while in <100> single crystals slip systems B6, B4, A5, A3, D5, D4, C6, and C3 are active. A misorientation of less than 1^{o} was given to the <111> single crystal, while the <100> single crystal was perfectly oriented along the tensile axis. This can be seen clearly in Fig. 5.2 which shows evolution of the resolved shear stress (RSS) in the two single crystals. The <111> single crystal shows distinguished evolution of the RSS in all active slip systems. See Fig. 5.2(a). However in the <100> single crystal, RSS evolves identically on all of the active slip systems. See Fig. 5.2(b).

The difference in hardening rate in the two types of single crystals can be seen through the evolution of dislocation densities as well, which is shown in Fig. 5.3. Therein, the evolution of total edge and total screw type dislocation densities in the single crystals is depicted, and the higher stress level in <111> single crystals as compared to <100> is justified. Also, the difference in evolution of edge and screw dislocation densities can be easily appreciated.

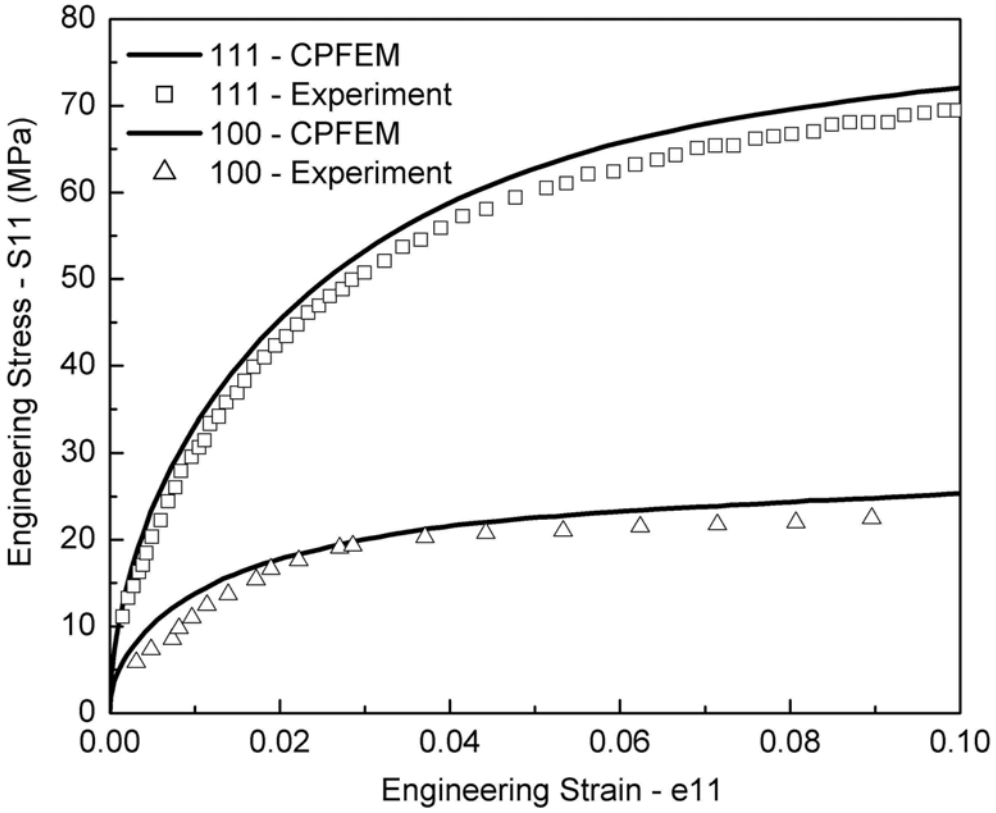

Figure 5.1. Stress evolution as a function of strain in single crystal aluminum <111> and <100> validated against experimental data obtained from the work of Hosford et al. [1]

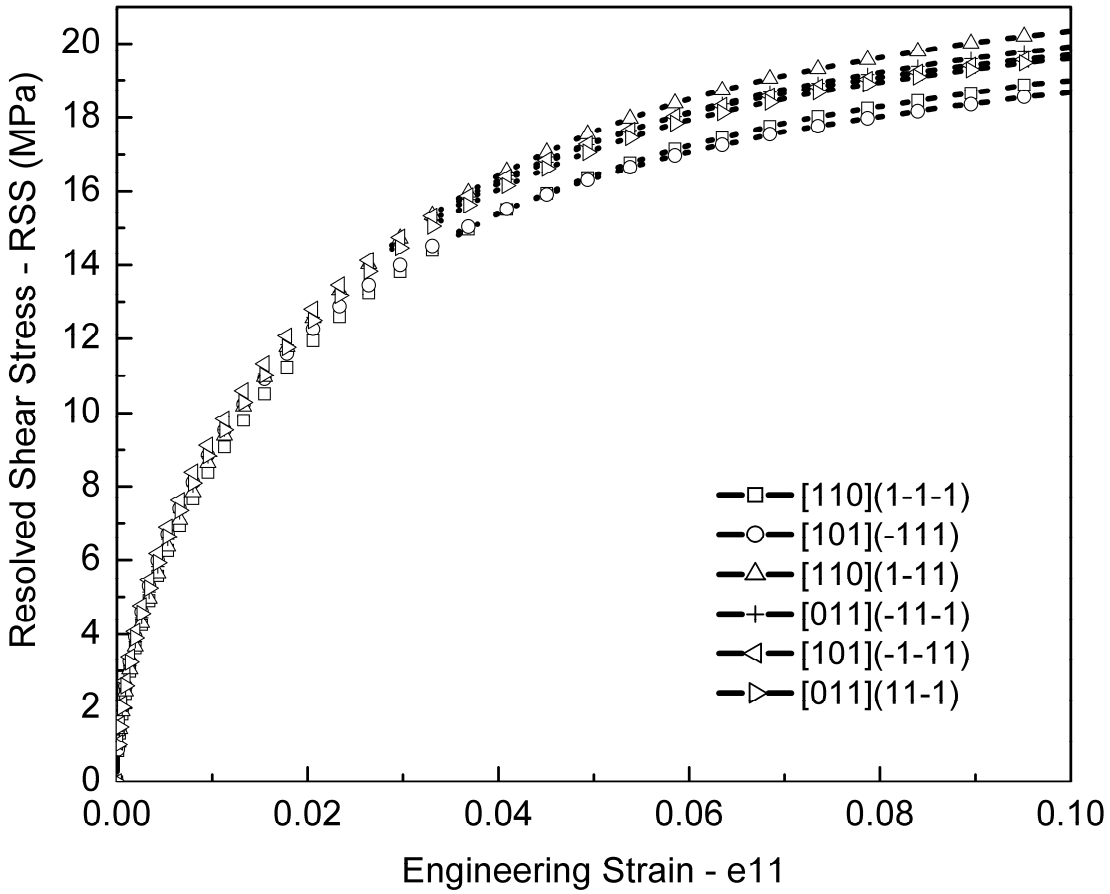

(a)

Figure 5.2. Resolved shear stress evolution in aluminum single crystals (a) <111> (misorientation <1^{o}) and (b) <100> (no misorientation included).

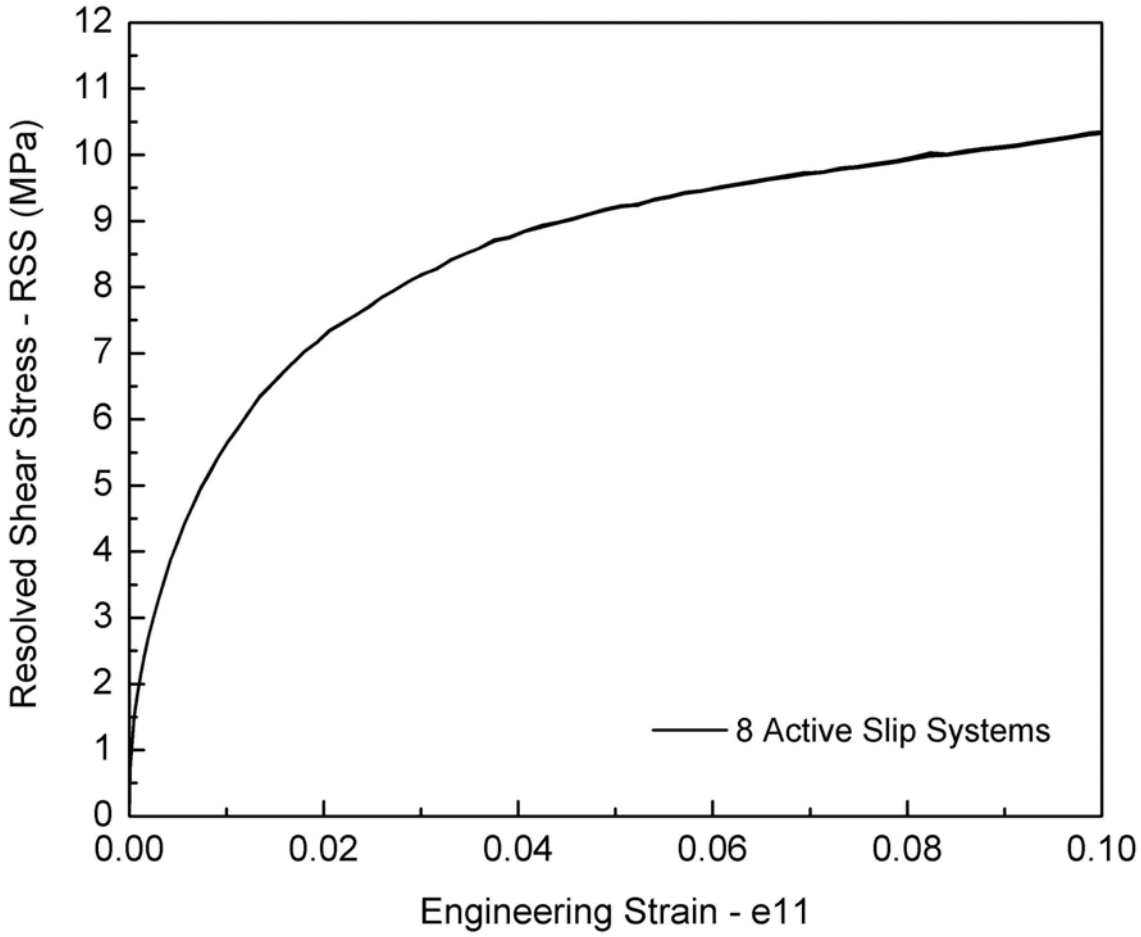
Resolved Shear Stress - RSS (MPa)
Engineering Strain - e11
8 Active Slip Systems
0
1
2
3
4
5
6
7
8
9
10
11
12
0.00
0.02
0.04
0.06
0.08
0.10

(b)

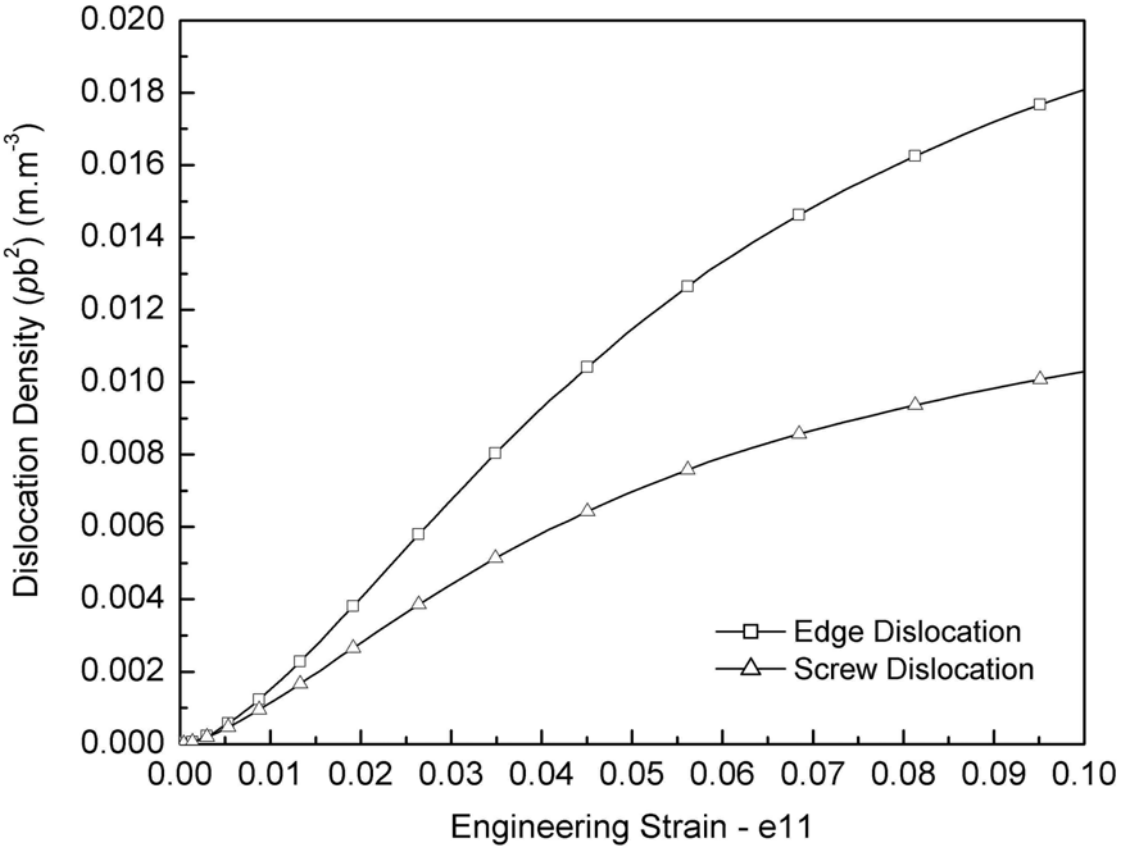

(a)

Figure 5.3. Dislocation density evolution in pure aluminum single crystals (a) <111> and (b) <100>

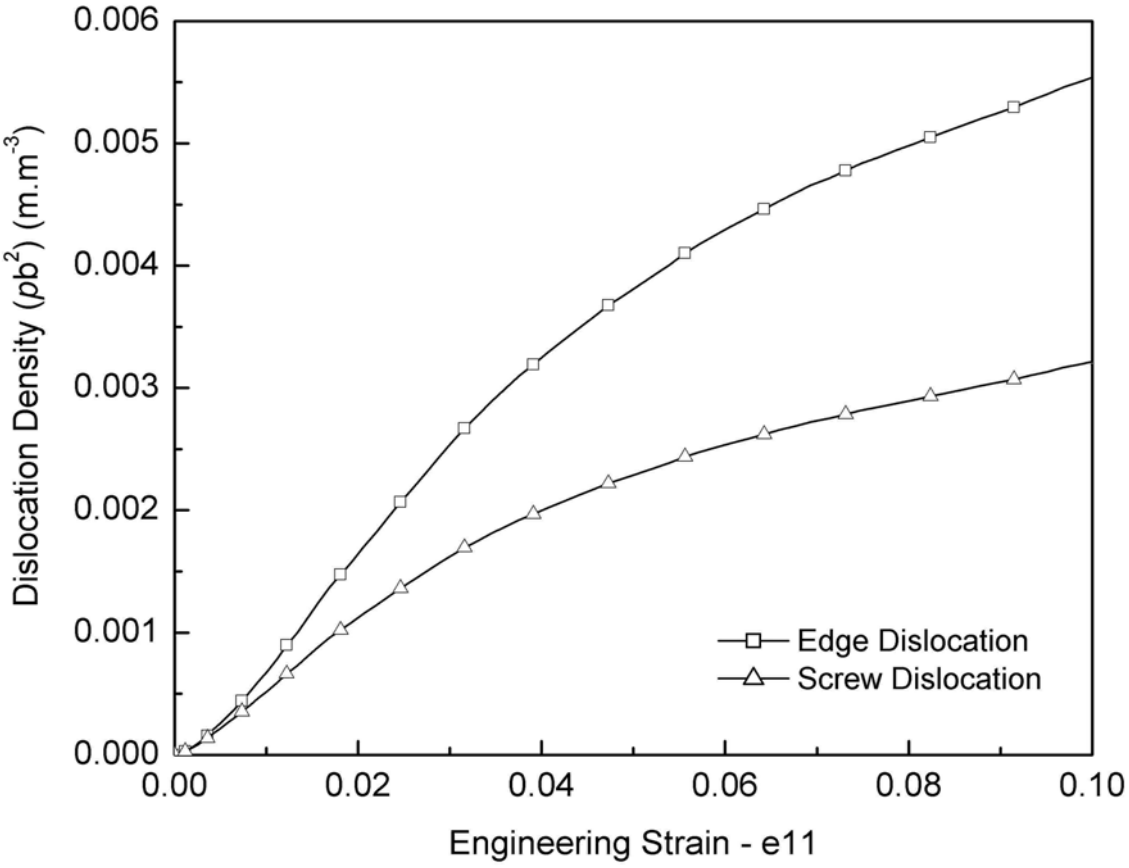
0.006
0.005
0.004
0.003
0.002
0.001
0.000
Dislocation Density (ρb^2) ($m.m^{-3}$)
0.00
0.02
0.04
0.06
0.08
0.10
Engineering Strain - e11
Edge Dislocation
Screw Dislocation

(b)

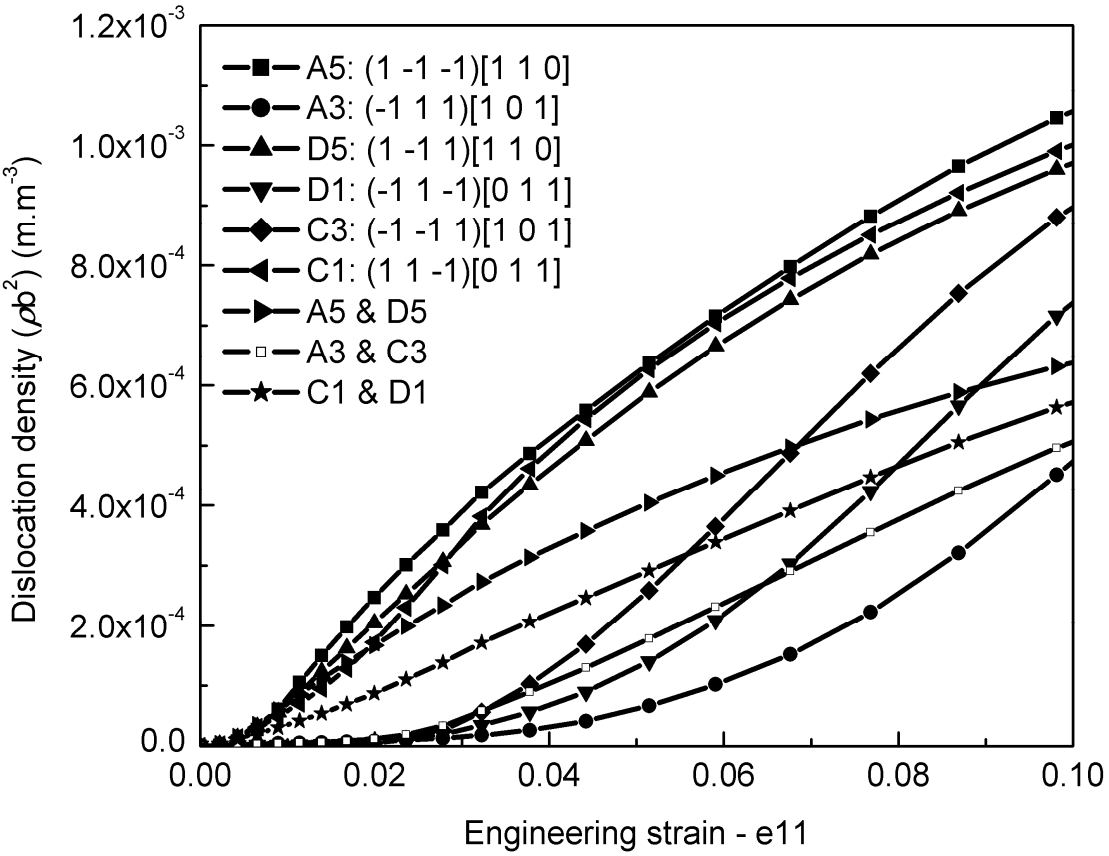

Figure 5.4. Dislocation density evolution on different slip systems of aluminum single crystal <111> with little misorientation (< 1 degree)

Figure 5.4 shows the evolution of dislocation densities for the uniaxial tensile text mentioned earlier. In this picture also, the effect of misorientation of the tensile axis from the <111> direction can be seen. The edge type dislocations on slip systems A5, C1, and D5 show a higher degree of evolution as compared to the other three edge type dislocations i.e. on C3, D1, and A3. The screw dislocations show intermediate evolution rates between these two sets of edge type dislocations. The sets of edge dislocations and

screw dislocations are diverging after the simulation starts but soon after they seem to converge in the groups of edge and screw type dislocations.

5.1.1. Overshooting in single crystal aluminum

Application of overshooting phenomenon in single crystals for study of hardening laws was discussed briefly in Chapter 2. The reader is referred to the experimental study by Joshi and Green [3] for a discussion of the occurrence of overshooting in aluminum. On the contrary, a theoretical approach (Taylor and Elam [4]) shows that during uniaxial tensile deformation of an aluminum single crystal oriented in single glide orientation, the tensile axis would reach the symmetry line and then would start moving along it, showing double glide behavior. Here, the current CPFEM model is shown to predict the overshooting behavior. In this section, the effect of latent hardening parameters on the overshooting behavior is discussed emphasizing the role of the collinear interaction (cross-slip) of dislocations. The correlations of average segment length and slip resistance are given by average dislocation segment length parameters and hardening parameters respectively. Since both govern the evolution of hardening, we call both of them hardening parameters.

For studying the phenomenon of overshooting, simulations of uniaxial tensile test are performed on different orientations of single crystals. Simulation set up is identical to as described earlier in Section 5.1. A hardening parameter for collinear interaction less than that of the Lomer junction, shows overshooting by our CPFEM model. If the hardening parameter for collinear interaction is chosen to be higher as compared to the other hardening parameters, the extent of overshooting is increased. Henceforth the

hardening parameters are treated in two sets; namely, set 1: In which the Lomer junction parameter is the strongest hardening parameter, set 2: In which the collinear lock parameter is the strongest hardening parameter. The results from these two sets of parameters are compared to show the effect of hardening parameters on the evolution of the tensile axis orientation. In the forthcoming section are presented the simulation setup, results, discussion, and conclusions. The hardening parameters of set 1 and set 2 are shown in Table 5.3 and Table 5.4 respectively.

Table 5.3 Dislocation strength interaction parameters

Parameters	G_0 Parallel burgers vector on same planes	G_1 Parallel burgers vectors on parallel planes	G_2 Collinear lock	G_3 Glissile junction	G_4 Hirth junction	G_5 Lomer junction
Set 1	0.10	0.22	0.30	0.38	0.16	0.45
Set 2	0.10	1.00	0.30	0.38	0.16	0.45

Table 5.4 Average dislocation segment length interaction parameters

Parameters	H_0 Parallel burgers vector on same planes	H_1 Parallel burgers vectors on parallel planes	H_2 Collinear lock	H_3 Glissile junction	H_4 Hirth junction	H_5 Lomer junction
Set 1	0.0	0.0	0.05	0.12	0.03	0.25
Set 2	0.0	0.0	1.0	0.12	0.03	0.25

The phenomenon of overshooting depends on latent hardening. Tabourot et al. [5] have shown the occurrence of stage I, stage II, and stage III hardening in pure copper using a dislocation density based model which is specifically designed to model single glide behavior. However, in their work, the evolution of orientation for a [-125] oriented single crystal, is not shown to have any overshooting to the conjugate slip system. On reaching the symmetry line for the slip systems considered, the orientation evolution starts following the direction of double slip along the symmetry line. This is in contrast to the orientation evolution shown by Anand and Kothari [6] for a copper single crystal of [-236] orientation using a rate dependent CPFEM model employing isotropic latent hardening. Basinski and Basinski et al. [7] report that the latent hardening ratio of all coplanar systems is unity (except for Cu - Philip [8]) which means that the ratio of stress on system II (orientation in which system II is activated) to the ratio of stress on system I

(orientation in which system I is activated) is one. This implies that in a non-hardening system, there should be no overshooting. This is well supported by the work of Anand and Kothari [6] who show that a CPFEM model employing non-hardening behavior does not predict overshooting. In contrast to the commonly used isotropic latent hardening, the model which we have used for the present work, uses hardening parameters based on distinct dislocation reactions and junction formation [9]. In this CPFEM model, the Lomer junction is considered to be the strongest junction. However, it has been recently reported [10] that a collinear interaction of dislocations is much stronger than a Lomer junction. Two dislocations with a common burgers vector may interact along the line of intersection of their glide planes (cross slip planes) to annihilate a part of their segment lengths. Such an interaction may be envisioned as a zero Burgers vector segment [10] (also see Chapter 2, Chapter 3).

The rotations of symmetric orientations of single crystals are shown in the standard stereographic unit triangles in Fig. 5.5. A [111] orientation with negligible misorientation (orientation 'F' in Table 5.2) shows negligible movement of the tensile axis inside the unit triangle (see Fig. 5.5a). This is not the case with the behavior of crystal 'E' in which the crystal axis is slightly misoriented from the [111] tensile axis (See Fig. 5.5b). In this orientation there are 6 unequally active slip systems. Similar behavior is shown by another symmetrically oriented single crystal [011] and the orientations of the tensile axis can be seen coincident on the [011] pole in Fig. 5.5c.

Fig. 5.6 shows the rotation of the tensile axis for single glide oriented single crystals. The right hand column in Fig. 5.6 is for the simulations which use set 1 of the parameters (collinear lock is not the strongest hardening parameter). The left hand

column in Fig. 5.6 is for the simulations which use set 2 of the parameters (collinear lock is the strongest hardening parameter). Single crystal ‘A’ for which the tensile axis is oriented in the [-123] direction, shows a movement of the tensile axis towards the symmetry line and overshooting into the conjugate slip system. After overshooting into the conjugate slip system it turns suddenly and starts moving parallel to the symmetry line of the two slip systems. This is the case with all single crystals oriented for single glide. The farther the initial orientation of the tensile axis from the symmetry line into the primary slip system, more it travels to reach the symmetry line and beyond to overshoot. In all simulations, the single crystal was stretched up to ~ 45 % elongation.

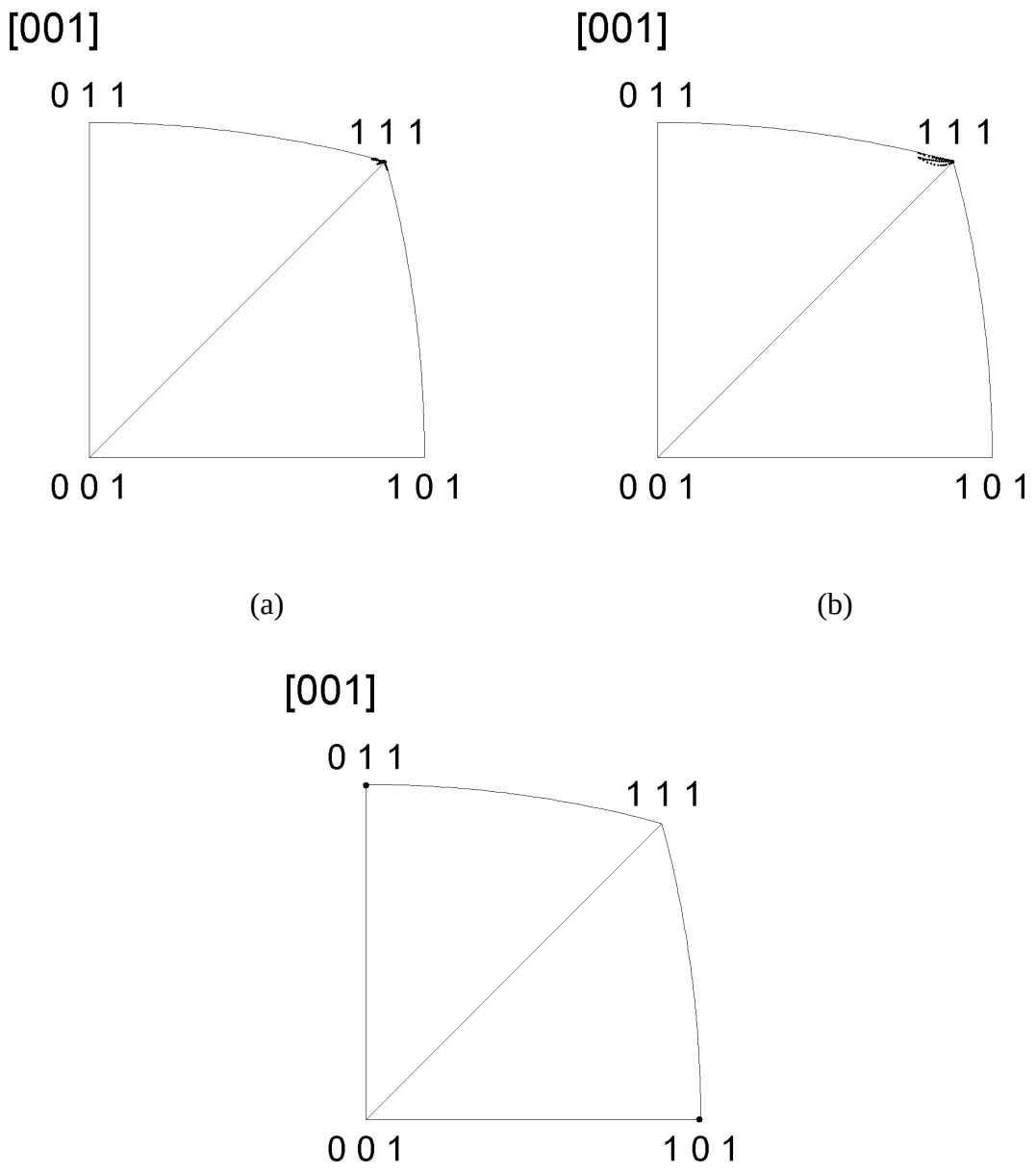

Figure 5.5. Orientation changes for tensile axes during the deformation of symmetrically oriented single crystals. (a) [111] with no misorientation, (b) [111] with misorientation, (c) [011] with no misorientation

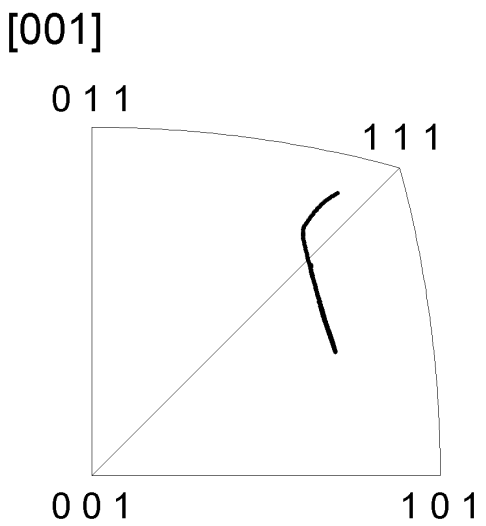

(a)

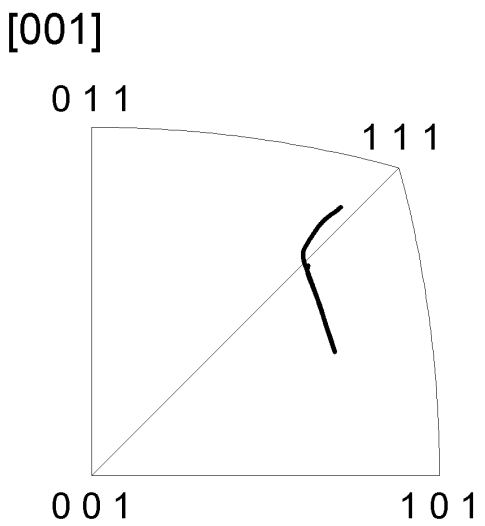

(e)

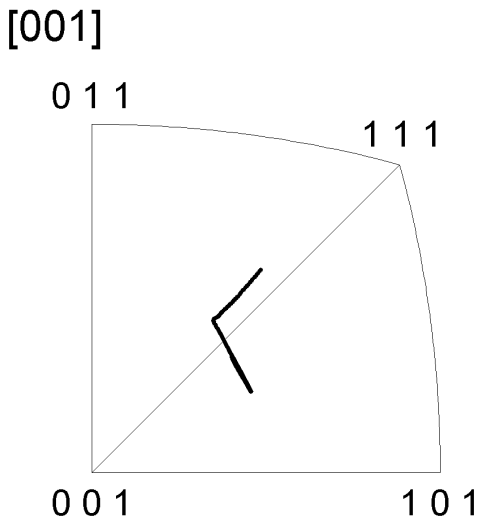

(b)

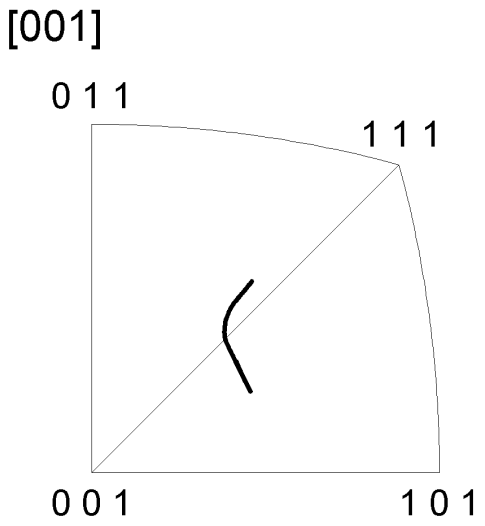

(f)

Figure 5.6. Orientation changes for tensile axes during the deformation of single glide oriented single crystals. (a) [-123] (b) [-125] (c) [-421] (d) [-236]. (e), (f), (g) and (h) show the counterparts of (a), (b), (c), and (d) respectively using hardening parameters of set 2.

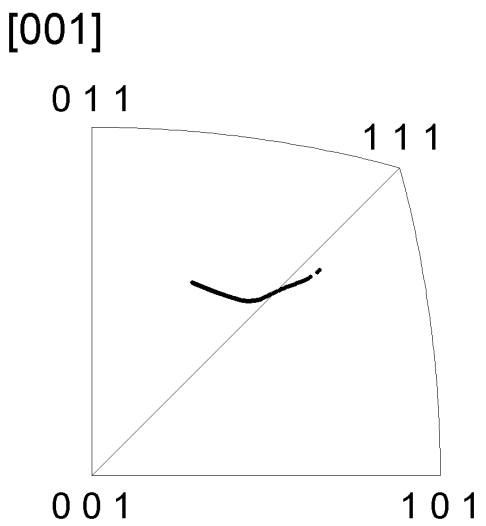

(c)

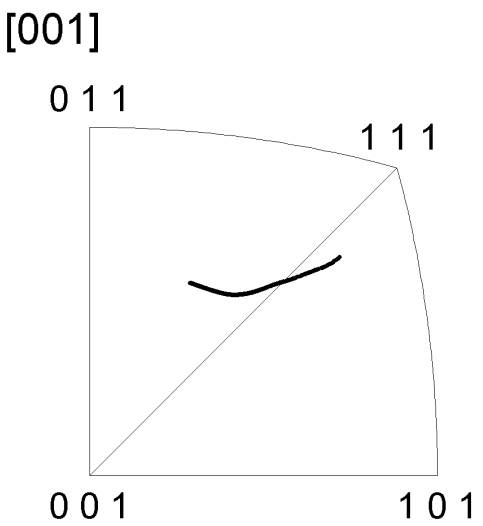

(g)

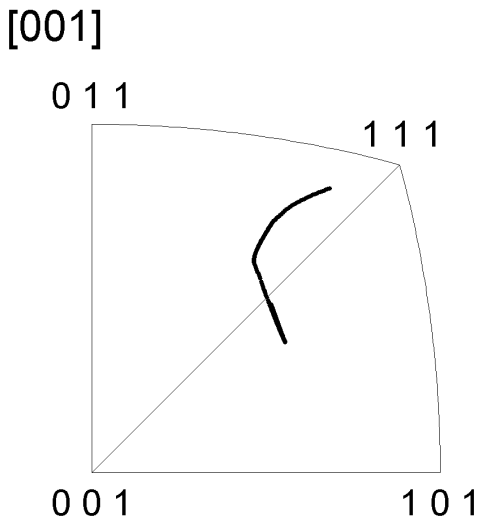

(d)

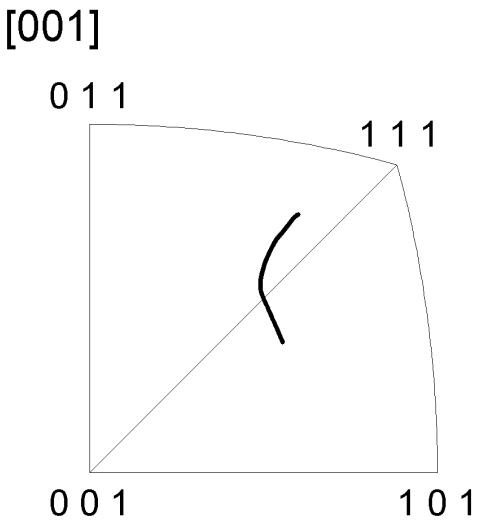

(h)

In the simulations which show overshooting, after overshooting the tensile axis orientation starts moving parallel to the symmetry line of the primary slip system and the conjugate slip system and then turn towards the [111] pole, as seen in Fig. 5.6. Single

crystal ‘C’ shows slightly different behavior as the tensile axis changes its path even before it reaches the line of symmetry [001] – [111]. The tensile axis follows this second path and overshoots into the conjugate system.

It is evident from the above observation that a higher value of the hardening parameter for a collinear lock predicts the overshooting behavior better then the case when a weak collinear interaction parameter is used. In the latter simulations, the transient from single glide to the double glide regime does not seem to occur suddenly as it does in the former. The dislocations on the primary and conjugate slip systems work as forest dislocations for each other and may interact to form a Lomer junction. Tisone et al. [11] suggest a model for describing overshooting in Cu-15% Al based on failure of Lomer junctions due to bowing out of mobile dislocations gliding on the conjugate slip system. For a given length of Lomer junctions, the bow out of the mobile dislocations on conjugate slip system occurs for a critical stress [11]. The smaller the length of the Lomer junctions, more stress will be needed for starting dislocations to glide on the conjugate slip system. As mentioned earlier in section I and elsewhere (cf. [10]), collinear interaction of dislocations causes formation of smaller dislocation segments on the interacting slip systems. Though primary and conjugate slip systems do not mutually interact by collinear reactions, these systems may interact with other latent systems which cause collinear interactions with these. These separate reactions may further decrease the length of the Lomer junctions formed by mutual interactions of primary and conjugate slip systems and therefore extending the overshooting. It is also suggested by Tisone et al. [11] that more frequent cross-slip causes formation of a random distribution of forest dislocation segments and that the dislocation glide is easier through a randomly

distributed forest as compared to a planar distribution. As first defined by Franciosi and Zaoui [12] and as incorporated in the present CPFEM model, a collinear hardening parameter represents interaction of cross-slip systems. A higher value of the collinear parameter represents, indirectly, a higher activity of cross-slip interactions. Therefore a higher value of the collinear lock parameter causes creation of smaller dislocation segment lengths on the interacting planes and a more random distribution of forest dislocations. This explanation suits well the observations in the present simulations but has scope of further examination. As suggested by Devincre et al. [9], the latent hardening parameters are non-dimensional parameters and must be the same for all FCC crystals. This offers motivation for a further study for distinguishing the extent of overshooting in different crystals [7] (e.g. Cu and Al which are supposed to have the same values of the collinear hardening parameter but different extent of cross-slip due to a substantial difference in the stacking fault energy).

5.2 Plane strain deformation of bicrystals

In this section studies on the rotations and split of the crystallite orientations during plane strain deformation of bicrystals are presented. The predictions by the CPFEM model are compared against the experimental observations. Orientations of the crystallites of the bicrystals are given in Table 5.5 and are shown on the crystallographic orientation map in Fig. 5.7. Note that {001} and {111} crystallographic pole figures are used for bicrystal 1 and bicrystal 2 respectively for easy comparison with the results from literature. Bicrystal 1 and 2 are deformed up to 10% and 30% thickness reductions respectively.

Table 5.5 Orientations of the crystallites in bicrystals 1 and 2

Bicrystal crystal Identification	Crystallite Identification	φ_1 (^{o})	Φ (^{o})	φ_2 (^{o})
1 (cf. Prasannavenkatesan et al. [13])	A	320.175	50.443	51.813
	B	318.656	41.024	54.964
2 (cf. Field and Alankar [14]	A	40.3	57.0	57.0
	B	267.1	20.0	182.8

Fig. 5.8 and Fig, 5.9 show the comparisons of the evolution of orientations for crystallite A and crystallite B respectively against the experimental observations and predictions by Asaro's model, a power law model, and Bassani's model [13]. The predictions by the current CPFEM model compare reasonably well against the experimental work and the other models. Fig. 5.10 shows the orientation spread in the crystallites A and B of bicrystal 2 after a thickness reduction of 30%. The CPFEM model is able to capture the orientation evolutions fairly closely. For the simulation of bicrystal 2, 180 elements of C3D8 type in ABAQUS^{TM}/Standard are used to mesh a geometry of 0.40 mm x 0.24 mm x 0.12 mm. The interface of the two grains is along the XZ plane. The thickness reduction is done along the '-' Z direction and any dimension changes are restricted along the Y direction.

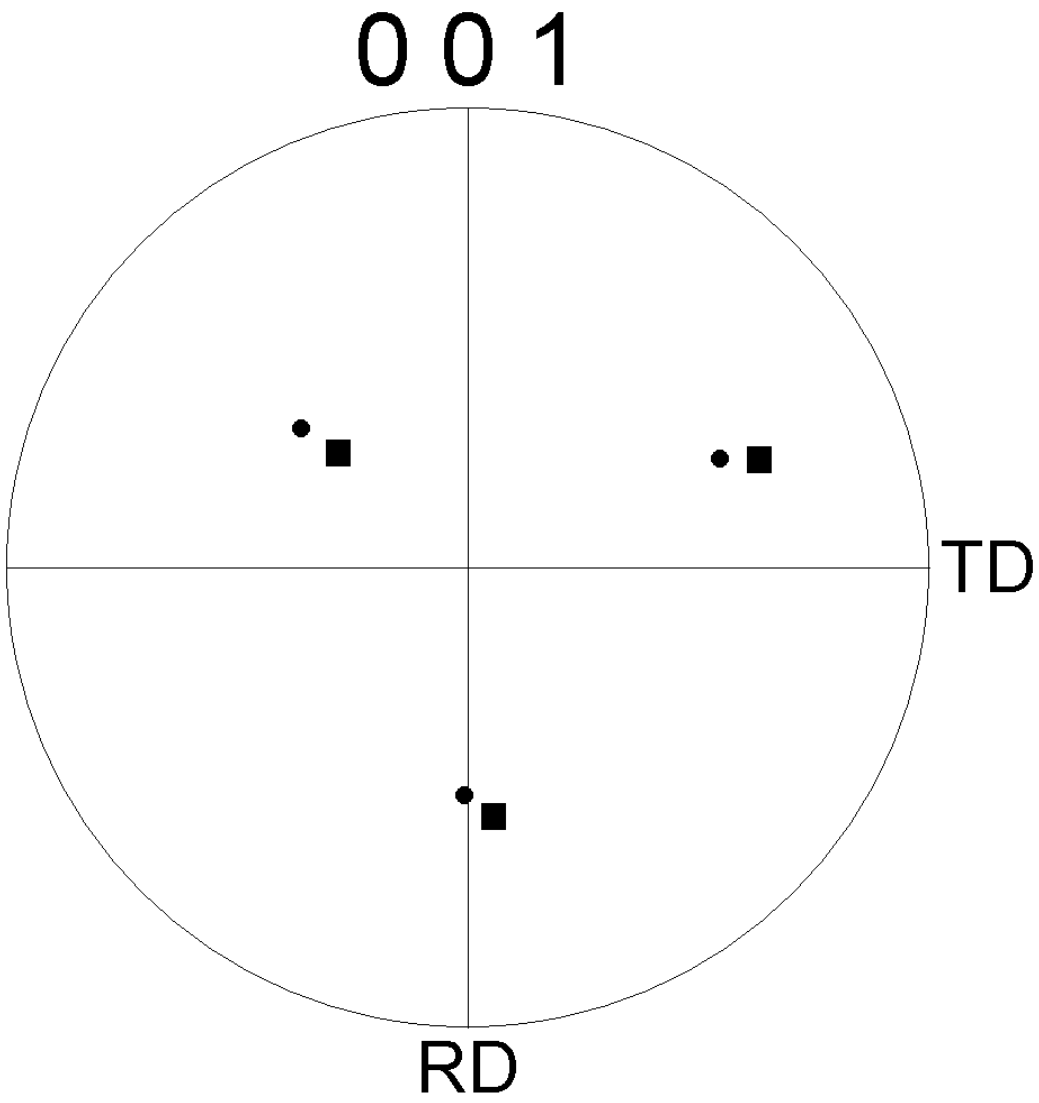

(a)

Figure 5.7 Initial orientations of crystallites in the bicrystals. In each bicrystal crystallite A is represented by square symbols and crystallite B is represented by circles (a) Bicrystal 1, (b) Bicrystal 2.

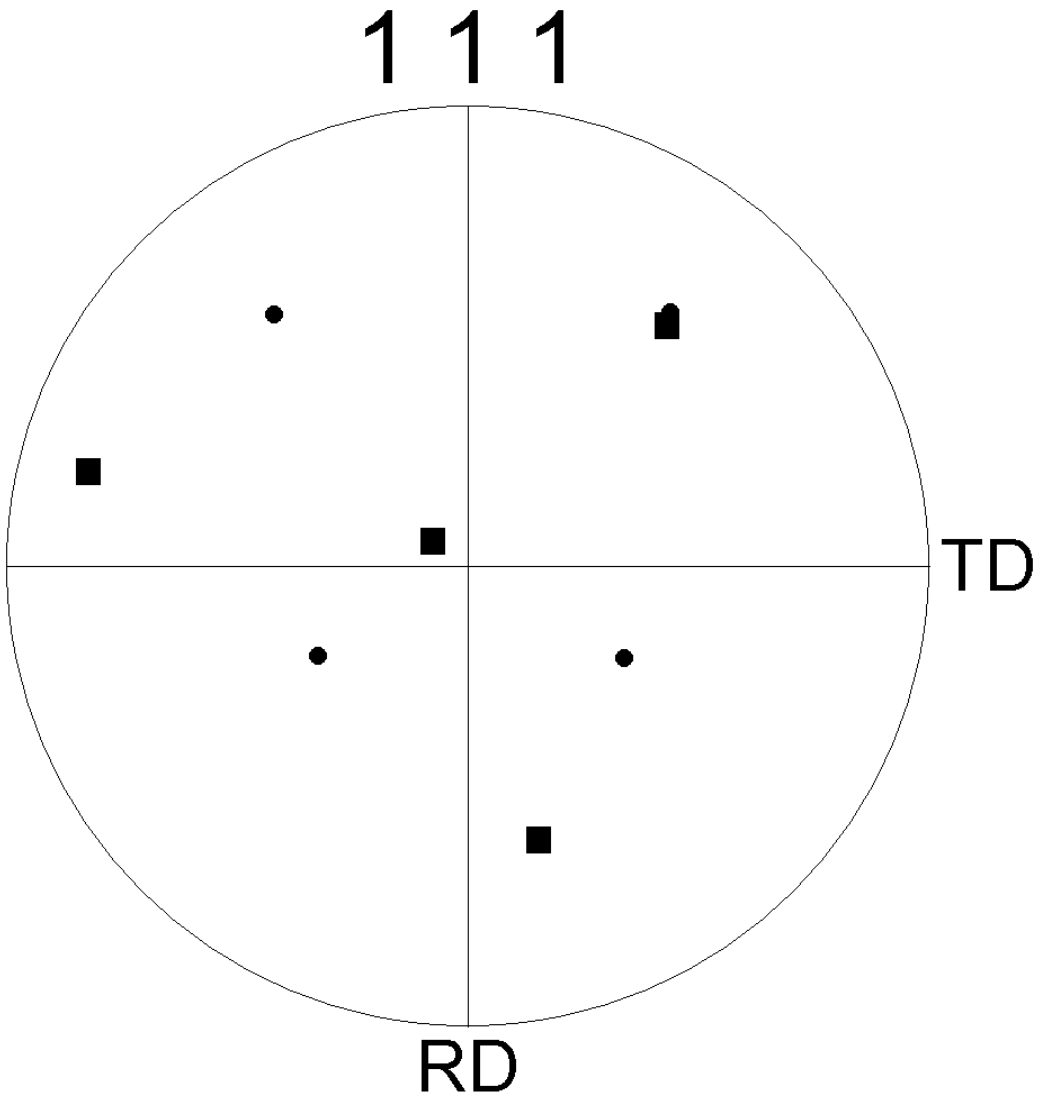

(b)

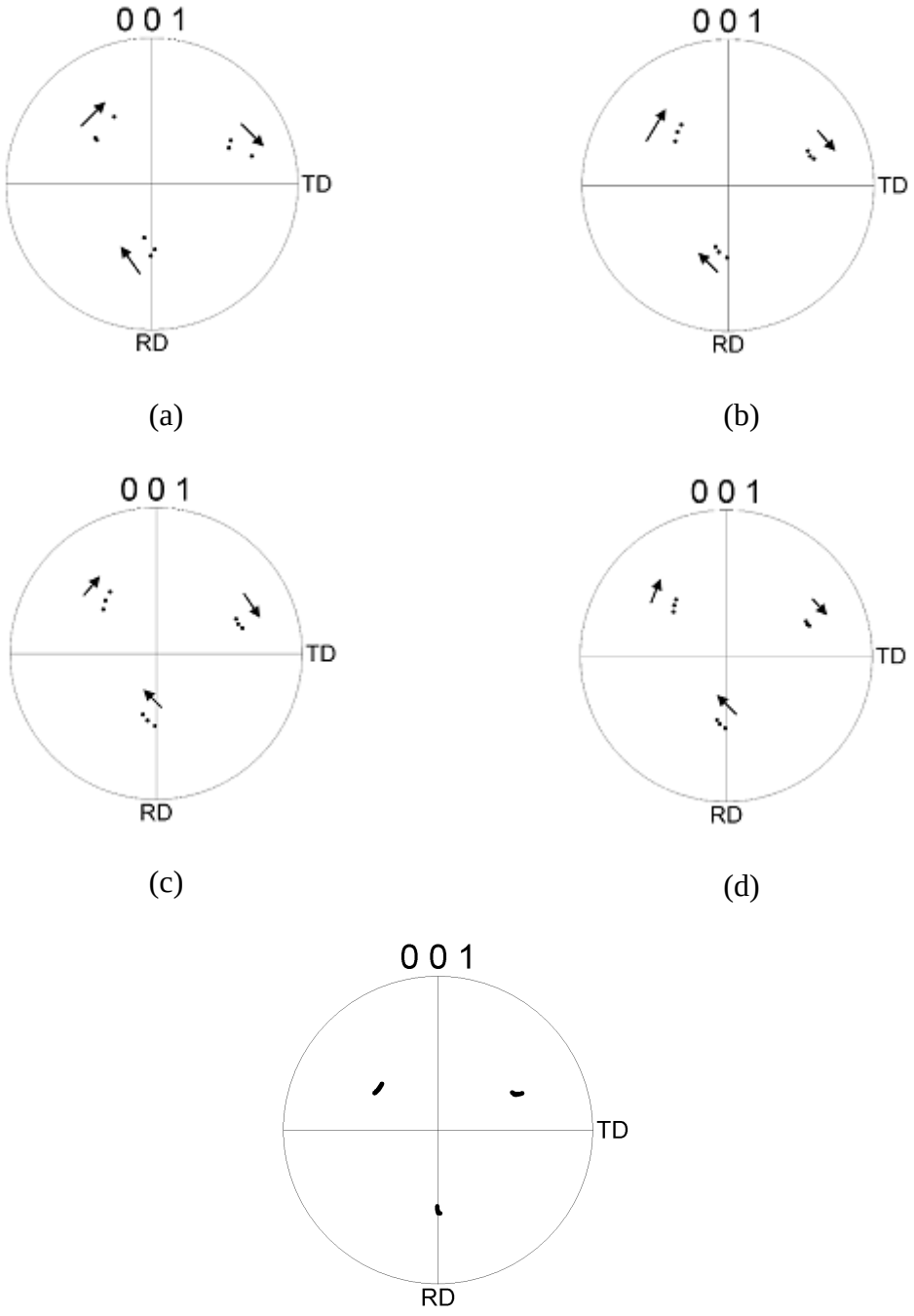

Figure 5.8 Change of orientation of crystallite A in bicrystal 1 after a thickness reduction of 10 %. (a) Experimental observation [13], (b) Asaro's hardening model [13], (c) Power law [13], (d) Bassani's model [13], (e) present work

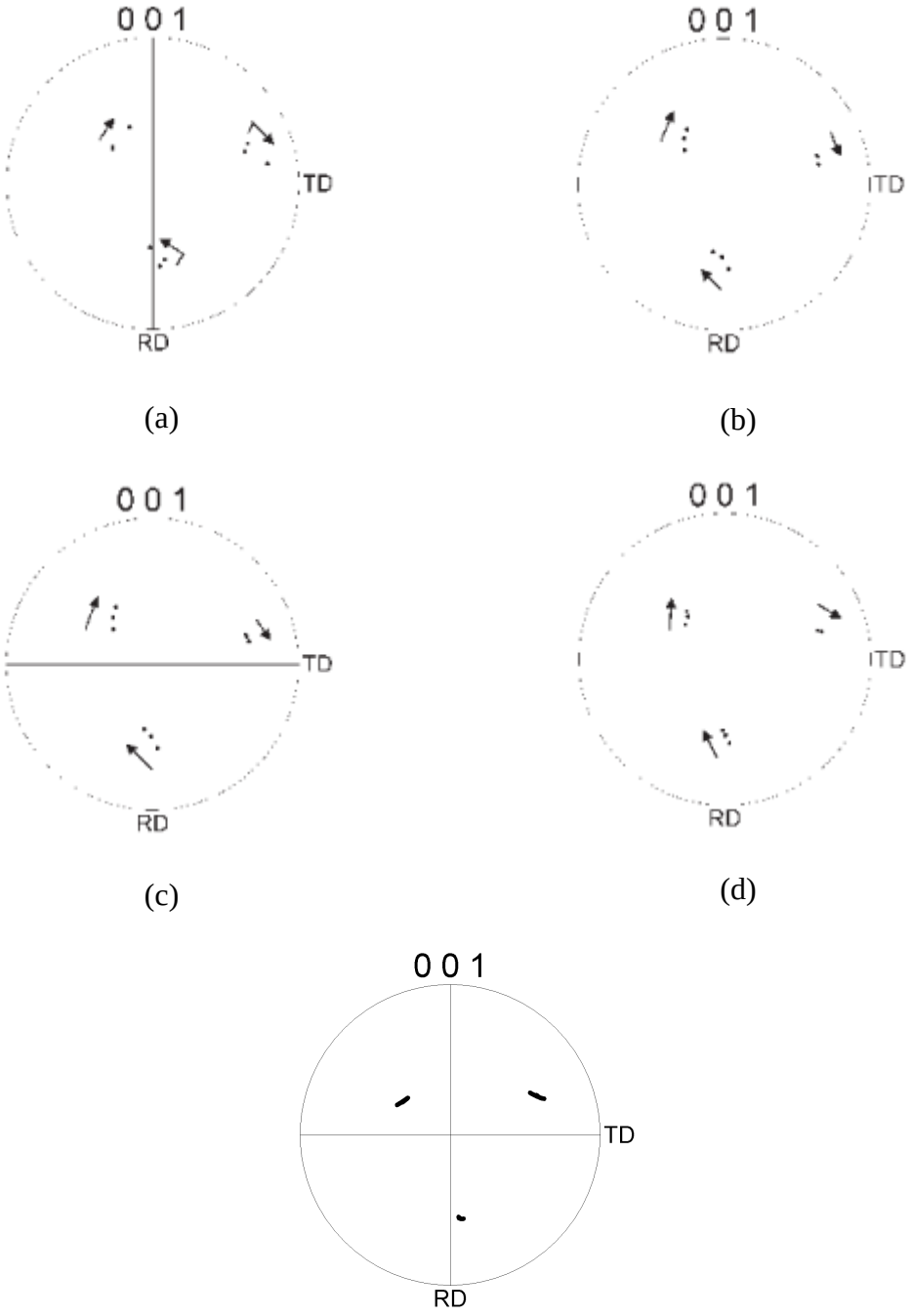

Figure 5.9 Change of orientation of crystallite B in bicrystal 1 after a thickness reduction of 10%. (a) Experimental observation [13], (b) Asaro's hardening model [13], (c) Power law [13], (d) Bassani's model [13], (e) present work

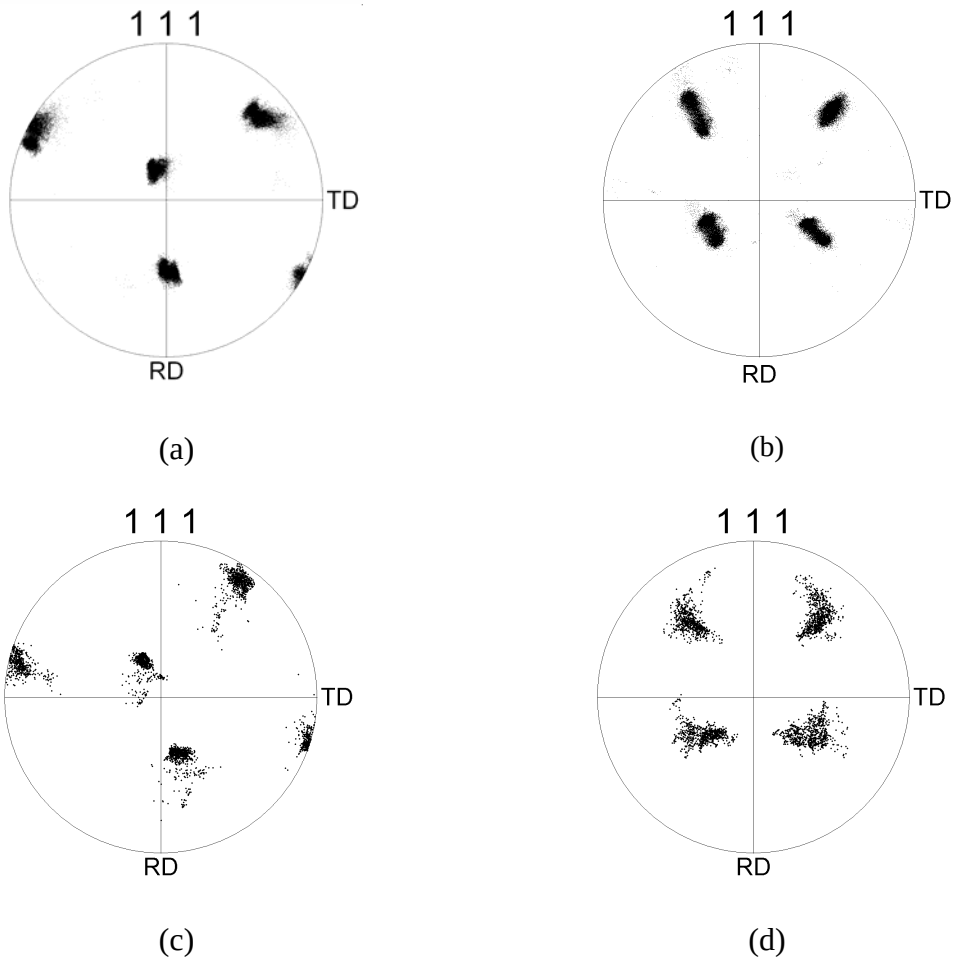

Figure 5.10 Orientation spread crystallite A and crystallite B of bicrystal 2 after a thickness reduction of 30 %. (a), and (c) represent crystallite A and (b) and (d) represent crystallite B. (a) and (b) are experimental observations [14].

5.3 Crystallographic texture evolution in a polycrystal

The FE formulation uses a simplified geometry of 0.2 mm x 0.2 mm x 0.1 mm, consisting of 500 elements. C3D8 type elements are used which are 8 node, 8 integration points, linear elements in ABAQUS^{TM}/Standard library. The rear face perpendicular to X is restricted for displacement in X. Both faces normal to the Y direction are restricted in the

Y direction. The rear face normal to the Z direction is restricted for Z displacement and the front face normal to the Z direction is given a displacement to cause an 80% reduction in distance between the two faces normal to the Z direction. Each element is treated as a single grain and is assigned a random orientation. Fig. 5.11a represents the random arrangement of material point orientations in the FEM mesh. The thickness is reduced using the prescribed displacement. In the present study a constant strain rate of 5.33e-05 s^{-1} is used.

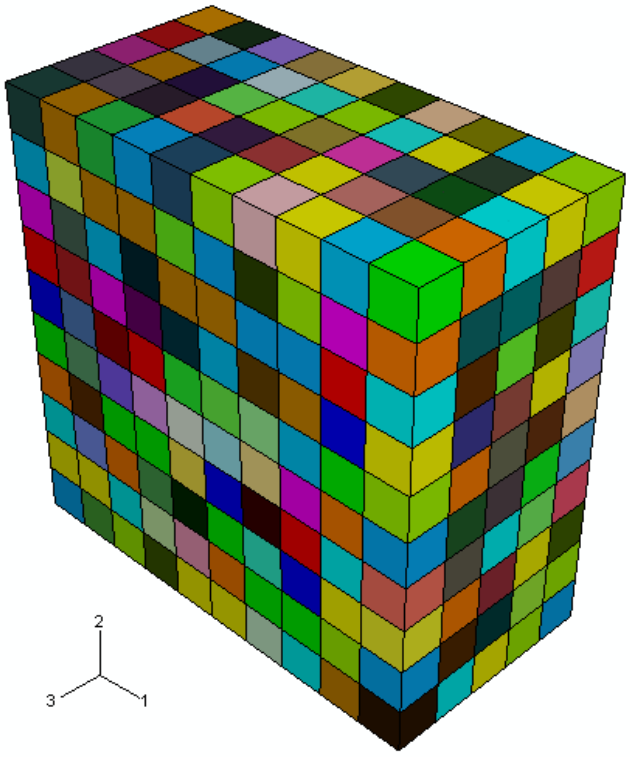

(a)

Figure 5.11 (a) Initial FEM mesh; 500 C3D8 type 8 node brick elements with random orientation. (b) Deformed mesh showing von Mises stress distribution with 80 % thickness (Z direction) reduction in plane strain compression of pure aluminum polycrystal.

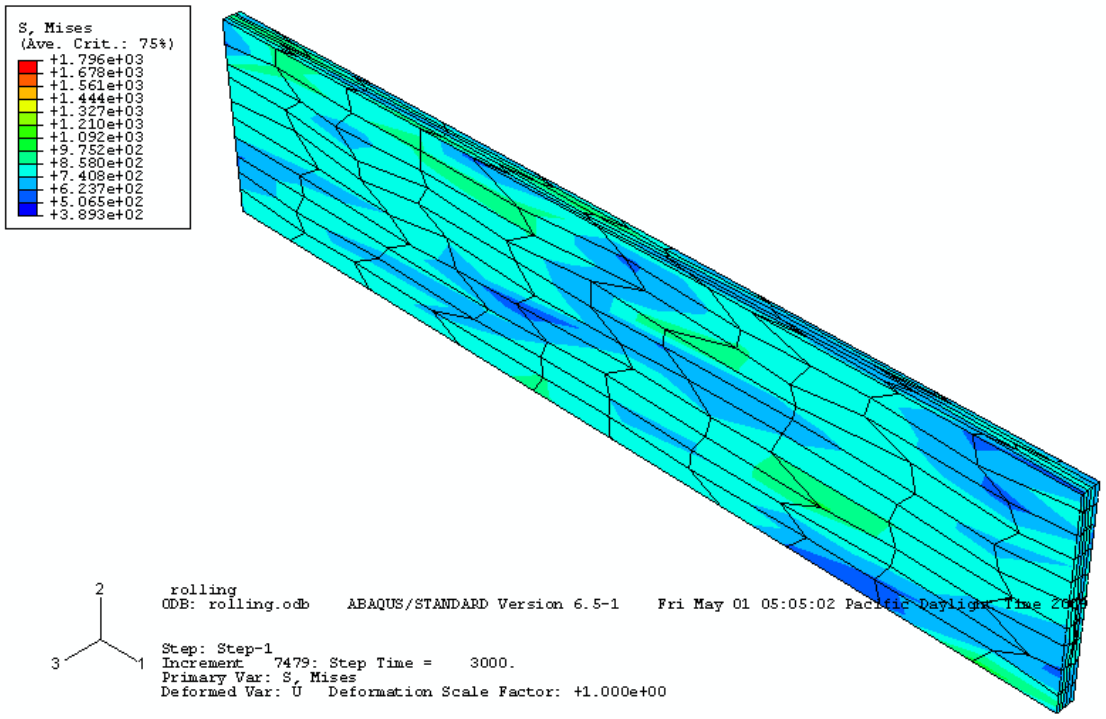

(b)

Results presented here are due to homogenous deformation and it is considered that the texture evolution in this case is representative of the whole material volume. Von Mises stress distribution in the deformed body after a thickness reduction of 80% is shown in Fig. 5.11b. Fig. 5.12 shows the “random” initial crystallographic texture in the material considered in this study. Fig. 5.13 shows the prediction of texture evolution after 80% thickness reduction and demonstrates a nominally correct texture prediction by the CPFEM model. This texture plot is typical of FCC material deformed under plane strain compression and can be validated with a great degree of agreement against an experimental observation reported in the literature. Any qualitative or quantitative comparison with experimental observation is not being presented here. The forthcoming part of this work, discusses various components of texture in plane-strain compression.

The strongest texture component seen in this figure is the ‘S’ component $\{123\}\langle 63\bar{4}\rangle$. The high intensity regions in the texture plots are the expected fibers that evolved during rolling of FCC metals. α-fiber $\{110\}\langle \mathbf{uvw}\rangle$ and β-fibers $\{100\}\langle \mathbf{uvw}\rangle$ are the two main fiber components.

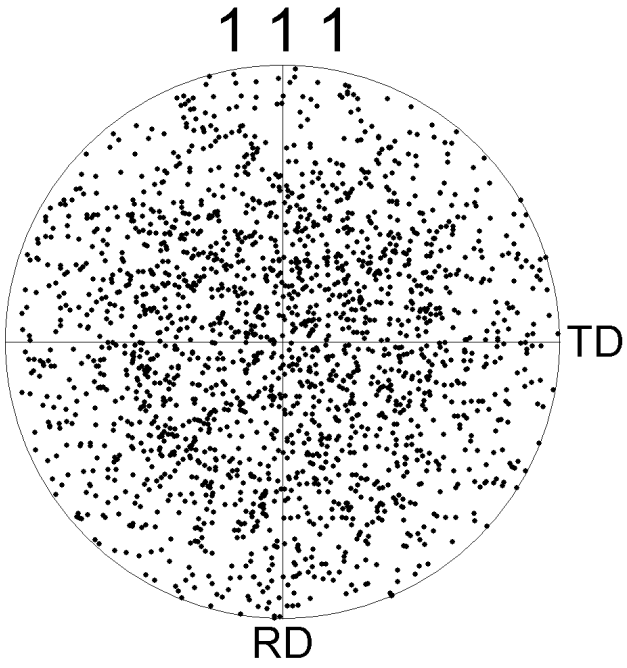

(a)

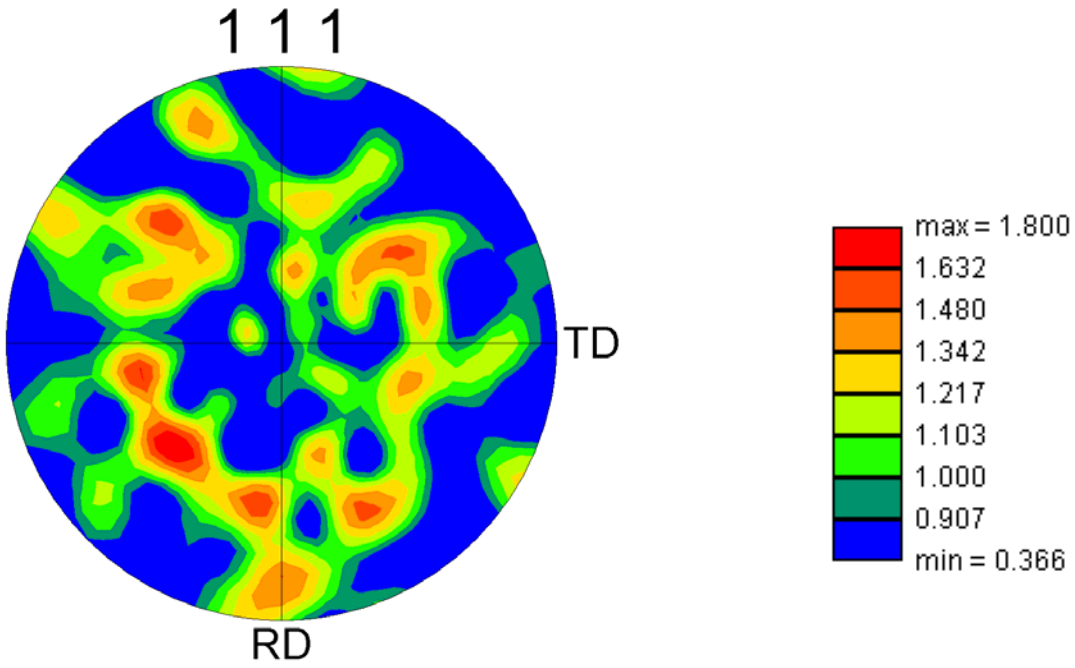

(b)

Figure 5.12. Initial random orientation of grains (a) Stereographic projection 111 (b)

Texture 111

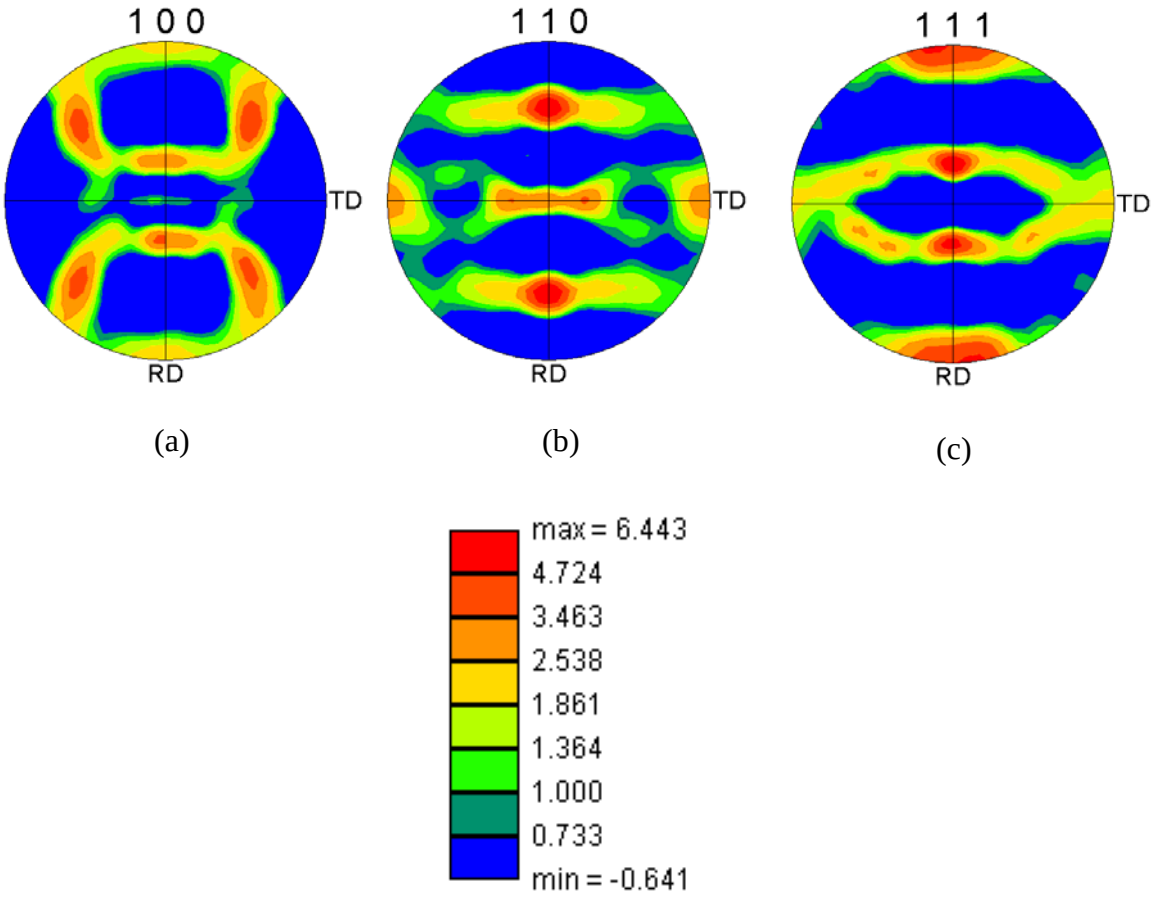

Figure 5.13 Evolution of texture in plane strain compression of pure aluminum polycrystal at 80 % thickness reduction.

Fig. 5.14 shows a comparison of the texture evolution for reductions in thickness to 40 %, 70 % and 80 %. While the character of the texture over this range changes little, the major texture components increase in intensity.

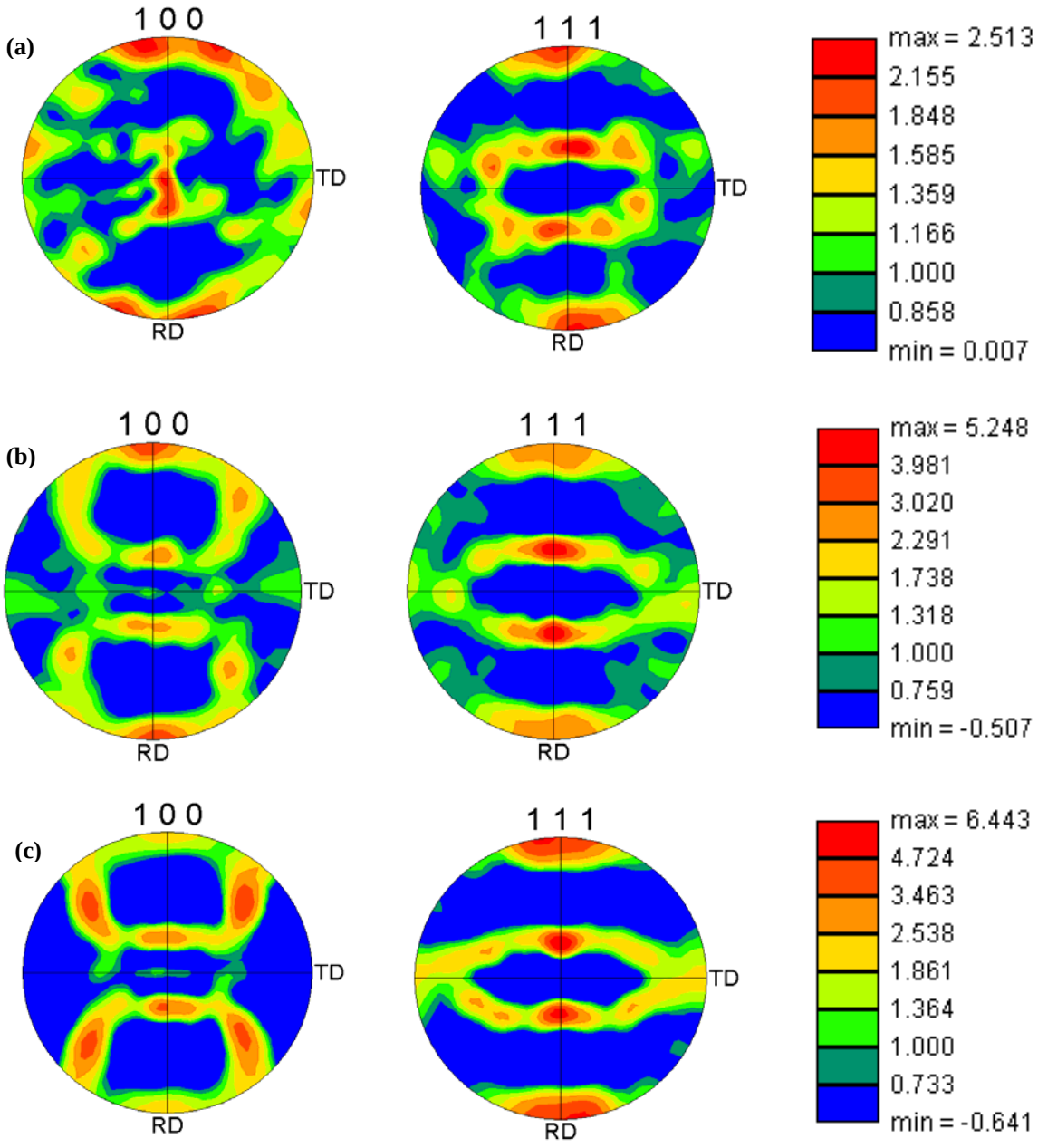

Figure 5.14 Comparison of texture evolution at different thickness reductions. (a) 40 % (b) 70 % (c) 80 %

Euler space ($\varphi_2 = constant$) representation of Fig. 5.13 can be seen in Fig. 5.15. Relatively strong 'brass' $\{110\}\left[\bar{1}12\right]$ and 'copper' $\{112\}\left[11\bar{1}\right]$ texture components are

present in the simulation and a minor component of cube $\{001\}[100]$ texture can be seen. Sections $\varphi_2 = 0^o$ and $\varphi_2 = 90^o$ show the presence of a weak α-fiber and the high intensity peak running through the constant φ_2 sections indicates a strong β-fiber as expected for rolled Al [15].

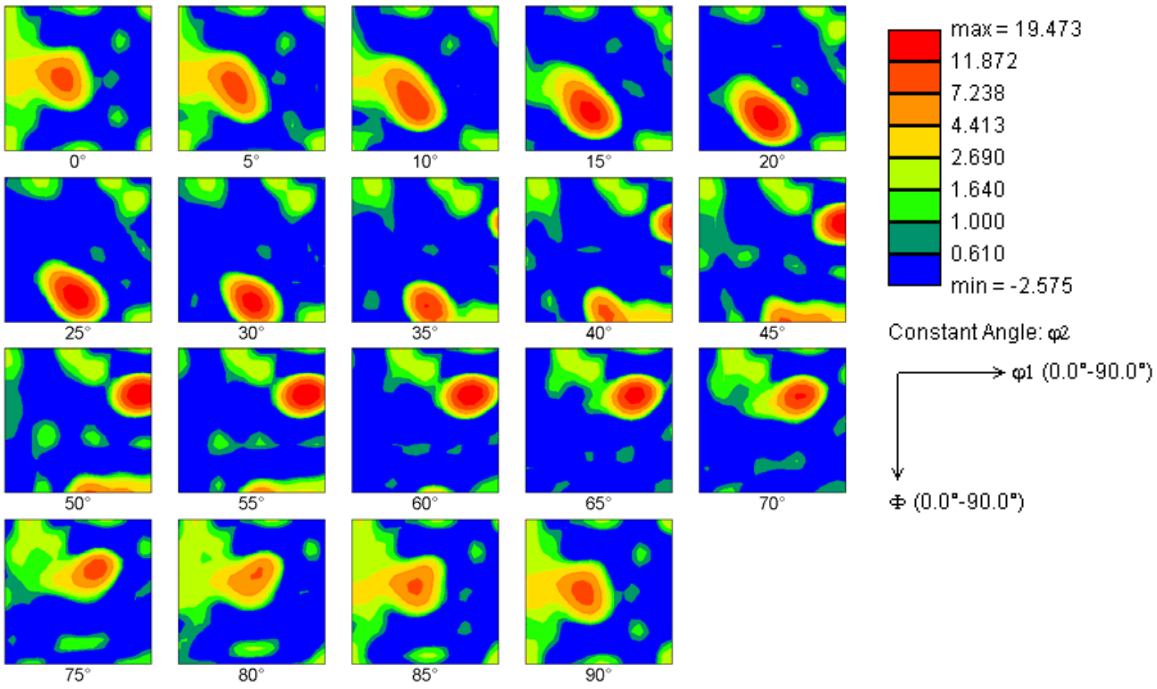

Figure 5.15. Rolling texture represented in Euler space showing few texture components that are present.

Fig. 5.16 shows evolution of the alpha and beta fibers at different reductions in the simulation. The α-fiber connects the 'brass' $\{110\}[\bar{1}12]$ to 'Goss' $\{110\}[001]$ components and can be seen clearly on the 100 texture plot in Fig. 5.13 and in the Euler space plot of Fig. 5.15 at section $\varphi_2 = 0^o$.

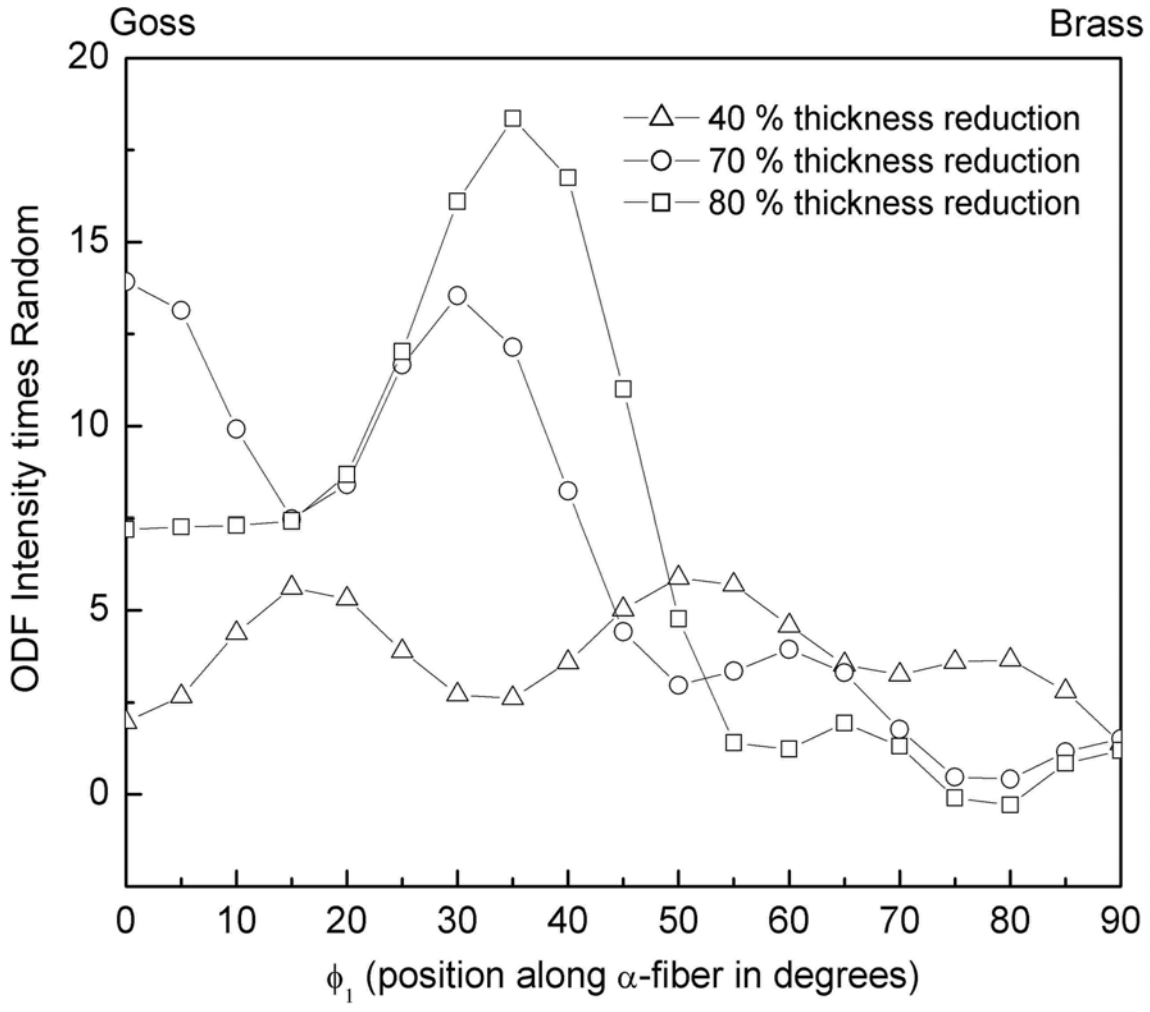

(a)

Figure 5.16 Evolution of (a) α -fiber and (b) β -fiber with increasing deformation

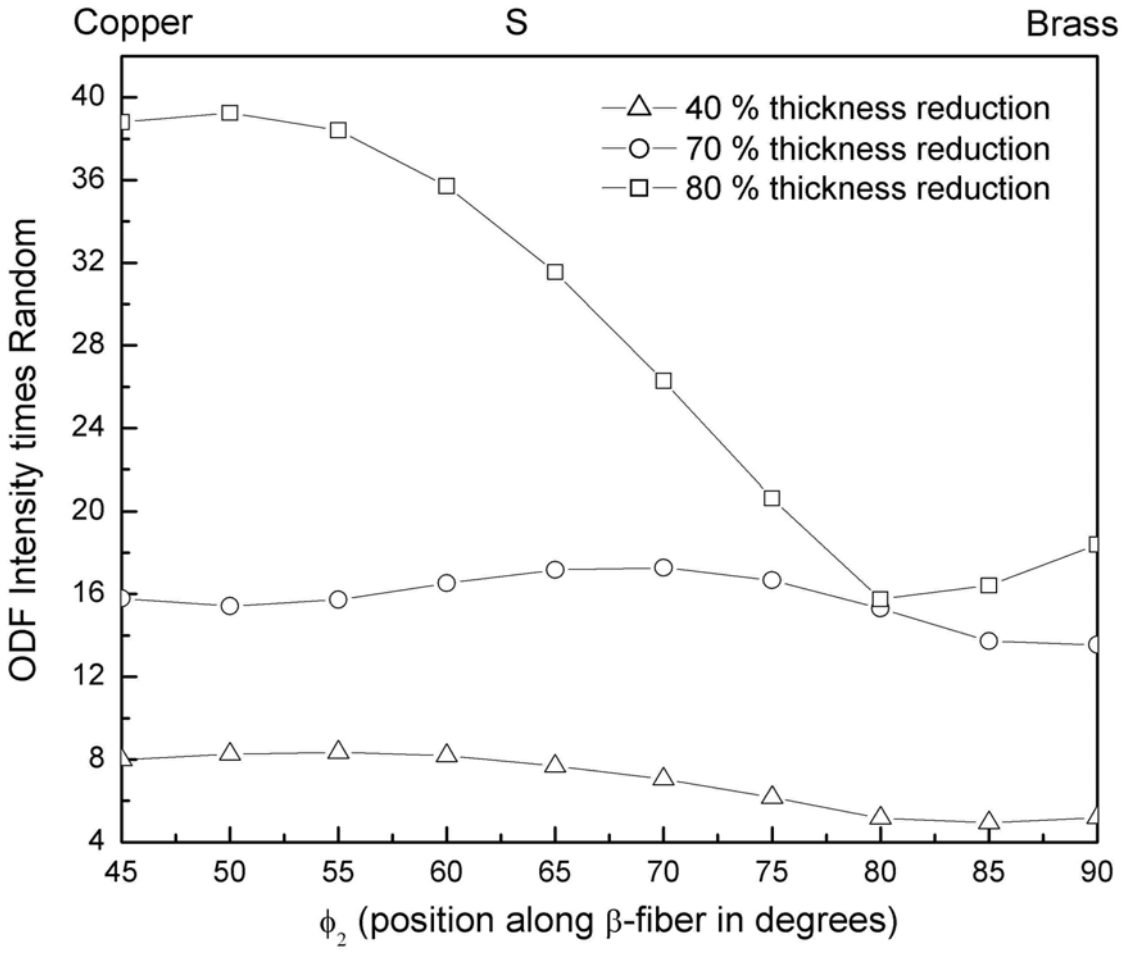

(b)

Fig 5.17 presents texture prediction by the model during simple shear of a 500 grained polycrystal after 80% shear. The initial geometry for this simulation is the same as for the simulation of the plane strain compression and initially all 500 grains are assigned identical sets of random orientations. These predictions of crystallographic evolution compare reasonably well with the results presented in the literature e.g. [15]. 'A' partial fiber – {111}<uvw>, 'B' partial fiber – {hkl}<110> and the 'C' component – {001}<110> are clearly visible.

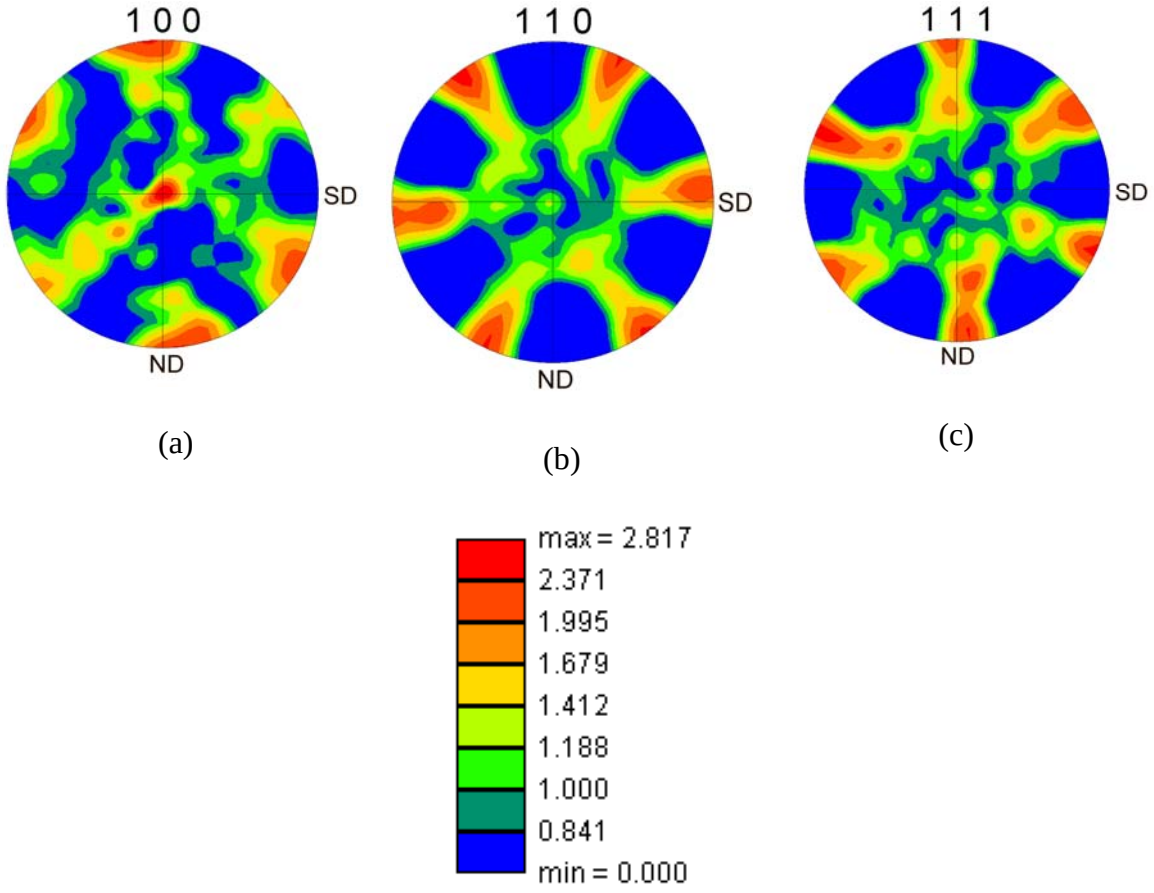

Figure 5.17. Texture evolution after 80% simple shear of pure aluminum. 'SD' on the texture plots represents the shear direction.

5.4 Dislocation density patterning

The initial dislocation density in all the above simulations of plane strain compression is 1×10^{8} m.m^{-3} which is uniformly distributed in the material volume. As the deformation proceeds, the dislocation density evolution varies spatially. Non-uniform spatial distribution of dislocation density comes due to varying crystallographic orientation of each material point and due to local deformation gradient. The spatial distribution of total

dislocation density (i.e. dislocation patterning) is shown in Fig. 5.18 at 40% and 70% thickness reduction. Qualitatively the evolving heterogeneity can be observed in Fig. 5.18a and 5.18b with increasing deformation. A quantitative description of the same is presented using a coupling of dislocation densities with the crystallographic orientations of different material points. Fig. 5.19 shows the distribution of dislocation density for the corresponding orientation of the material point on a stereographic projection. The legends in Fig. 5.19 show the dislocation densities in multiples of 10^{14} $m.m^{-3}$. The increasing degree of heterogeneity of dislocation patterning with proceeding deformation can be envisioned using the maximum and minimum values of the dislocation densities. At 40% deformation the dislocation density distribution is still more of a random type. Whereas, at 70% the stereographic projection shows a definite pattern which is similar to the texture plot at 70% and the variation of dislocation density for different orientations of crystallites is much higher than what is observed at 40%.

The hardening behavior of the two crystallites A and B in bicrystal 1 discussed in section 5.2 can be compared referring to total dislocation density and initial orientations (see Fig. 5.20). Crystallite A is close to the <111> orientation and shows higher accumulated dislocation density. Especially, the effect of the interface between the two crystallites can be seen clearly as the highest accumulated dislocation density is observed in the neighborhood of the interface. However, due to lack of transport of non-local effect across the interface, crystallite B does not show any increased dislocation density around the interface. A more detailed discussion of hardening is presented referring to Taylor factors and dislocation density evolution in a multicrystal later in this chapter. To further

study the evolution of dislocation patterning, more complex studies on the deformation of polycrystals are considered in the forthcoming sections.

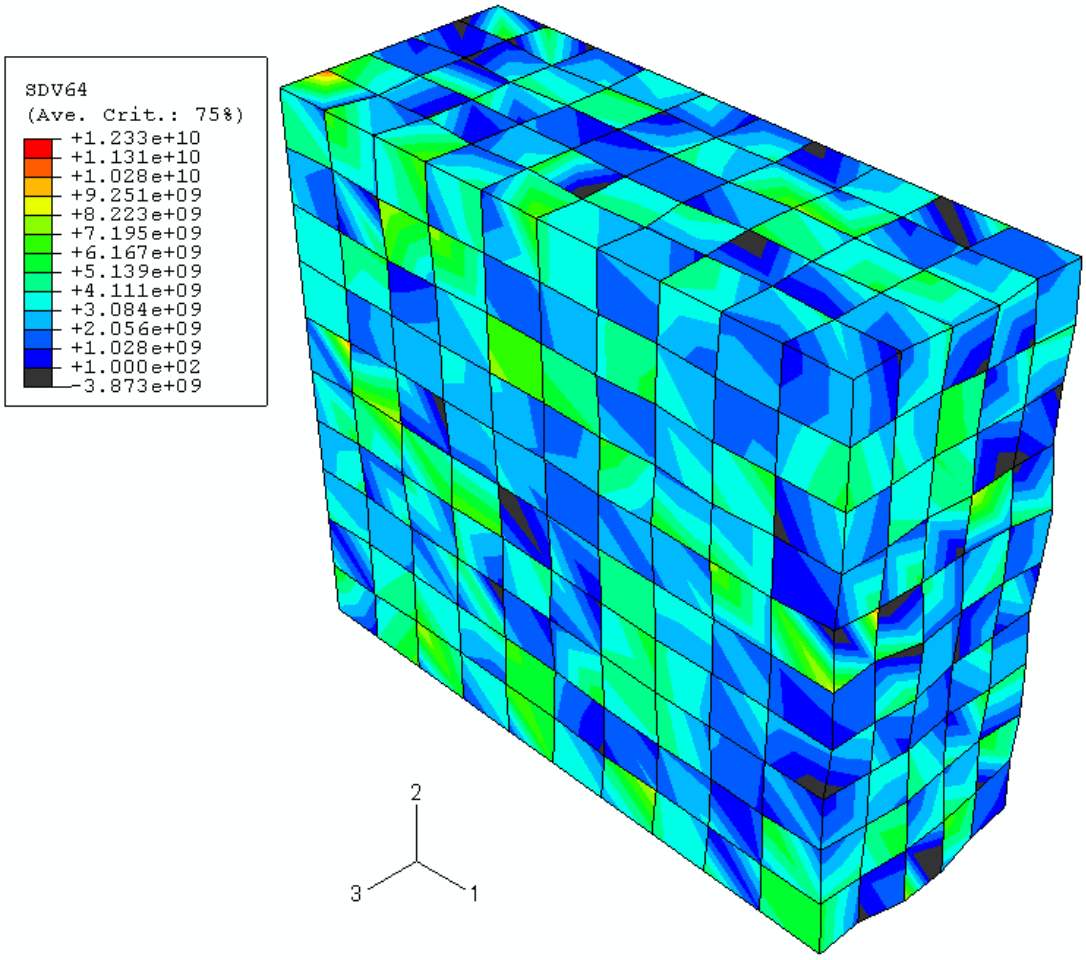

(a)

Figure 5.18 Dislocation patterns during plane strain deformation. Dislocation density in the legend is in multiples of 1×10^6 m.m^{-3} (a) 40% deformation, (b) 70% deformation

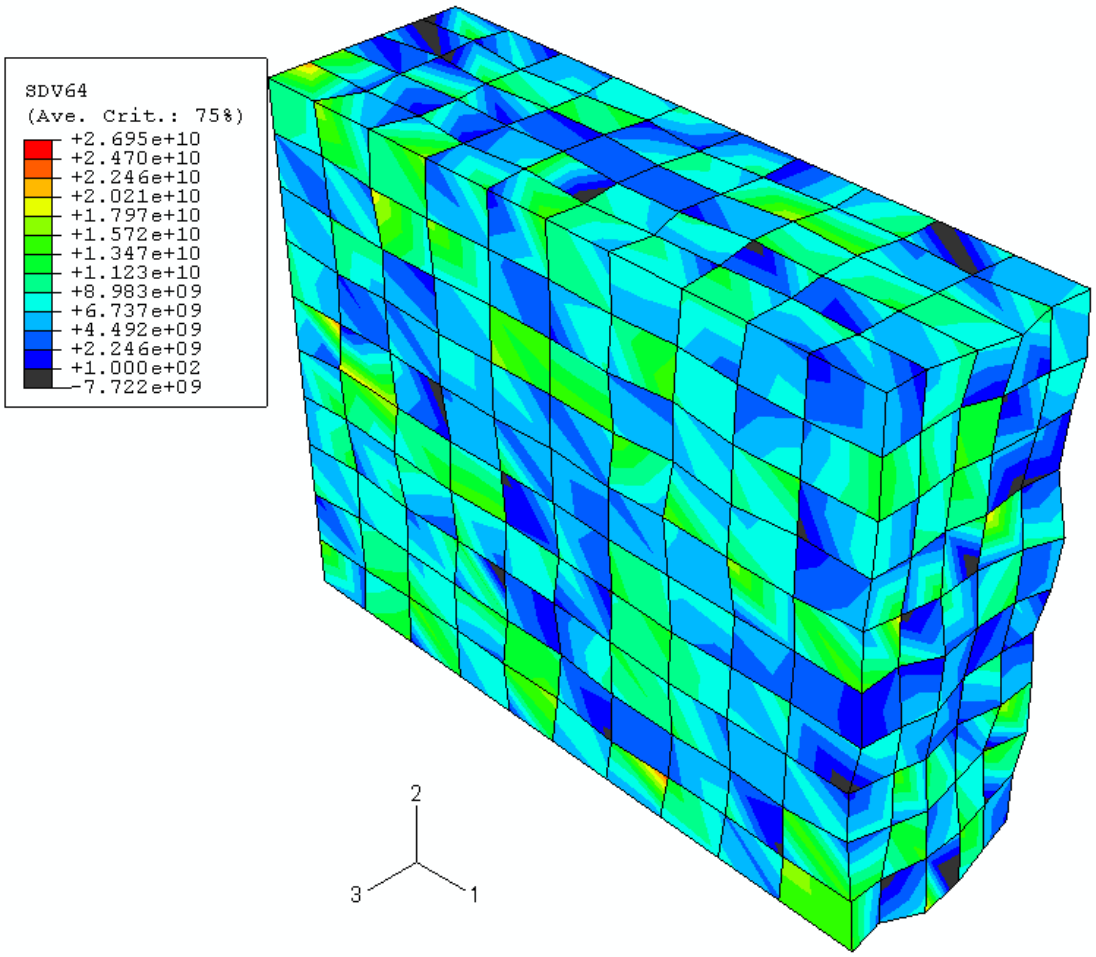
SDV64
(Ave. Crit.: 75%)
+2.695e+10
+2.470e+10
+2.246e+10
+2.021e+10
+1.797e+10
+1.572e+10
+1.347e+10
+1.123e+10
+8.983e+09
+6.737e+09
+4.492e+09
+2.246e+09
+1.000e+02
-7.722e+09
2
3
1

(b)

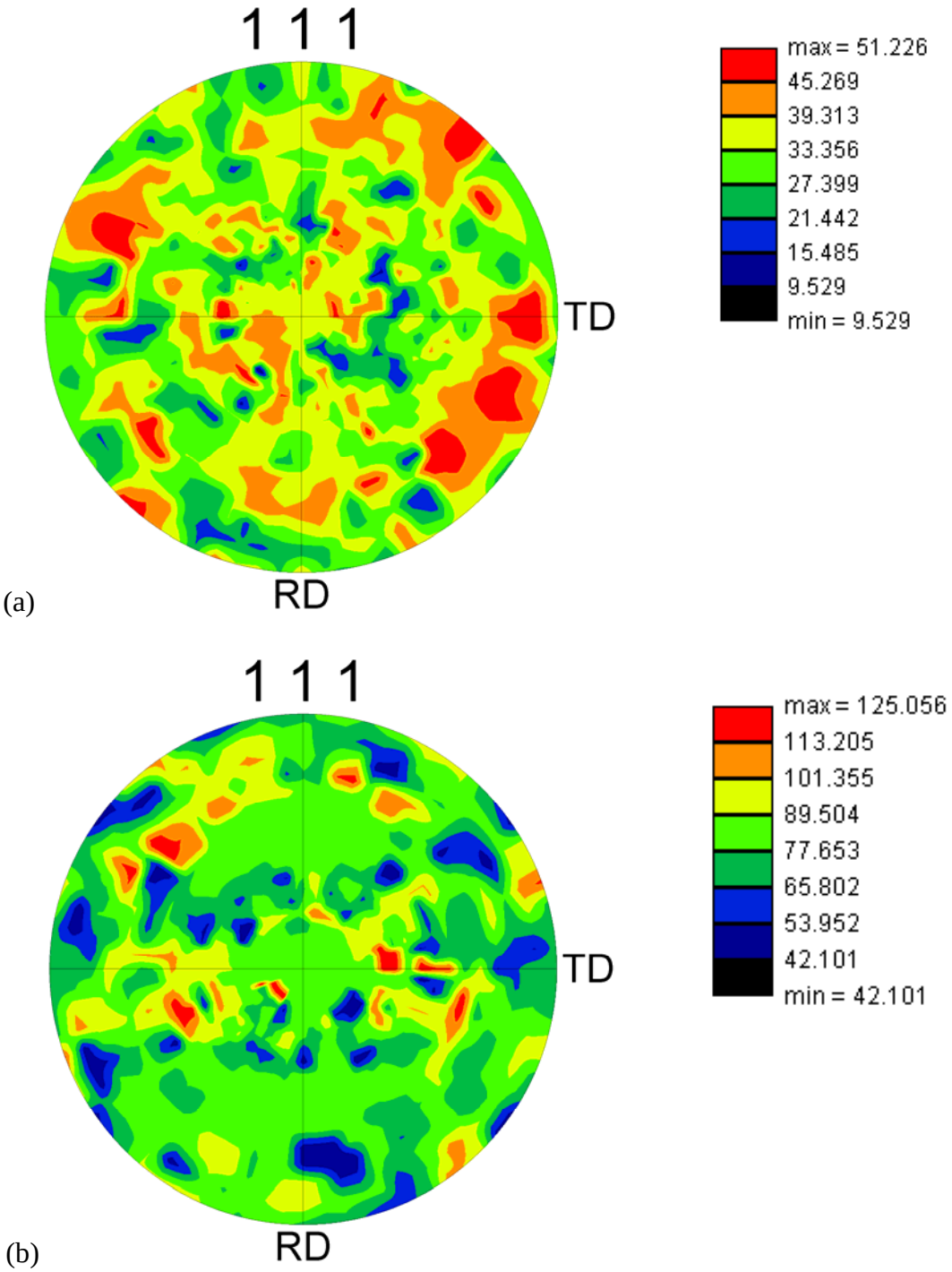

Figure 5.19. Dislocation density distribution in a polycrystal presented coupled with crystallographic orientations. (a) 40 % thickness reduction, (b) 70% thickness reduction. The legend shows dislocation density $\times 10^{14}$ m.m^{-3}.

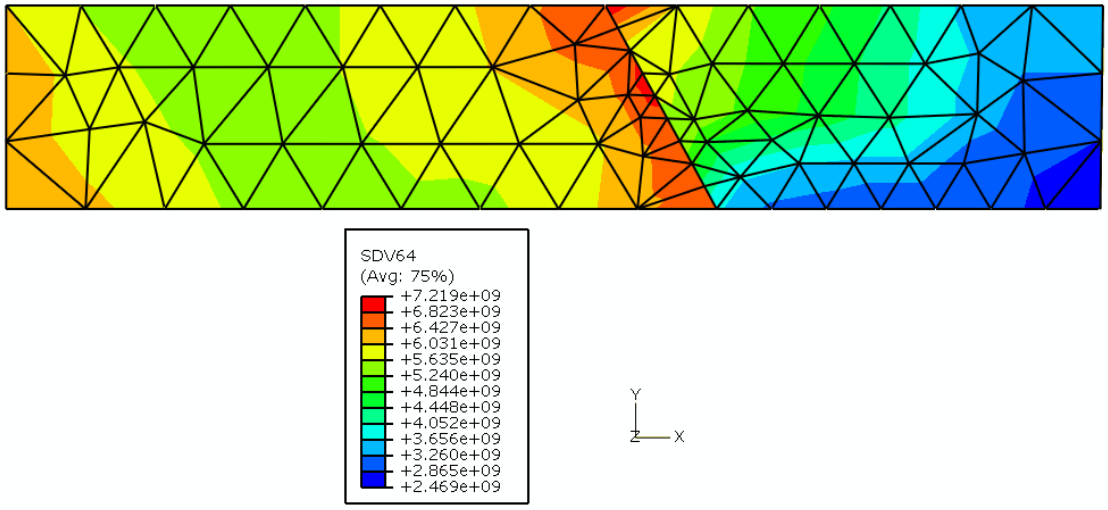

Figure 5.20. Dislocation density distribution in the bicrystal 1 after a thickness reduction of 10%. The legend shows dislocation density $\times$ 10^6 m.m^{-3}.

5.5 Channel die compression of 2D columnar multicrystals

5.5.1 Grain rotations and hardening in a 2D multicrystal

The microstructure evolution during plane strain compression of a columnar grained, two-dimensional single layer multicrystal of aluminum is investigated using the CPFEM model. The multicrystal under consideration here is the one studied by Prasannavenkatesan et al. [13] which consists of 10 large grains. The initial orientations of the grains are shown in Table B.1 in Appendix B. Initial crystallographic orientations of the grains are mapped onto a FEM mesh and the predictions of spatial distribution of accumulated strain and dislocation density distribution are compared. Rotations of selected grains during the deformation are compared with the experimental study done by the above authors in which orientation change was determined by interrupted measurements using EBSD technique.

The initial orientation map of the real multicrystal and the crystallographic orientations determined using electron backscatter diffraction patterns are shown on the standard crystallographic unit triangle in Fig. 5.21a and 5.21b respectively. The FE mesh for the simulation is generated using idealized mapping of the real microstructure studied by Prasannavenkatesan et al. [13]. The actual size of the specimen used in the aforesaid study is 20 mm x 3 mm x 3 mm. The FE mesh is formed of 2416, 4 node, 1 integration point elements, which are C3D4 type first order tetrahedral elements in ABAQUS^{TM}/Standard [2]. Deformation gradient is applied using displacement boundary conditions. The rear face perpendicular to the X direction is restricted for displacement in X. Both faces normal to the Y direction are restricted in the Y direction. The rear face normal to the Z direction is restricted for Z displacement and the front face normal to the Z direction is given a displacement to cause 15% reduction in the distance between the two faces normal to the Z direction (the thickness direction). In the present study a constant strain rate of 8.33e-03 s^{-1} was used.

Total meshed geometry is divided into 10 different groups of elements which make the crystallites of the multicrystal. These element groups are numbered from 1 to 10 and are assigned initial crystallographic orientations which are identical to the ones reported by the above researchers. Fig 5.22 shows the initial geometry and the FE mesh representation of the multicrystal. For the results shown in this section a non-uniform mesh was used (see Fig 5.22b) to minimize the simulation time. Relatively finer elements were used to mesh the regions of complex geometry and the regions across the grain boundaries. Nevertheless, later in this section we show a qualitative comparison of the results shown by coarse mesh and a uniformly finer mesh.

(a)

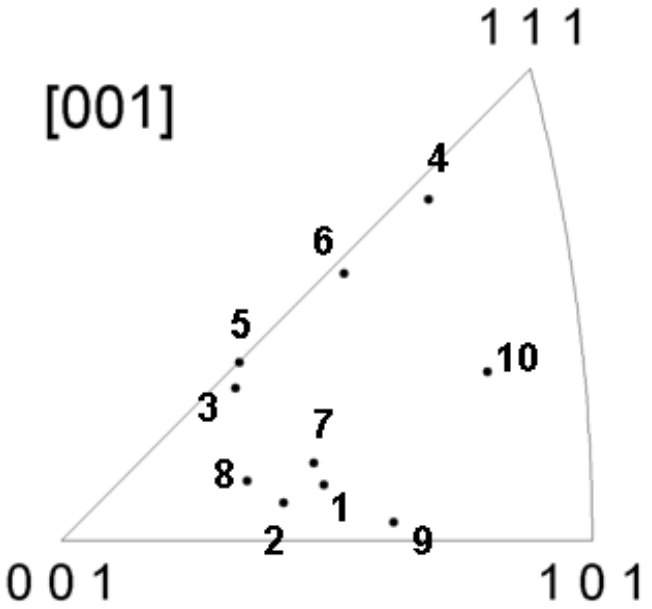

(b)

Figure 5.21. (a) Initial orientation imaging map of the multicrystal (b) Crystallographic orientations of the grains in the unit triangle [13].

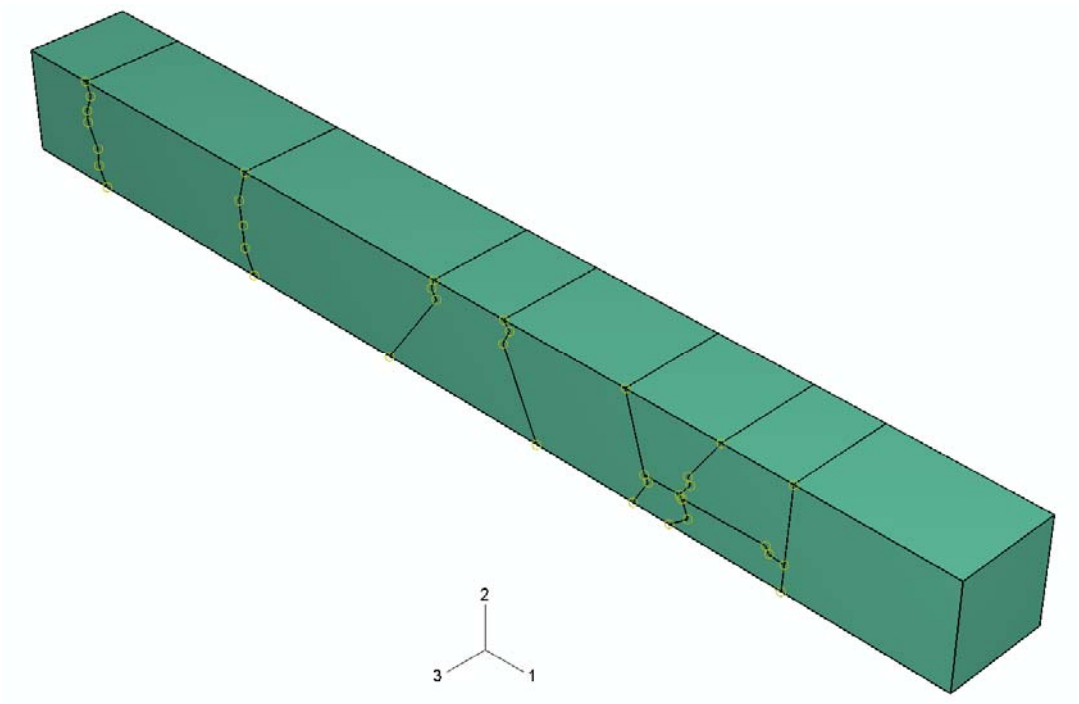

(a)

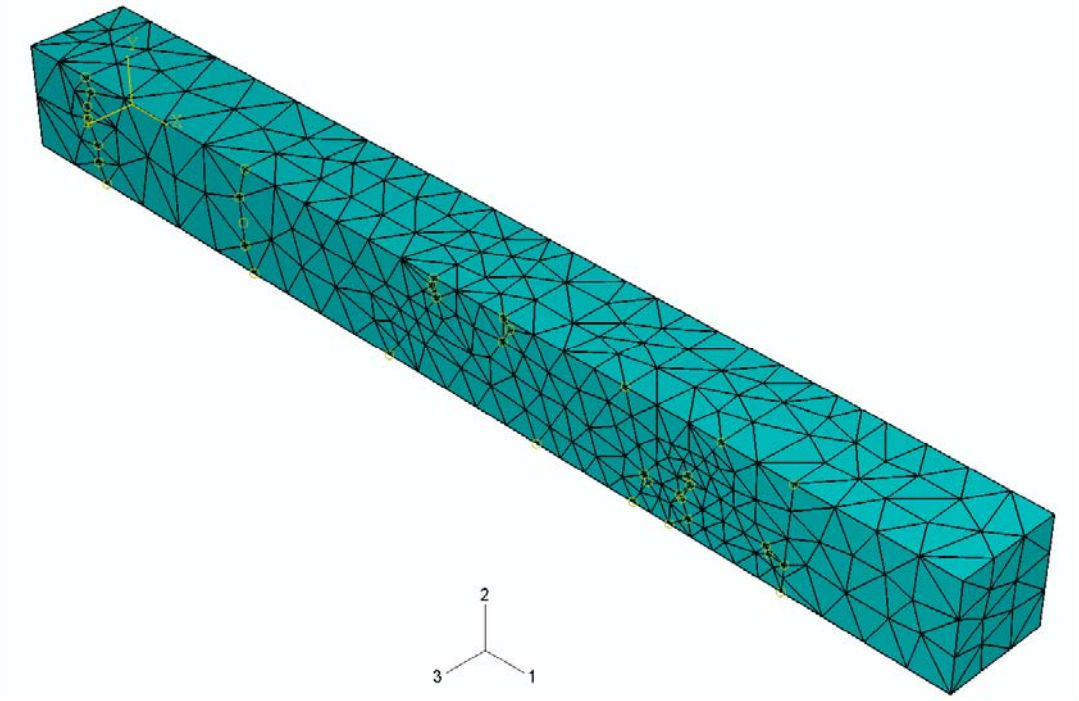

(b)

Figure 5.22 (a) Idealized mapping of the grain structure. (b) Finite element mesh to form a microstructure of a 10 columnar grain polycrystal

Fig 5.23a shows evolution of maximum principal strain which is remarkably non-uniform throughout the multicrystal. Noteworthy is that the grains oriented closer to the stable orientation <111> (e.g. grain 5) accumulate more strain as compared to the ones which are farther from a stable orientation (e.g. grain 3 and single glide oriented grain 1). The grains which share more grains in the neighborhood i.e. grains 5, 6, 7, 8, 9, and 10 and make more complex grain boundary junctions show more accumulated strain. The heterogeneous microstructure evolution is reflected due to the dislocation slip activity and here it is represented by the total accumulated dislocation density shown in Fig. 5.23b. The heterogeneous accumulation of strain and dislocation density distribution pointed out above is a result of grains interactions, local deformation gradient, and orientations of the crystallites. Therefore it is worthwhile to do a quantitative analysis of the underlying microstructure evolution in terms of dislocation density evolution, Taylor factor and the change of orientation of the grains during deformation.

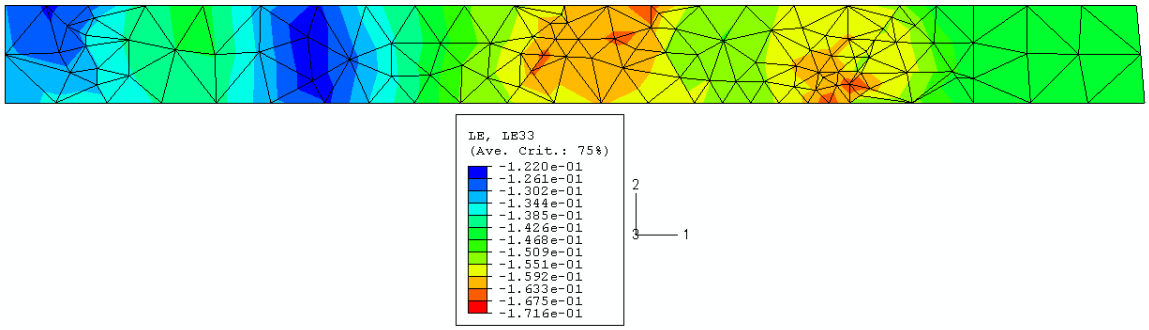

(a)

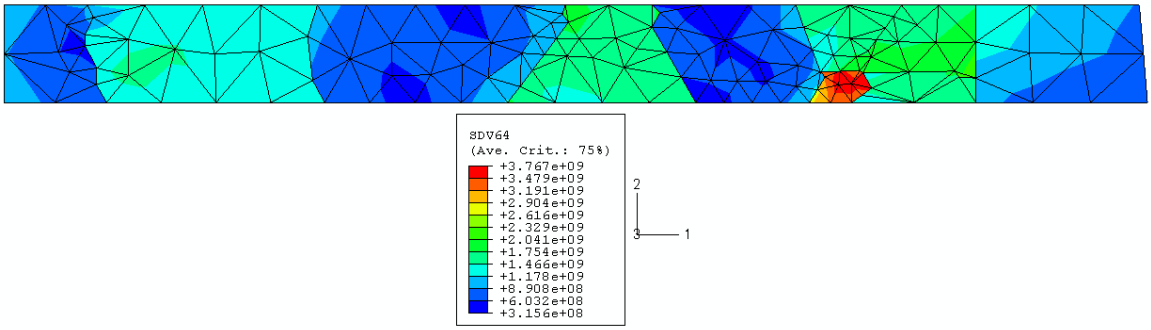

(b)

Figure 5.23 (a) Maximum principal strain (b) Total dislocation density distribution after ~ 15 % thickness reduction. The legend shows dislocation density $\times$ 10^6 m.m^{-3}.

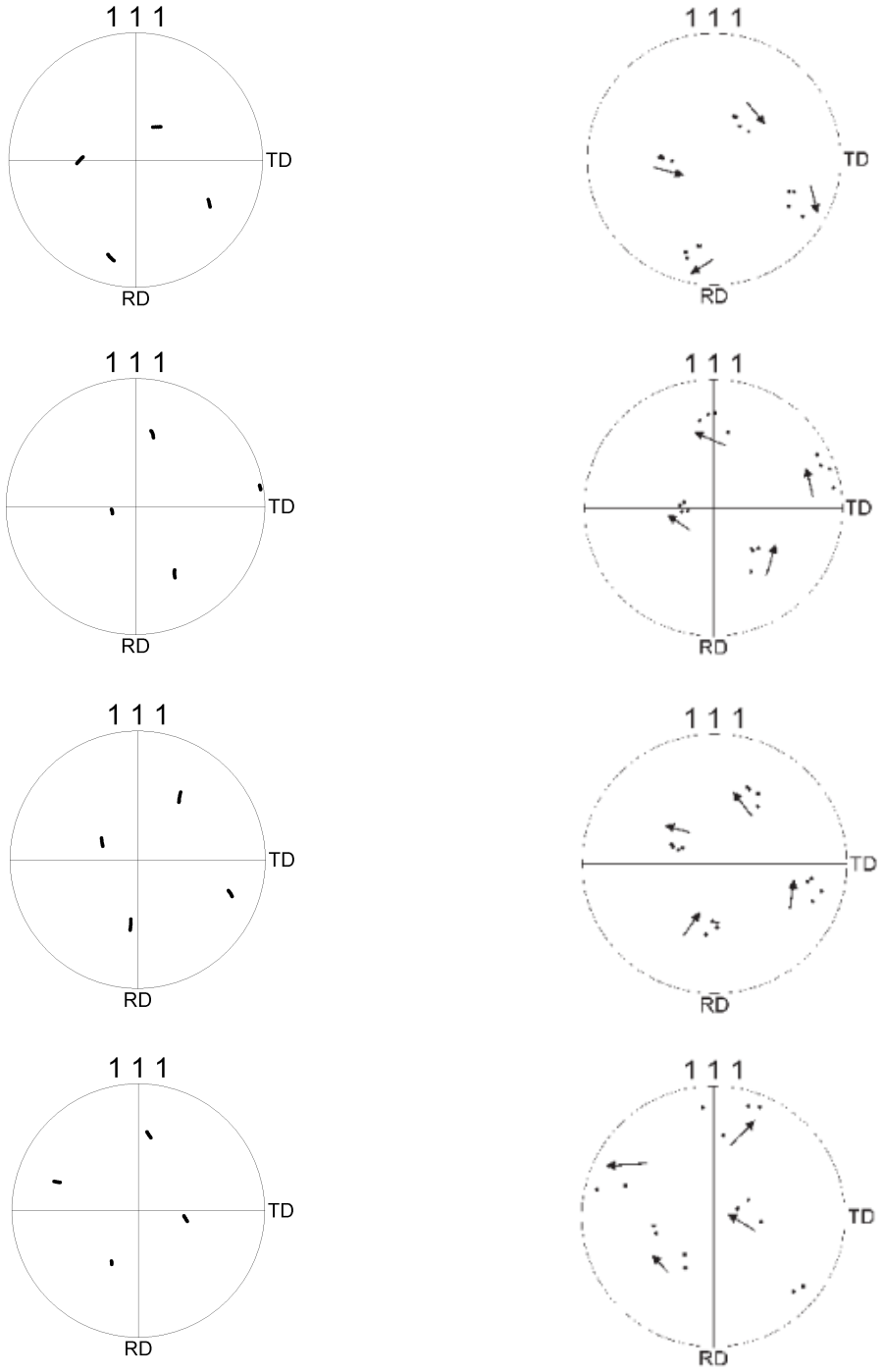

Figure 5.24 Rotation of (a) grain 1, (b) grain 7, (c) grain 8, and (d) grain 10. Pictured on the right hand column are experimental observations by Prasannavenkatesan et al. [13].

Rotations of grain 1, grain 7, grain 8, and grain 10 after ~ 15 % thickness reduction, are shown in Fig 5.24. These results are compared with the experimental results presented in the reference [13]. Crystallographic orientation plots shown along the right hand columns in Fig. 5.24 are those reported by Prasannavenkatesan et al. [13].The presented CPFEM model predicts rotations of grain 7, 8, and 10 reasonably well. However the predictions are slightly off for grain 1. The study by Zaefferer et al. in [16] and by Roters in [17] shows that the material behavior within a grain is very much affected by the orientation of grain boundaries with respect to the external loading. Considering the fact that we do not include the effect of grain boundaries explicitly in our CPFEM model, the present results predict the grain orientation evolution in a multicrystal reasonably well.

Fig 5.25 compares evolution of dislocation density in grain 1, 2, 6, 7, 8, 9, and 10 which is discussed further referring to the geometrical and micromechanical Taylor factors. The term 'micromechanical' used here is adapted from Raabe et al. [18] who distinguish macromechanical Taylor factor from the micromechanical Taylor factor. In the former, von Mises strain is determined as a function of global strain components, and in the latter as a function of local strain components. Therefore a micromechanical Taylor factor is defined as $\frac{\sum_{\alpha}\left|\gamma^{\alpha}\right|}{e_{local}}$. Where $\sum_{\alpha}\left|\gamma^{\alpha}\right|$ is the total accumulated slip on all slip systems α and e_{local} is the local von Mises strain. The geometrical and micromechanical Taylor factors are shown in Table 5.6. The Taylor factor values are in general in the order of dislocation density accumulation in the corresponding grains. Grain 1 and grain 10 are

exceptions. Grain 10 has a high Taylor factor but not a high accumulated dislocation density.

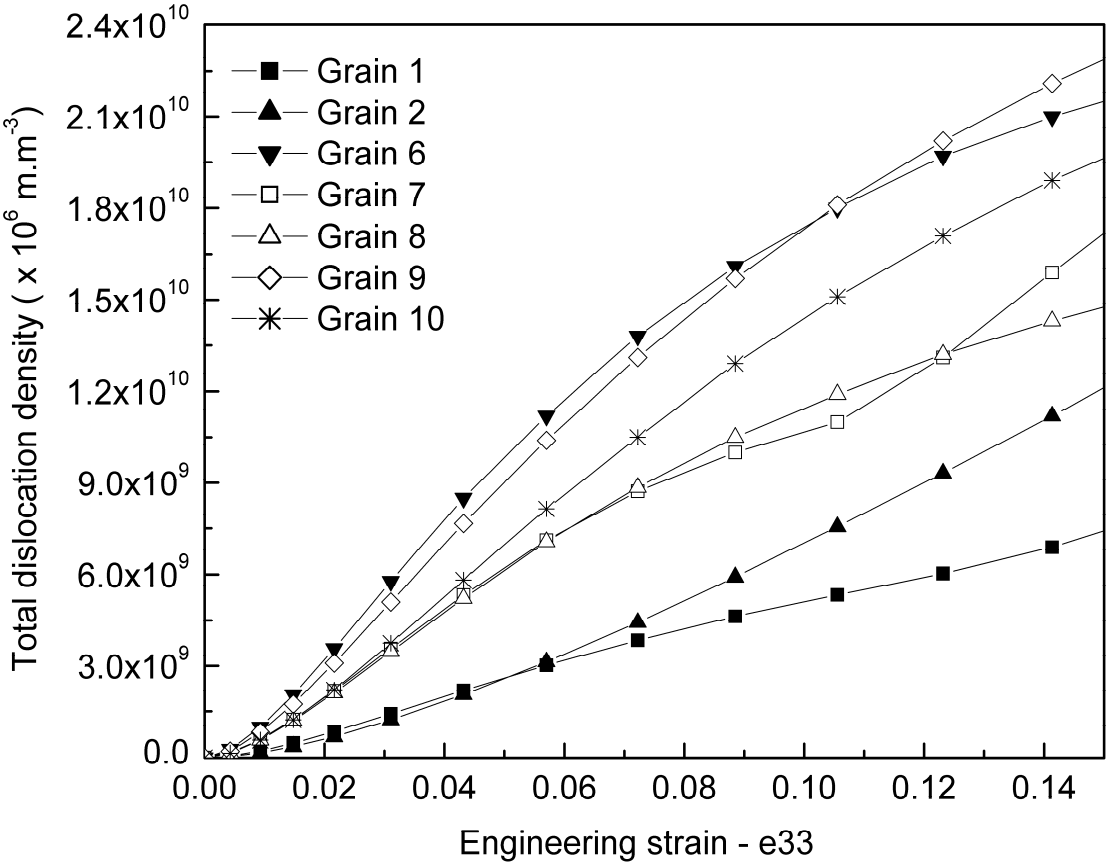

Figure 5.25 Dislocation density evolution in grain 1, 2, 6, 7, 8, 9, and 10 as a function of engineering strain in the Z direction (thickness)

Table 5.6 Taylor factors* for grain 1,2,6,7,8,9, 10

Grain Identification No.	Geometrical Taylor Factor	Micromechanical Taylor factor $\frac{\sum_{\alpha}\left\|\gamma^{\alpha}\right\|}{e_{local}}$
Grain 1	3.39	3.22
Grain 2	2.58	2.51
Grain 6	3.19	3.32
Grain 7	3.07	3.09
Grain 8	2.95	2.70
Grain 9	3.00	3.56
Grain 10	4.58	3.82

* e is the equivalent (von Mises) strain

As mentioned earlier, one of the key factors affecting the microstructure evolution and hardening of individual grains in a multicrystal is the effect of grain boundaries which is not considered explicitly in the present model. The only way how the effect of interfaces such as grain boundaries becomes active here is by the inherent compatibility condition used in the finite element method. Apart from the aforesaid, mesh density does affect the predictions by the finite element model. As a qualitative measure of the effect of mesh density, two different simulation results are compared at the same thickness reductions. Fig. 5.26a represents a non-uniform mesh which uses finer mesh around the interfaces and in the regions of complex geometries. The element size in this mesh varies

from 0.10 mm to 0.40 mm. Fig. 5.26b shows a uniform finer mesh of element size 0.1 mm. Definitely, a finer mesh shows predictions unaffected by the mesh dependent artifacts, for the present research an optimum mesh density was used using selective meshing. A mesh thus generated decreased the total simulation time by approximately 10 times as compared for the mesh shown in Fig. 5.26b. In the next study we use a finer and uniform mesh to compare the microstructural evolution against the CPFEM model predictions.

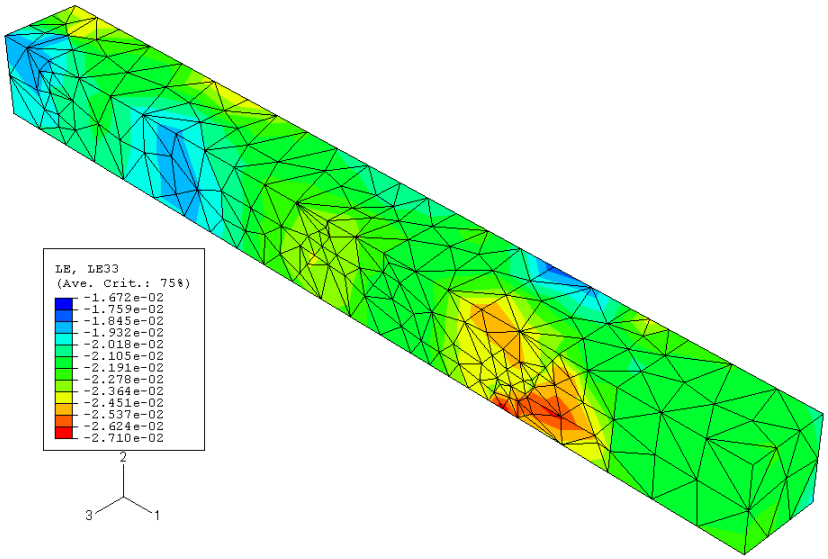

(a)

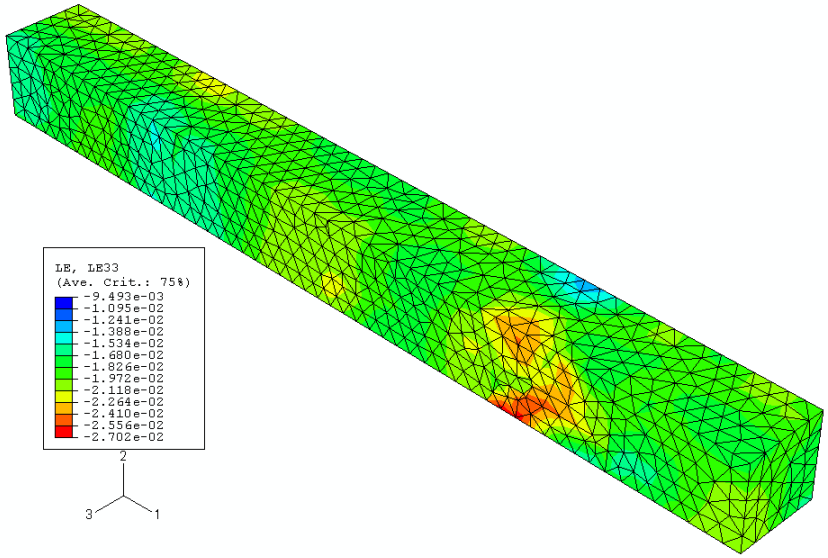

(b)

Figure 5.26 Comparison of fine and coarse mesh effects. The evolution of strain along the thickness direction is compared. (a) Coarse mesh with selective fine meshing around grain boundaries (b) Uniform fine mesh.

5.5.2 Microstructure evolution in a 2D multicrystal

One step further, in this section, a more complex study on the microstructure evolution is done. The structure considered is a 2D columnar polycrystal as in the previous section but it has larger number of grains overall and more grains in the neighborhood. The 2D columnar polycrystal considered here is from the work of Raabe et al. [18], and is a pure aluminum polycrystal which contains > 99.999% Al. In the experimental work done by these researchers, the orientation map of the polycrystal was determined using interrupted measurements by EBSD technique. The orientation image was mapped onto an FEM mesh for study by a CPFEM model. However, in the present study an idealized grain topology is mapped and not the real microstructure. Idealization here specifically refers to the fact that grain boundaries are planar surfaces and therefore the projections of grain boundaries on the XY planes are straight lines. Also, the orientations used in this study are average orientations of individual grains and no misorientation exists within a grain. Such an idealized grain structure is shown in Fig. 5.27a with the orientations of individual grains shown on the standard stereographic unit triangle in Fig. 5.27b. A list of Euler angles for the 18 constituent grains is given in Table B.2 in Appendix B [19].

A map of von Mises strain determined using digital image correlation is shown in Fig. 5.28. The image shows the distribution of von Mises strain at ~ 8% determined using the data of displacement in the thickness reduction. Evidently, the plastic deformation across the polycrystal is very heterogeneous. The regions showing high plastic deformation across the grain boundaries and with in single grains are visible.

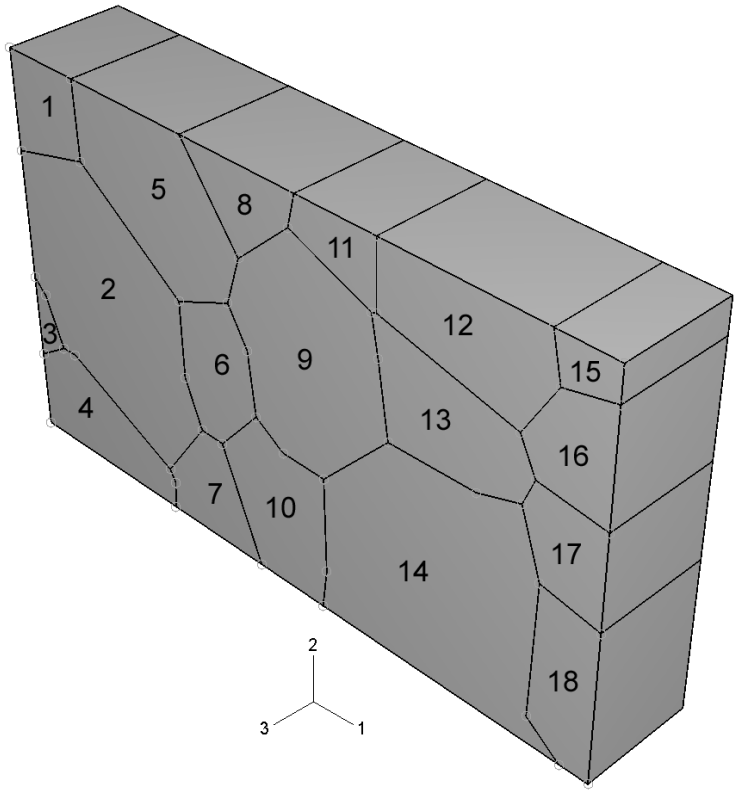

(a)

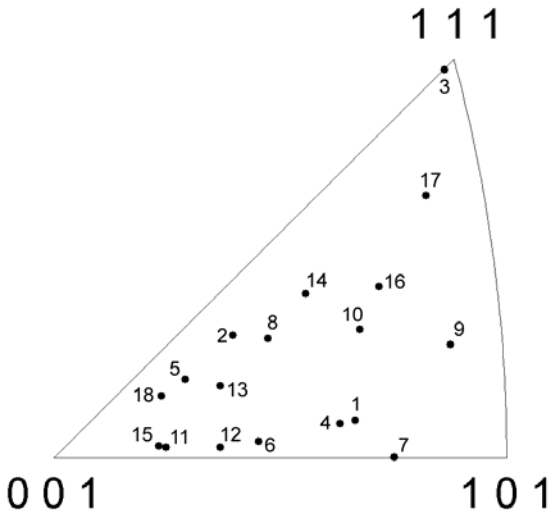

(b)

Figure 5.27 Idealized grain structures in the columnar polycrystal containing 18 grains

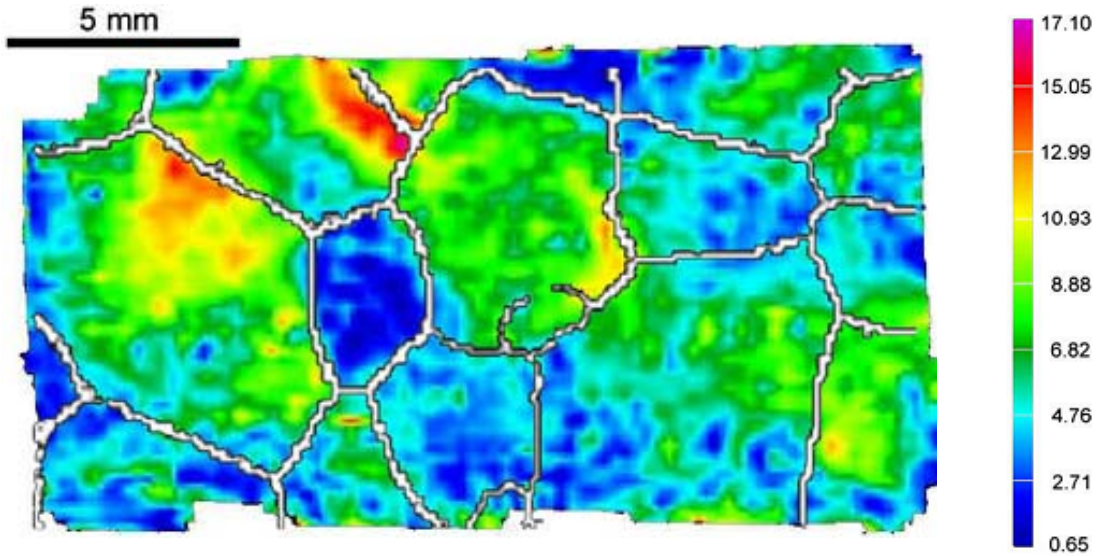

Figure 5.28 Heterogeneity of plastic deformation (von Mises) determined using strain map correlation at 8 % thickness reduction [18].

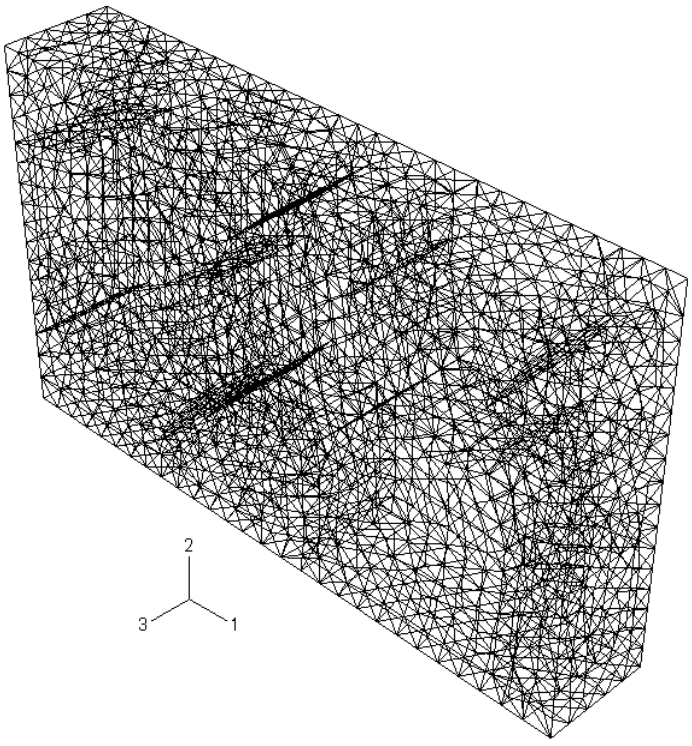

Figure 5.29 Uniform mesh with 19631 tetrahedral elements C3D4

The geometry is meshed using 19631, 4 node, 1 integration point elements which are C3D4 type elements in the ABAQUS^{TM}/Standard library. To cause plane strain deformation, identical boundary conditions that are used in the previous simulation of plain strain compression, were employed. Fig. 5.29 shows the mesh used for this simulation. The above observation of accumulated plastic deformation is compared against the CPFEM model observations using different microstructure parameters (e.g. accumulated dislocation density, dislocation evolution rate and accumulated shear).

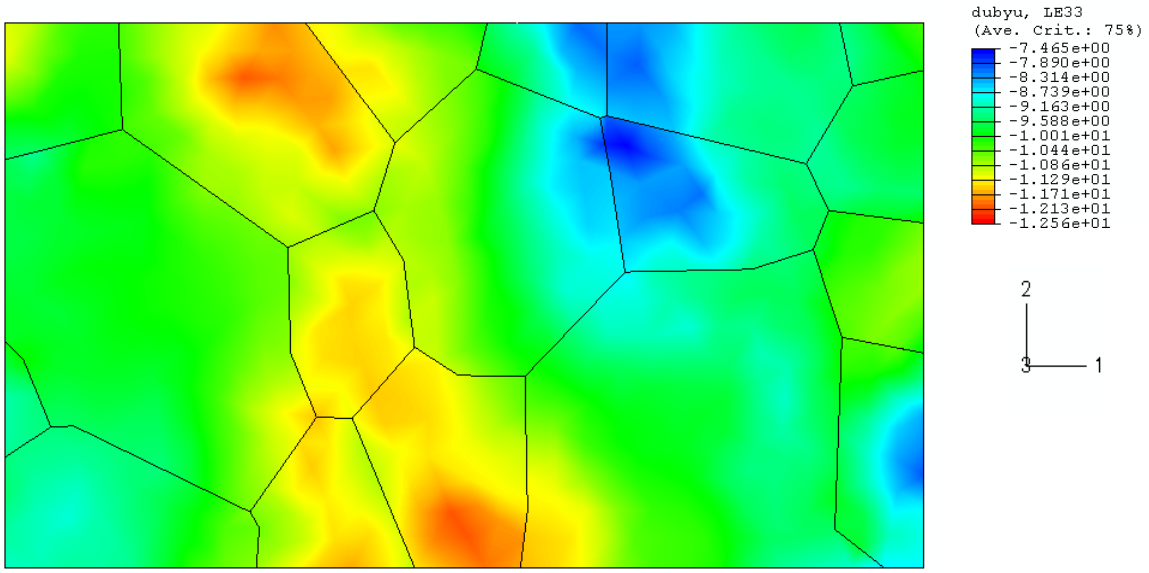

Figure 5.30 CPFEM prediction of von Mises strain at ~ 8% thickness reduction.

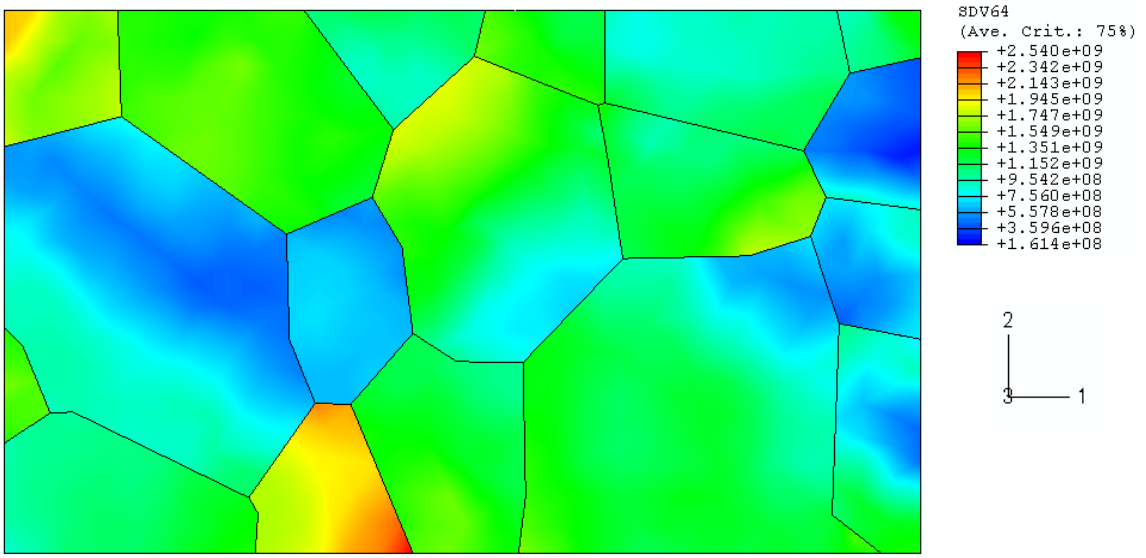

Figure 5.31 Accumulated dislocation density predictions at 8% thickness reduction by CPFEM model. The legend shows dislocation density $\times 10^6$ m.m^{-3}.

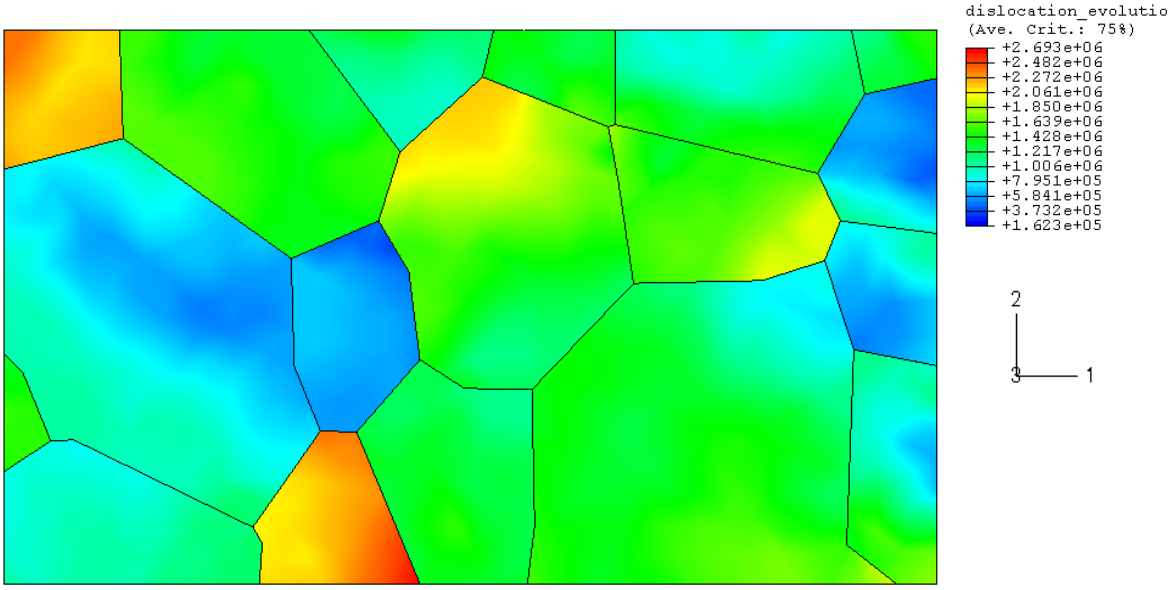

Figure 5.32 Prediction of dislocation density evolution rate at 8% thickness reduction by CPFEM model

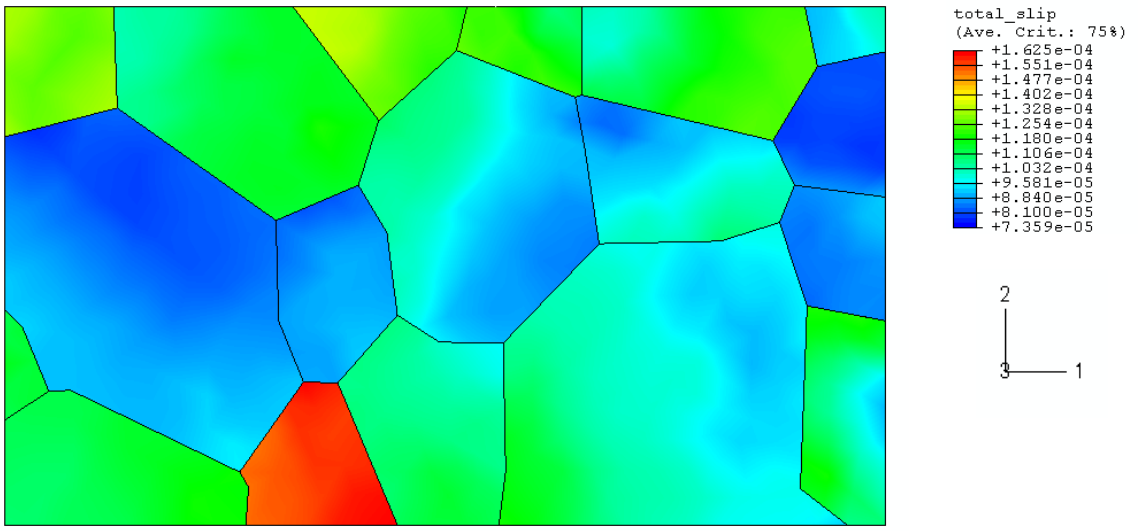

Figure 5.33 Total plastic shear rate at 8% thickness reduction by CPFEM model

The plastic strain map observed in the experiments does not match point to point with that predicted by the CPFEM model. The model is able to predict high and low regions of accumulated plastic deformation in some of the grains but in the other the predictions are no where close to the experiments. For example, the model shows high plastic deformation across the shared boundary of grain 5 and grain 8 but not across the shared grain boundary of grain 5 and grain 2. In fact, the model shows a low accumulated plastic strain in grain 2 in the neighborhood of grain 5. In the other regions such as grain 6, grain 7, grain 11, grain 12, grain 17, and grain 18 predictions by the CPFEM model compared well. Dislocation density distribution shown in Fig. 5.31, rate of dislocation density evolution shown in Fig. 5.32, and total plastic shear rate shown in Fig. 5.33 compare well with each other and the self validation of the model is justified.

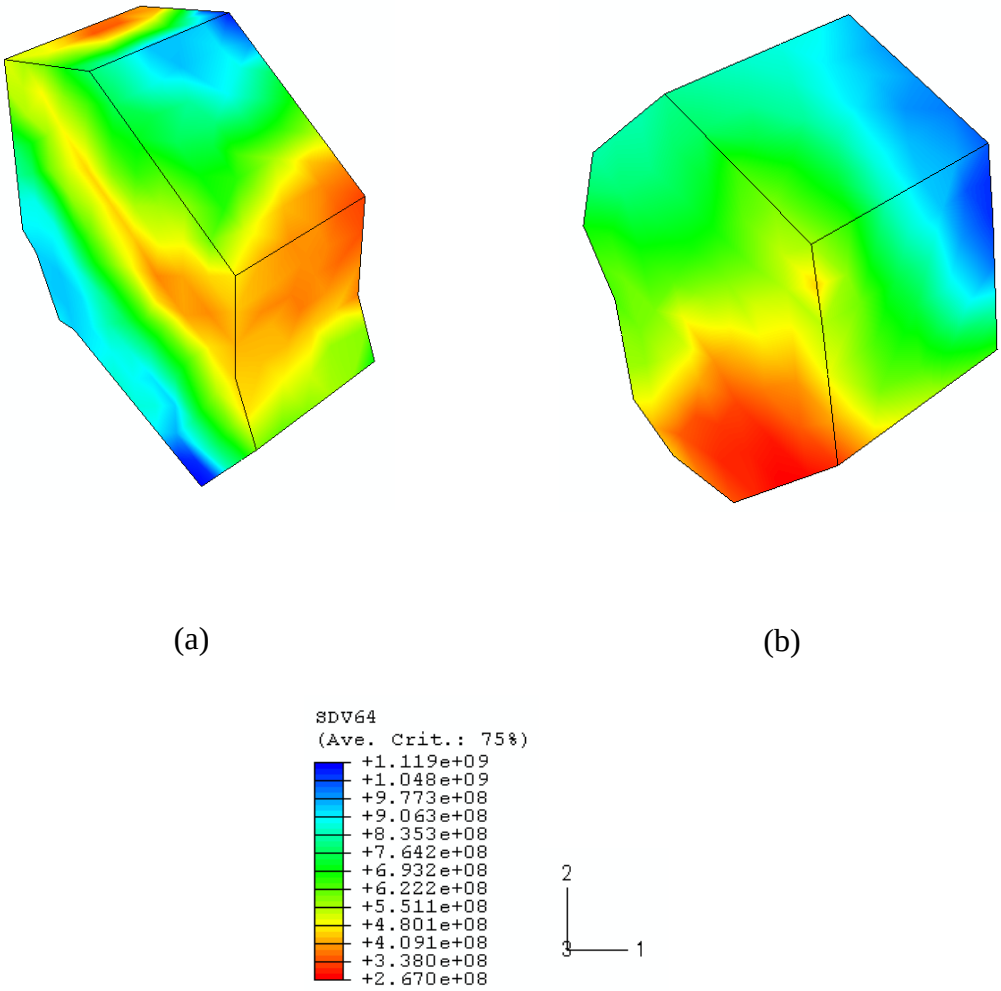

Figure 5.34 Heterogeneity of plastic deformation through thickness of (a) Grain 2, (b) Grain 6

To emphasize the heterogeneity across the thickness, through thickness views of grain 2 and grain 6 are shown in Fig. 5.33a and Fig. 5.33b respectively. Note that the distribution of microstructure parameters visible on the surface is not essentially consistent through out the volume. Therefore a true validation of microstructure evolution done only on the basis of microstructure evolution on the visible surface is not well

justified. As reported by Raabe et al. [18] that the real experimental conditions also include friction along the contact surfaces of the channel die, a 3D analysis of the microstructure evolution becomes even more important.

5.6 Summary

The dislocation density based framework of crystal plasticity described in Chapter 3 is employed to develop a CPFEM model using user interface subroutine UMAT in ABAQUS^{TM}. In this chapter it shown that the model is able to predict the anisotropy of single crystal aluminum including the overshooting behavior. A more stringent validation of the model is done by employing the model for studies on plane strain deformation of bicrystals and polycrystals. The model is able to predict evolution of orientations of individual grains in bicrystals and polycrystals. The evolution of microstructure variables such as dislocation density, and shear rate is consistent with the orientations of the grains. However, at the current state the model is sometimes inconsistent in predicting point to point material behavior.

References

[1] Hosford WFJ, Fleischer RL, Backofen WA. Acta Metallurgica 1960;8:187.

[2] ABAQUS Reference Manual Versions 6.5. Providence, RI: ABAQUS Inc., 2005.

[3] Joshi NR, Green Jr RE. Journal of Materials Science 1980;15:729.

[4] Taylor GI, Elam CF. Proceedings of The Royal Society London 1925;A108:28.

[5] Tabourot L, Fivel M, Rauch E. Materials Science and Engineering A 1997;A234-23:639.

[6] Anand L, Kothari M. Journal of Mechanics and Physics of Solids 1996;44:525.

[7] Basinski SJ, Basinski ZS. Plastic Deformation and Work Hardening. In: Nabarro FRN, editor. Dislocations in Solids, vol. 4. North-Holland, Amsterdam, 1979.

[8] Phillips WL. Transactions of AIME 1962;224:845.

[9] Devincre B, Kubin L, Hoc T. Scripta Materialia 2006;54:741.

[10] Madec R, Devincre B, Kubin L, Hoc T, Rodney D. Science 2003;301:1879.

[11] Tisone TC, Brittain JO, Meshii M. Physica Status Solidi (b) 1969;36:479.

[12] Franciosi P, Berveiller M, Zaoui A. Acta Metallurgica 1980;28:273.

[13] Prasannavenkatesan R, Li BQ, Field DP, Weiland H. Metallurgical and Materials Transactions A: Physical Metallurgy and Materials Science 2005;36A:241.

[14] Field DP, Alankar A. Metallurgical and Materials Transactions A: Physical Metallurgy and Materials Science 2009;Submitted.

[15] Kocks UF, Tome CN, Wenk H-R. Texture and Anisotropy - Preferred Orientations in Polycrystals and their Effect on Materials Properties: Cambridge University Press, 2000.

[16] Zaefferer S, Kuo JC, Zhao Z, Winning M, Raabe D. Acta Materialia 2003;51:4719.

[17] Roters F. Computational Materials Science 2005;32:509.

[18] Raabe D, Sachtleber M, Zhao Z, Roters F, Zaefferer S. Acta Materialia 2001;49:3433.

[19] Raabe D, Roters F. Personal communication on: Initial orientations of crystallites in the columnar polycrystal 2009.

CHAPTER SIX

CONCLUSIONS

A 3D CPFEM model based on statistical evolution of dislocation density is introduced in this work. The dislocation density evolution framework used in the model is adopted from a work presented in the literature (cf. Chapter 3). The following conclusions are drawn:

1. Stress-strain curves of Al single crystals are reasonably simulated with the characteristic differences in hardening behavior between {001} and {111} oriented crystals being captured by the model. At this point, only statistical evolution of dislocation densities is considered in the model. The evolution of edge and screw densities on different slip systems in an aluminum single crystal of <111> orientation is presented.
2. A generalized Taylor equation is used as a hardening law in which hardening coefficients are functions of strengths of various reactions, junctions, and locks between dislocations on co-planar and no-planar slip systems. Strength of junctions between dislocations on non-coplanar slip systems in aluminum is studied using 3D discrete dislocation dynamics of curved dislocations of mixed character. The hardening coefficients so determined are in the order with the ones presented in similar studies in the literature. The Hirth junction, glissile junction, Lomer junction, and collinear lock are found to have strengths in increasing order respectively. Resolved shear stress (RSS) plotted along with the number of junctions formed shows that with every new junction formed RSS evolves further

and with each unzipping of a junction, the stress decreases. Worth mentioning is the fact that some simulation dependent criteria (e.g. critical angles of the reacting segments, and the minimum length between two reacting segments) do play significant roles on the reactions.

3. It is shown that the CPFEM model is able to show overshooting phenomena in pure aluminum which is consistent with the experimental work reported in the literature. Collinear interaction coefficient of dislocations larger than that of Lomer junction, predicts an enhanced overshooting behavior. The effect of collinear interactions on overshooting is proposed to be because of latent hardening on the secondary slip system. This disables secondary slip systems for dislocation glide therefore dislocations continue to glide on the primary slip system and the phenomena of overshooting occurs.
4. Simulations of plane strain compression (idealized rolling) of polycrystalline aluminum having an initially random crystallographic texture also provide some validation for the model in the form of crystallographic texture predictions. Various texture components known to be present in rolled aluminum are seen in the simulated crystallographic texture and the characteristic “rolling texture” is observed. Texture prediction during simple shear of an aluminum polycrystal is also shown which compared well with experimental results presented in the literature. The evolution of α-fiber and β-fiber is shown with increasing thickness reduction and compares well with the data from the literature. Evolution of dislocation density distribution during plane strain compression of the polycrystal is compared at different thickness reductions. Using mapping of dislocation

densities coupled with crystallographic orientations of corresponding crystallites, it is shown that heterogeneity of accumulated dislocation density in the microstructure increases with increasing deformation.

5. To further investigate the microstructure evolution using numerical data on dislocation density, accumulated shear strain, and Taylor factor, simulations are performed for channel die compression of bicrystals and a 2D columnar polycrystal. The model is able to predict the evolution of crystallite orientations fairly closely to that observed in the experiments both in the bicrystals and in a 2D columnar crystals as well. In the simulations of 2D columnar polycrystals, a non-uniform strain field and dislocation density distribution is observed which is a result of grain interactions, local deformation gradient, orientation of crystallites and orientation of grain boundaries with respect to the external loading. The model shows high dislocation density accumulation in the grains which accumulate high strains. A further insight into rotation and hardening activities in different grains is given referring to the dislocation density accumulation and evolution of the Taylor factor using one-on-one correlation of microstructure evolution in the grains. The predictions of crystallite rotations match with the experimental results of some the crystallites and for the others they do not match well. However, the dislocation density evolutions self validate hardening in most of the grains when correlated with the Taylor factors of the chosen corresponding grains. Provided that the model does not contain any effects of grain boundaries and the long range effects from the neighborhood grains, these predictions are well justified.

Though there are several models which are able to predict texture evolution during material deformation, only a few bridge the gap between the physics of dislocation activity and crystal plasticity. This model shows a reasonable attempt at incorporating microstructural considerations into the model (in the form of predictions of dislocation structure evolution) along with the kinematics of crystal plasticity to form a more physically realistic prediction.

CHAPTER SEVEN

FUTURE WORK

1. A two step validation of the model is suggested in terms of dislocation density. First, dislocation density evolution as a function of strain must be compared with the experimental observations and the values of critical radii of the dislocation interactions must be determined using the saturation values of dislocation densities. A point to point comparison of dislocation density will not be possible at this stage. However, overall dislocation density distribution and orientation dependent evolution of dislocation densities in different grains in a large grained polycrystal may be used for a validation study. Electron channeling contrast imaging (ECCI) and dislocation density estimation using electron backscatter diffraction data may prove to be useful for a qualitative and quantitative validation respectively of dislocation density patterning.
2. It was shown in Chapter 5 that plastic deformation is heterogeneous even in pure aluminum. For the correct prediction of microstructure evolution during deformation of polycrystalline materials, and for the problems like fatigue where interfaces (e.g. grain boundaries and particle matrix interfaces) play key roles, it is of utmost importance to include the strain gradient plasticity.
3. Strain gradient effects will ensure that the non-local effects across the grain boundaries are active in the model. Nevertheless, it is worthwhile to attempt an additional constitutive framework which includes the grain boundary effects explicitly in the model framework.

4. The latent hardening coefficients are reported not to be very much affected by strain history. Evolution of hardening coefficients does occur through out the deformation history. A dislocation density dependence of the hardening coefficients can not be ruled out. Therefore it is suggested to include a functional dependence of hardening coefficients on the deformation history.
5. An improved time integration procedure focused on faster convergence will enhance the ability of the model for application to larger polycrystals and in general to microstructure having complex topology which could then be adapted to FEM mesh directly. This will also enable simulations of rather realistic microstructures.
6. Enriched with a large number of microstructure parameters, this model comes out to be an uphill task for specialized problems like fatigue which may prove to be unrealistically time consuming if approached directly. Rather then applying direct cyclic loading, a condensed form of fatigue loading history which produces the same effect may be used.

APPENDIX A

SYMBOLS AND MATHEMATICAL OPERATIONS

A.1 Slip directions ($\mathbf{m}_0^\alpha$) and slip plane normals ($\mathbf{n}_0^\alpha$) for FCC crystals

Slip System Index (α)	Slip System Label	$\mathbf{m}_0^\alpha$	$\mathbf{n}_0^\alpha$
1	B6	$\frac{1}{\sqrt{2}}[1\bar{1}0]$	$\frac{1}{\sqrt{3}}[111]$
2	B4	$\frac{1}{\sqrt{2}}[10\bar{1}]$	$\frac{1}{\sqrt{3}}[\bar{1}\bar{1}\bar{1}]$
3	B2	$\frac{1}{\sqrt{2}}[01\bar{1}]$	$\frac{1}{\sqrt{3}}[111]$
4	A5	$\frac{1}{\sqrt{2}}[110]$	$\frac{1}{\sqrt{3}}[1\bar{1}\bar{1}]$
5	A3	$\frac{1}{\sqrt{2}}[101]$	$\frac{1}{\sqrt{3}}[\bar{1}11]$
6	A2	$\frac{1}{\sqrt{2}}[01\bar{1}]$	$\frac{1}{\sqrt{3}}[1\bar{1}\bar{1}]$
7	D5	$\frac{1}{\sqrt{2}}[110]$	$\frac{1}{\sqrt{3}}[1\bar{1}1]$
8	D4	$\frac{1}{\sqrt{2}}[10\bar{1}]$	$\frac{1}{\sqrt{3}}[1\bar{1}1]$
9	D1	$\frac{1}{\sqrt{2}}[011]$	$\frac{1}{\sqrt{3}}[\bar{1}1\bar{1}]$
10	C6	$\frac{1}{\sqrt{2}}[1\bar{1}0]$	$\frac{1}{\sqrt{3}}[\bar{1}\bar{1}1]$
11	C3	$\frac{1}{\sqrt{2}}[101]$	$\frac{1}{\sqrt{3}}[\bar{1}\bar{1}1]$
12	C1	$\frac{1}{\sqrt{2}}[011]$	$\frac{1}{\sqrt{3}}[11\bar{1}]$

A.2 Orientation matrix using Bunge's convention of Euler angles

$$\mathbf{g} = \begin{bmatrix} \cos\varphi_1 \cos\varphi_2 - \sin\varphi_1 \sin\varphi_2 \cos\Phi & \sin\varphi_1 \cos\varphi_2 + \cos\varphi_1 \sin\varphi_2 \cos\Phi & \sin\varphi_2 \sin\Phi \\ -\cos\varphi_1 \sin\varphi_2 - \sin\varphi_1 \cos\varphi_2 \cos\Phi & -\sin\varphi_1 \sin\varphi_2 + \cos\varphi_1 \cos\varphi_2 \cos\Phi & \cos\varphi_2 \sin\Phi \\ \sin\varphi_1 \sin\Phi & -\cos\varphi_1 \sin\Phi & \cos\Phi \end{bmatrix}$$

where φ_1, Φ, and φ_2 are Euler angles defined as:

$$0 \le \varphi_1 \le 360^o,$$

$$0 \le \Phi \le 180^o, \text{ and}$$

$$0 \le \varphi_2 \le 360^o.$$

A.3 Basic mathematical operations on tensors

Inner product $\mathbf{AB}$	$(\mathbf{AB})_{ik} = \mathbf{A}_{ij}\mathbf{B}_{jk}$
Double contraction $\mathbf{A}:\mathbf{B}$	$\mathbf{A}:\mathbf{B} = \mathbf{A}_{ij}\mathbf{B}_{ij}$
Tensor product of vectors $\mathbf{a}\otimes\mathbf{b}$	$(\mathbf{a}\otimes\mathbf{b})_{ij} = a_i b_j$
Tensor product of matrices $\mathbf{A}\otimes\mathbf{B}$	$(\mathbf{A}\otimes\mathbf{B})_{ijkl} = \mathbf{A}_{ij}\mathbf{B}_{kl}$
Lower tensor product of matrices $\mathbf{A}\underline{\otimes}\mathbf{B}$	$(\mathbf{A}\underline{\otimes}\mathbf{B})_{ijkl} = \mathbf{A}_{ik}\mathbf{B}_{jl}$
Upper tensor product of matrices $\mathbf{A}\overline{\otimes}\mathbf{B}$	$(\mathbf{A}\overline{\otimes}\mathbf{B})_{ijkl} = \mathbf{A}_{il}\mathbf{B}_{jk}$

APPENDIX B

EULER ANGLES FOR POLYCRYSTALS

Table B.1 Initial crystallographic orientations for the 10 grain polycrystal

Grain Identification No.*	φ_1 (^{o})	Φ (^{o})	φ_2 (^{o})
1	100.611	23.663	281.838
2	10.772	19.996	350.421
3	86.918	20.455	311.001
4	124.045	42.628	222.709
5	158.366	22.173	225.287
6	191.024	33.690	133.155
7	141.521	23.319	253.018
8	317.189	17.361	72.307
9	35.581	29.164	3.151
10	289.115	39.362	68.526

* Grain identification numbers shown here are the numbers shown on the real orientation imaging map presented in Fig. 5.21a

Table B.2 Initial crystallographic orientations for the 18 grain polycrystal

Grain Identification No.*	φ_1 (^{o})	Φ (^{o})	φ_2 (^{o})
1	88.800	31.100	7.200
2	-34.400	22.500	55.600
3	-69.200	53.600	45.100
4	89.100	29.600	6.900
5	33.000	16.000	30.900
6	-58.100	21.300	85.400
7	-5.000	34.600	0.200
8	4.500	25.300	60.800
9	-19.700	41.400	16.000
10	27.400	33.800	22.900
11	-16.100	11.800	5.400
12	-62.900	17.400	86.200
13	89.500	18.900	23.500
14	41.900	30.800	56.800
15	-28.500	11.100	83.500
16	51.600	37.200	27.900
17	-59.000	45.300	35.300
18	-47.000	13.000	59.900

* Grain identification numbers shown here are corresponding to those shown in Fig. 5.27a